ABSTRACT

Title of Document:	PLASMA-SURFACE INTERACTIONS DURING REACTIVE PLASMA PROCESSING OF HYDROCARBON FILMS
	Nicholas Andrew Fox-Lyon Doctor of Philosophy, 2013
Directed By:	Professor Gottlieb S. Oehrlein Materials Science and Engineering and Institute for Research in Electronics and Applied Physics

Reactive plasma interactions with hydrocarbon-based surfaces play a critical role in future biological-plasma applications and for microelectronic device manufacture. As device dimensions get smaller and we require fine control of surfaces during plasma processing we will need to develop more understanding of fundamental plasma surface interactions. Through the use of plasma-deposited amorphous carbon films interacting inert/reactive plasmas (Ar/H_2 plasmas) we explored etch rates and the formation of modified layers. Facing Ar and H_2 plasmas mixtures, hydrocarbon surfaces can exhibit widely different properties, depending on plasma composition (ions, reactive species, fast neutrals) and initial film composition (graphitic, polymeric). Ar plasmas cause densification of hydrocarbon surface by selectively sputtering H atoms, while H_2 plasmas cause incorporation/saturation of H atoms within the film surface. For hard amorphous carbon, we find that small

amounts of H_2 added to Ar plasma can completely negate ion-induced densification. Plasmas are also drastically changed by small impurities of H_2 atoms. We investigated the plasma property effects of adding H_2, D_2, CH_4, and surface derived hydrocarbon gases. We find that small amounts (as low as 1%) of H_2/D_2 in Ar cause a large decrease in electron density, increase in electron temperature, Ar metastable atoms, and radically different ion mass distributions. These effects are intensified at higher pressures, as neutral molecule-ion interactions in the plasma increase. These changes can be related to the surface modification caused by the plasma. Surface derived impurities into inert plasmas were also investigated. Hydrocarbon flow from the surface causes changes to plasma properties similar to the addition of CH_4 gas. We applied the learning from these fundamental plasma-surface interaction studies to an applied problem of plasma-assisted shrink of asymmetric photoresist features. Using fluorocarbon-based plasmas, we successfully shrink asymmetric pattern features and find that lower concentrations of C_4F_8 in plasmas and shorter deposition thicknesses lead to more uniform shrink in L and W dimensions. To improve future plasma-assisted shrink processes, careful tuning of plasma composition and feature dimensions is critical.

PLASMA-SURFACE INTERACTIONS DURING REACTIVE PLASMA ETCHING OF HYDROCARBONS

By

Nicholas Andrew Fox-Lyon

Dissertation submitted to the Faculty of the Graduate School of the
University of Maryland, College Park, in partial fulfillment
of the requirements for the degree of
Doctor of Philosophy

2013

Advisory Committee:
Prof. Gottlieb Oehrlein, Department of Materials Science & Engineering, Chair
Prof. Robert Briber, Department of Materials Science & Engineering
Prof. Ray Phaneuf, Department of Materials Science & Engineering
Prof. Oded Rabin, Department of Materials Science & Engineering
Prof. Raymond Sedwick, Department of Aerospace Engineering

Acknowledgements

This work would not have been possible without my advisor, Prof. Gottlieb Oehrlein. Through your constant patience, guidance, and encouragement I had the opportunity to learn some amazing things and have been a part of world-class research projects. You set an example for the quality of work and research that I will strive to keep up in my career going forward.

I would like to thank my dissertation committee for showing interest in my work and reading my dissertation. Prof. Briber, Prof. Phaneuf, Prof. Rabin, and Prof. Sedwick – Thank you.

Thanks to Texas Instruments, the US Department of Energy Office of Fusion Energy Sciences (under Award DE-SC0001939) and the DOE Plasma Science Center for fostering such a collaborative and productive environment. More specifically, I'd like to thank my collaborators at University of California, Berkeley: Prof. Graves and Dr. Ning, my collaborators associated with West Virginia University: Prof. Koepke, Dr. Demidov, and Jim Franek. Special thanks to Dr. Valery Godyak, who always had time to help me out with probe measurement problems. I'd also like to thank my collaborators and program managers David Farber and Tom Lii, at Texas Instruments, for helping to steer my project with helpful insights.

To my current and former laboratory colleagues and friends – Dr. Ming-Shu Kuo, Dr. Robert Bruce, and Dr. Florian Weilnboeck, Elliot Bartis, Dominik Metzler, Andrew Knoll, Chen Li. I will never forget the times we've spent in the in/out of work over the years. Thank you for helping me complete my research and being my

closest friends. I'd also like to thank my IREAP buddy Dr. Jane Cornett for her friendship, advice, and coffee making over these last five years.

The constant encouragement from my parents Debra and David Lyon kept me going. Thank you for guiding me and getting me to where I am today. To my grandmother, Amerylis Epps, your frequent cards/letter and support have meant so much to me. To my grandfather, Robert Epps, thanks for being there when I needed you, I wish you were here to see me finish. And last, but not least, thanks to Kate Schuerman for your eternal patience during my studies. I cannot wait to start the next chapter of my life by your side!

Table of Contents

List of Figures

Chapter 1: Introduction

1.1 Plasma-material interactions

Plasma-material interactions are of fundamental importance in microelectronic device manufacture, plasma surface functionalization, plasma-biological deactivation and other applications.[1.1] Low-pressure plasma processing can be used to remove unwanted films,[1.2] transfer patterns into substrates,[1.3] deposit thin graphitic films,[1.4] and functionalize surfaces.[1.5] Depending on the application, plasma properties can be tuned to give desired fluxes of surface interacting species. Important species at plasma-facing surfaces are high energy ions, UV/VUV photons, reactive species, and fast neutral atoms (seen in fig. 1.1). For many applications, these plasma components can cause synergistic effects on surfaces.[1.6] Coburn and Winters described a classic case of ion/reactant synergistic effects causing the transition from physical sputtering to chemical sputtering of atoms at surfaces facing the plasma.[1.7] These effects can be etching of atoms and molecules, changes in surface chemistry, morphology, and density of the films and in the bulk (UV/VUV). In turn, the etching surface can feed atoms, molecules and electrons back into the plasma.

Hydrocarbon surface interaction with plasmas is interesting because of its ubiquity in plasma applications. Carbon elements were once proposed and researched extensively for fusion plasma facing applications.[1.8] A more common example is plasma etching of polymeric photoresists (PR). PR's are used extensively in device manufacture as sacrificial photolithographic masks.[1.6] As device dimensions get smaller, control of plasma-PR surface interactions becomes of critical importance to

control feature dimensions. Coupled with this, newer generations of polymeric PR (tuned to lower wavelengths) exhibit poor etching behavior and roughening in plasmas.[1.9] Our group has extensively investigated the synergistic roughening effects caused during plasma etching of PR, with the aim of improving atomistic understanding of plasma-surface interactions.[1.10–1.13] In this study, we look to simplify the synergistic effects in an etching material system to gain better understanding.

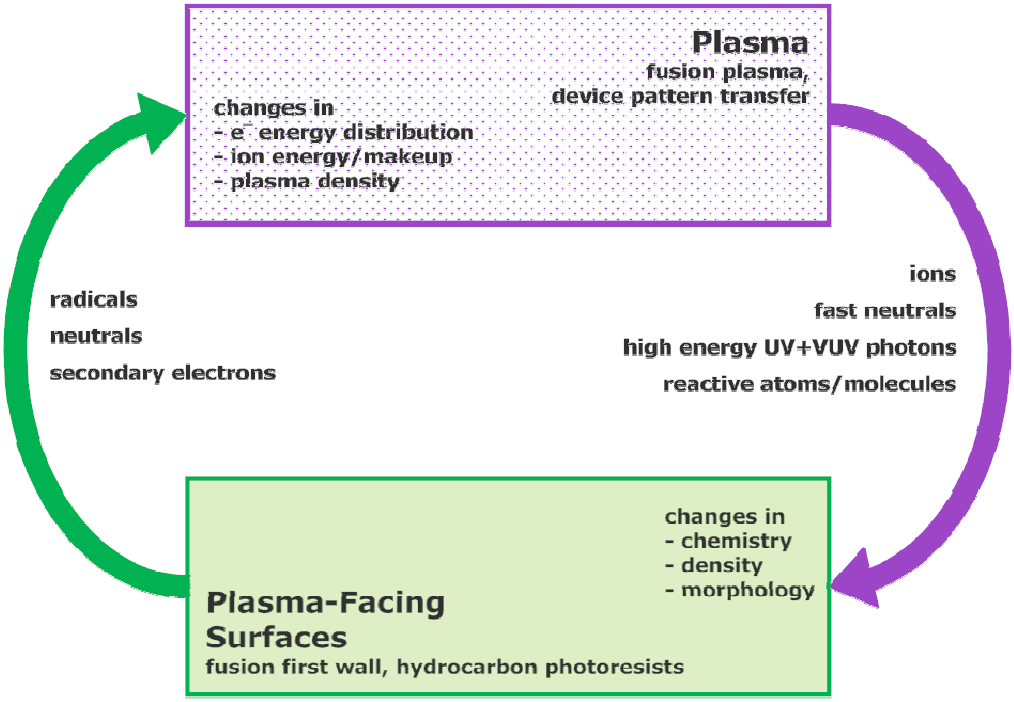

Figure 1.1 *Schematic of plasma-surface interacting species, modifications, and feedback.*

Taking a step back from specific applications, we seek to identify the fundamental dependencies of plasma species and initial hydrocarbon surface conditions on etching system outcomes as they evolve. There is interest to the study of how simple inert plasmas interact with hydrocarbons, and how the addition of reactivity changes the process. Hopf *et al.* investigated the effect of combined inert Ar^+ ions and reactive H

atoms etching hydrocarbon surfaces. [1.14] Using experimental data and models, they found that the surface response to minute flows of reactants is large. In this work, we seek to explore this effect, and how to control surface in these films. To do this, we investigate simplistic model hydrocarbons in fundamental inert/reactive plasma situations.

1.2 Reactive impurities in inert plasmas

Impurities in plasmas and reactive plasma mixtures are of large interest for applications in device manufacture and fusion plasma research. Ar-based plasmas, used extensively in device manufacture, are highly sensitive to low levels of molecular impurities.[1.15] Small amounts of molecular impurities added to Ar have shown to cause large changes to plasma properties and species. Gudmundsson first investigated the effect of H_2 and O_2 impurities in Ar plasmas in inductively coupled plasma systems.[1.16,1.17] He found that average ion mass decreased as Ar^+ ions were becoming lesser contributions. Kimura and Kasugai investigated the effects of N_2 and H_2 on Ar plasmas using a global model, and proposed that ArH^+ ions could become important with increasing H_2 content.[1.18,1.19] Recently, this topic has become quite active, due to interest in reactive plasmas and impurity characterization. Measurements for all relevant ion types, Ar metastable atom densities, and other species in these plasmas have been reported.[1.20–1.23] Figure 1.2 displays an inert plasma and a reactive impurity plasma in our inductively coupled plasma system. In these studies we continue to explore the effects of impurity addition to inert plasmas, specifically isotope and surface derived impurities.

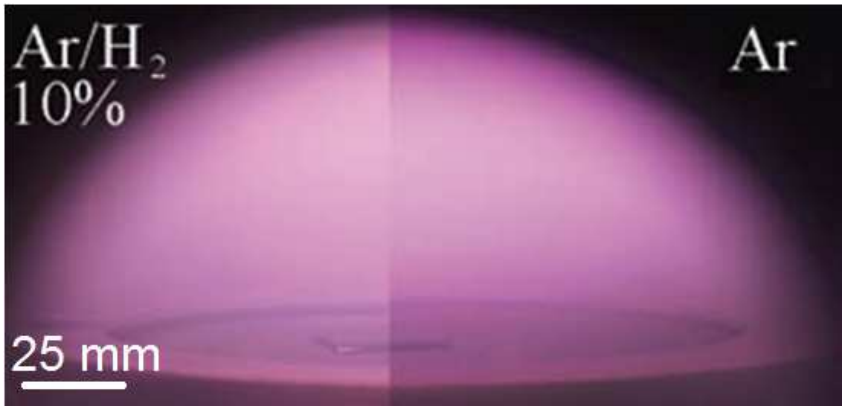

Figure 1.2. *Inert plasma with and without H_2 impurities in an inductively coupled plasma reactor.*

1.3 Collaborative research

These research projects were based upon several collaborations of leading research groups each specializing in different aspects of plasma-material interactions and a brief description is given in Fig. 1.3. The groups from University of Maryland (UMD), University of California, Berkeley (UC, Berkeley), West Virginia University (WVU), and the University of Michigan, Ann Arbor (U. Mich.) are individual members of the Department of Energy Plasma Science Center for Predictive Control of Plasma Kinetics, centered at U. Mich.

Project Member	Members	Expertise/Technique	Task
UMD	Oehrlein	Plasma Deposition/etching Surface characterization Plasma characterization	Plasma-surface interactions
UC, Berkeley	Graves Ning	Plasma-surface modeling	Inert/Reactive ions on amorphous carbon
WVU	Koepke Demidov	Spectroscopy and modeling	Reactive plasma effect on plasma properties
TI	Farber Lii	High AR patterns Cross section SEM	Plasma-assisted shrink of mask materials
U. Mich.	Godyak	Langmuir probe expertise and equipment	Reactive and depositing plasma characterization

Figure 1.3 *Organizational tables of collaborations in this dissertation.*

1.4 Experimental approach

1.4.2 UMD Laboratory for Plasma Processing of Materials

All experimental work in these studies was performed at the University of Maryland Laboratory for Plasma Processing of Materials (PPM). The PPM laboratory has a unique setup of high vacuum plasma-etching systems coupled with in-situ and vacuum transfer capable sensitive diagnostics (as seen in Fig. 1.3). This allows for investigations of transient, vacuum dependent chemical states on plasma-interacting surfaces.

The majority of the experimental work was performed in an inductively coupled plasma reactor (represented by the schematic in Fig. 1.4). This system has been used previously in the PPM and has been described in detail.[1.24] A brief description of the plasma generation and operation is as follows: a planar coil is located above a quartz dielectric window and is powered with a 13.56 MHz power supply coupled through an L-type matching network. To control ion directionality and energies to samples, an electrode can be biased independently using a 3.7 MHz power supply. The system is capable of ion energies ranging from 15 eV to 200 eV. Samples on the substrate are adhered using a thermal grease and actively cooled with a chiller to 10 °C. For sensitive plasma diagnostics and plasma-surface interactions, low amounts of impurities are required. Before starting experiments, the base pressure of the chamber was below 1×10^{-5} Torr. A permanently mounted ellipsometer samples the surface of the substrate electrode. Concurrent use of plasma

diagnostics (OES, Langmuir probe, ion sampling system—described in next section) also are available on the system.

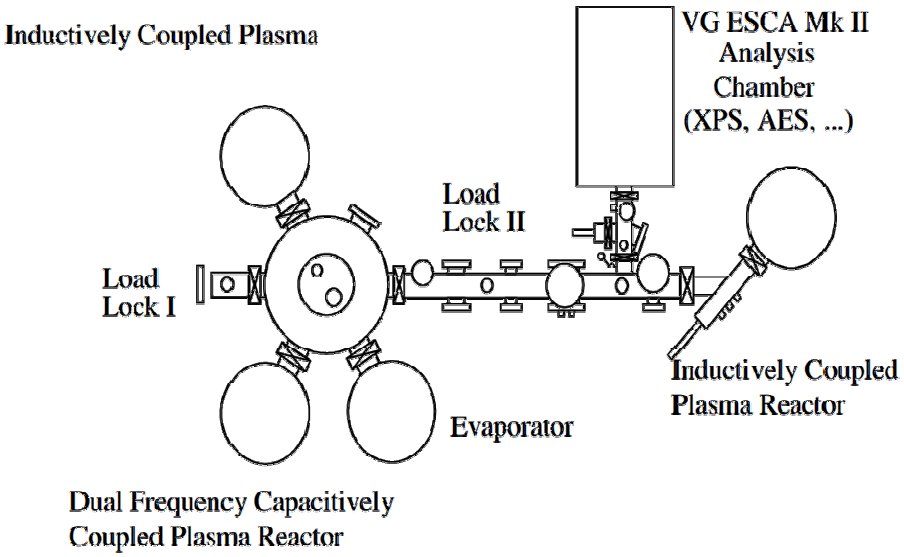

Figure 1.4 *Vacuum system cluster in the Plasma Processing of Materials Laboratory at UMD.*

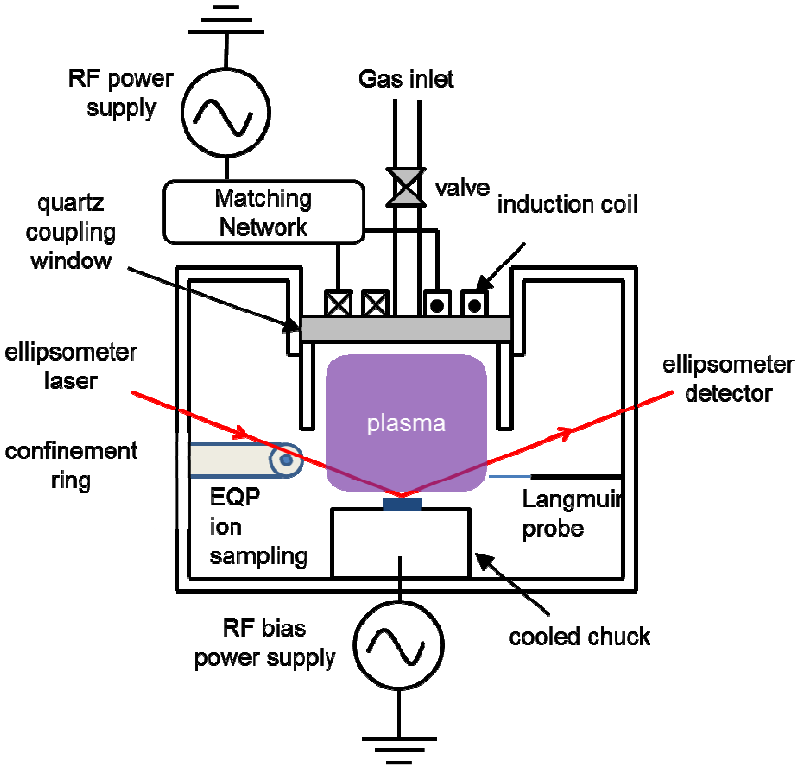

Figure 1.5. *Schematic of the inductively coupled plasma reactor used in these studies with in-situ plasma and surface diagnostics.*

1.4.3 Description of materials

In this study we investigated plasma-surface interactions with model plasma-deposited hydrocarbons. Hydrocarbon materials were grown in-situ using CH_4-based plasmas. By tuning the plasma parameters (ion energy, $\%CH_4$, source power), films were grown from very graphitic (H-poor, high density) to very polymeric (H-rich, low density). For more information about these plasma-deposited polymers, Schwarz-Selinger *et al.*[1.25] has reviewed this growth conditions/parameters that govern film properties. For plasma-assisted shrink studies, 193 nm PR patterned and blanket films were used as deposition substrates. In shrink studies, plasma deposited FC films were deposited onto substrates. For more information about the properties of these films and growth conditions see Labelle *et al* [1.26]

1.4.4 Plasma characterization techniques

Plasmas were monitored using multiple techniques to sample surface reactive and important species. Concurrent use of multiple plasma diagnostic techniques allows for a broad picture of plasma species behavior.

1.4.4.1 Langmuir probe

Plasma probe measurements are the predominant method to collect information on electron densities and energy distributions. A Plasma Sensors Langmuir probe was used to collect time-resolved data in reactive mixtures and depositing plasma conditions.[1.27]

1.4.4.2 Ion mass spectrometer

To understand the role of ions interacting with surfaces, understanding of ion compositions and energies is important. A Hiden EQP ion mass spectrometer system was used to measure the mass and energy of surface interacting ions.

1.4.4.2 Optical emission spectrometer

Optical emission from the plasma is useful for detecting species and electron energies within a plasma by the emission of excited states. It was used extensively in this study as to determine chamber conditioning (similar to process endpoint detection). In this study, a SPEX 750m spectrometer was used to detect lines as close as 0.3 Å apart.

1.4.5 Surface characterization techniques

Surfaces were monitored using in-situ diagnostics, along with post-plasma processing diagnostics. In-situ techniques allow for gathering information while the plasma is interacting with the sample. After processing, samples can be removed into atmosphere for atomic force microscopy or scanning electron microscopy measurements or vacuum transferred to x-ray photoelectron spectroscopy directly from the processing reactor.

1.4.5.1 In-situ ellipsometry

Ellipsometry was used for thin-film characterization during plasma deposition and etching to find index of refraction and thickness. The ellipsometer is a rotating compensator ellipsometer configured in the polarizer-compensator-sample-analyzer configuration at an angle of ~72°. The ellipsometer outputs data in Ψ (change in relative amplitude in s and p polarized light) and Δ (change in phase of s and p

polarized light). Modeling these values using a multilayer model for films, allows for extraction of time-resolved optical indexes and thicknesses.[1.28]

1.4.5.2 Atomic force microscopy (AFM)

Surface topography of films exposed to plasma was investigated using AFM. For hydrocarbon films, the AFM was operated in tapping mode and the surface roughness was calculated from the root-mean-square of the surface topography.

1.4.5.3 X-ray photoelectron spectroscopy (XPS)

Chemical composition of film surfaces before and after plasma treatment was investigated using XPS in a Vacuum Generators ESCA Mk II surface analysis chamber. Samples can be vacuum transferred from the deposition stage to the analysis chamber to prevent oxidation and adsorption of atmospheric impurities.

1.4.5.4 Scanning electron microscopy (SEM)

For SEM data in these studies looking at high aspect ratio features, a Hitachi SU-70 SEM in the University of Maryland Nanocenter was used. The change in feature dimensions was extracted using an automatic and manual line drawing program (Digimizer) of SEM micrographs.

1.5 Outline of thesis

The goal of this thesis is to improve understanding of subtle changes to plasmas and surfaces during plasma processing to improve plasma process design. With increased understanding we can better predict when small changes in plasma parameters can have large impacts on the surface being processed and plasma processing.

In Chapter 2, we investigated the mechanistic effects of Ar, H_2, and Ar/H_2 plasmas on graphitic amorphous hydrocarbons. We show data and modeling of the ion energy-dependent effects when Ar plasma causes surface densification, H_2 plasma causes hydrogenation, and Ar/H_2 plasmas can cause varying degrees of either effect, depending on the chemical composition.

In Chapter 3, we looked into the effect that chamber pressure and H_2 addition to Ar plasma affects plasma electrons and Ar metastable atom densities by collecting concurrent electron and emission data, coupled with modeling. We find that small additions of H_2 cause a large drop in electron densities and Ar metastable atom densities.

In Chapter 4, the effect surface derived hydrocarbons (etch products) have on feeding back on plasma properties was explored. By etching large film areas and real-time measurements of impurity flux and plasma electron behavior, we show that surface derived hydrocarbons behave similarly to injection of gaseous hydrocarbons into the chamber.

In Chapter 5, we apply a plasma-assisted shrink process to decreasing high aspect ratio, highly asymmetric photoresist feature dimensions. We show the dependence of uniform deposition on plasma chemistry, power, and pressure. Better shrink requires low depositing gas chemistries, top-down deposition, and source powers.

In Chapter 6, we investigate the role of initial hydrocarbon film properties on the erosion rates in H_2 and D_2 plasmas. We find that more H rich films etch more quickly than graphitic carbons (in part due to density differences) and that D_2 is more

effective at etching at low energies due to its ions having a lower threshold for physical sputtering.

In Chapter 7, we present data on the influence of isotope effects of reactive impurity addition to inert plasma. We find that D_2 causes similar changes in electron distributions, energies and densities, while having a much different ion mass distribution. As chamber pressure increases, these effects become more important as gas-phase collisions occur at higher rates.

In Chapter 8, we summarize the main findings of this work and discuss future directions.

Chapter 2: Hydrogenation and surface density changes in hydrocarbon films during erosion using Ar/H_2 plasmas

N. Fox-Lyon, G.S. Oehrlein

Department of Materials Science and Engineering and Institute for Research in Electronics and Applied Physics, University of Maryland, College Park

N. Ning, D.B Graves

Department of Chemical Engineering, University of California, Berkeley

Journal of Applied Physics, 110 (10), 104314-104314-9 2011

Abstract

We report interactions of low pressure Ar, H_2, and Ar/H_2 mixture plasmas with a-C:H films. Surface evolution and erosion of a-C:H films were examined for ion energies up to 200 eV by rf biasing the substrates. Film surfaces were characterized using *in situ* ellipsometry, x-ray photoelectron spectroscopy, and atomic force microscopy. Multilayer models for steady-state modified surface layers are constructed using ellipsometric data and compared with results of molecular dynamics (MD) simulations and transport of ions in matter (TRIM) calculations. We find that Ar plasma causes a modified layer at the surface that is depleted of H atoms. The depth and degree of this modification is strongly depending on Ar ion energies. This depletion saturates quickly during plasma exposure (<1 s) and persists during steady-state erosion. We find that the thickness and density of the H-depleted layer are in good agreement with MD and TRIM simulations. The degree of surface densification decreases when small amounts of H_2 are added to Ar plasmas. When more than 5% H_2 is added to the plasma, long term loss in surface density is observed, indicating rehydrogenation and saturation of H in the film. As the H_2 fraction increases, the near-surface atomic H increases and the ion composition bombarding the surface changes. This causes incorporation of H deeper into the a-C:H film. For a-C:H films exposed to pure H_2 plasmas, H is introduced into the near-surface region to a depth of up to ~8 nm from the surface. As the rf bias is increased the ion energy transitions from solely chemical sputtering to one involving physical sputtering, causing the yield of C atoms from the surface to greatly increase. The

increasing yield suppresses H incorporation/saturation and decreases the magnitude of the modified surface layer.

2.1 Introduction

Control of the surface properties of amorphous hydrocarbon (a-C:H) thin films is of interest for many applications: masking layers for semiconductor fabrication,[2.1] tribological coatings,[2.2, 2.3] gas diffusion barriers,[2.4] and biological interface coatings.[5] Depending on the desired use, a-C:H film properties can range from polymeric (H-saturated) to graphitic (H-poor). The density and hardness of a-C:H films directly relates to hydrogen content and sp^2/sp^3 hybridization.[2.6] Film properties can be selected during plasma deposition by changing the deposition gas chemistry, substrate temperature, and ion bombardment energy.[2.7] Modifying a-C:H films and surfaces for improving biocompatibility by plasma modification has been a topic of large interest.[2.8] For photoresist polymers, the surface composition changes due to plasma-surface interactions during etching.[2.9] Ar plasma interaction with polymer photoresist materials can cause the formation of a hard a-C:H surface layer.[2.10] This is due to preferential physical sputtering of lighter atoms over heavier atoms at the surface, leading to carbon enrichment and hydrogen depletion. The formation of a hard a-C:H surface layer over the polymer causes buckling and roughening due to compressive stresses between the layers, which degrades the pattern transfer fidelity.[2.10,2.11]

Studies aimed at predicting and controlling properties of hard a-C:H layers have focused primarily on ion energy and temperature related effects during the growth phase.[2.10] Ion/reactive atom effects on a-C:H surfaces have also been investigated.[2.12-2.14] Total erosion yields ($Y_{total}(E)$) of a-C:H with reactive H atoms

and ions can be described by a combination of the ion energy dependent physical sputtering ($Y_{PS}(E)$) and chemical sputtering ($Y_{CS}(E)$)

$$Y_{total}(E) = Y_{PS}(E) + Y_{CS}(E) \quad (2.1)$$

Physical sputtering is the effect of surface atoms being removed by ion-atom momentum transfer during direct interaction. For physical sputtering of atoms from a-C:H, momentum transfer between ions and target atoms must be greater than that corresponding to the sputtering threshold energy. The number of atoms removed from a surface (Γ_{PS} - number of atoms per unit time and surface area) for *physical sputtering* of a two atom system (a-C:H) can be described as

$$\Gamma_{PS} = \Gamma_C + \Gamma_H = (1 - \frac{n_H}{n}) Y_C \Gamma_i + (\frac{n_H}{n}) Y_H \Gamma_i \quad (2.2)$$

where $\frac{n_H}{n}$ is the fraction of atoms at the surface that are H, *n* the areal density of atoms, Y_C and Y_H are the ion energy and projectile type dependent physical sputter yields for the respective atoms, and Γ_i is the flux of ions to the surface (number of ions per unit time and surface area). When $Y_H >> Y_C$ in hydrocarbons under ion bombardment, the surface will become hydrogen-deficient.[2.15] The erosion rate (thickness removed per unit time) of a film by physical sputtering, ER_{PS}, is then

$$ER_{PS} = ER_C + ER_H = \upsilon_C (1 - \frac{n_H}{n}) Y_C \Gamma_i + \upsilon_H (\frac{n_H}{n}) Y_H \Gamma_i \quad (2.3)$$

where υ_C and υ_H are the volumes occupied per sputtered C and H atoms, respectively. Below the sputtering threshold energy, no physical sputtering is observed. As ions break C-C and C-H bonds below the physical sputtering threshold

energy in the outermost surface layers, plasma reactivity can contribute to additional erosion effects, i.e. *chemical sputtering*. The subject of chemical sputtering of C by H has been thoroughly reviewed by Jacob and Roth.[2.16] Free H atoms from an H_2 plasma, for example, quickly passivate broken bonds and form H_2 and volatile hydrocarbons (C_xH_y). These volatile species diffuse to the surface and are desorbed into the gas phase. Expanded from EQ. 2.2 for individual fluxes from the surface, the sputter rate Γ_{total} of atoms and molecules of C and H by physical and chemical sputtering is represented by

$$\Gamma_{total} = \Gamma_{PS} + \Gamma_{CS} = \Gamma_C + \Gamma_H + \Gamma_{C_xH_y} \tag{2.4}$$

where $\Gamma_{C_xH_y}$ is the sputtering of higher molecular weight compounds enabled through chemical sputtering. At low ion energies and reactive gas chemistries, the conditions dominated by chemical sputtering, C_xH_y is the dominant product. At high ion energies and/or noble gas ion bombardment, Γ_C and Γ_H are much higher than $\Gamma_{C_xH_y}$. The total erosion rate, ER_{total}, of films under physical and chemical sputtering conditions is given by

$$ER_{total} = ER_{PS} + ER_{CS} = \upsilon_C(1-\frac{n_H}{n})Y_C\Gamma_i + \upsilon_H(\frac{n_H}{n})Y_H\Gamma_i + \upsilon_{C_xH_y}(\frac{n_H}{n})Y_{C_xH_y}\Gamma_i \tag{2.5}$$

where $\upsilon_{C_xH_y}$ is the volume occupied by the volatile C_xH_y molecules and $Y_{C_xH_y}$ is the sputter yield of volatile C_xH_y molecules. Like physical sputtering of H atoms, the chemical sputtering process is dependent on the concentration of H atoms. Increasing levels of H atoms at the surface relative to C atoms, causes chemical sputtering to become a larger contributor to ER_{total}. This can be done by creating a more H-saturated film, or by adding H atom bombardment of the surface concurrent to ion

bombardment. The pathways and kinetics of the chemical sputtering effect by ion bombardment and reactive H atoms on a-C:H have been explored at various temperatures and ion energies.[2.12-2.14, 2.17, 2.18] For instance, Hopf *et al*[2.18] formulated a model for the sputter yields of C from hydrocarbon surfaces giving the total yield as

$$Y_{total}(E) = a\int y_{bb}(x,E)n(x,E)e^{-\frac{x}{\lambda}} + Y_{physical}(E) \quad (2.6)$$

where a is a constant factor, $y_{bb}(x,E)$ is the depth dependent bond-breaking events caused by the ion, $n(x,E)$ is the ion range distribution into the surface, and the exponential term is the probability of bond passivation, at depth x, where λ is the typical range of atomic H. Inserting relevant values for bond strength and other material-dependent quantities, they found that the chemical sputtering probability of H ions on graphite, below the threshold of physical sputtering, increased rapidly with ion energy. These modeled values agreed with established data for chemical sputtering of a-C:H under H^+ ion bombardment.[2.18] It also established a model for the maximum escape depth at room temperature of volatile hydrocarbons from hydrocarbon surfaces, relevant to this work.

While chemical sputtering yields of a-C:H have been investigated experimentally using beam systems of H atoms and heavier ions (N^+, He^+, Ar^+), limited data is available on the surface effects that arise during direct erosion in H_2 plasmas.[2.14, 2.19] Previous studies by von Keudell *et al.*[2.20] investigated H_2 plasma erosion of a-C:H films. They found that for hard a-C:H being exposed to H_2 plasmas, a soft, hydrogenated surface layer was formed. Using real-time ellipsometry, they found that when the sample was biased to 90 V the hydrogenated layer was depleted due to compensation by ion bombardment.[2.20] They also found that for H_2 plasma

erosion of soft a-C:H, an H-depleted surface layer is formed with a thickness that is dependent on the ion energy.[2.21] These studies used low pressures (<2 Pa) and explored limited ion energies for hard a-C:H. More so, little work has been done on the surface changes of a-C:H films when exposed to plasmas containing reactive and noble gas mixtures.

The surface changes of materials exposed to complex plasma chemistries is relevant to many current topics of interest in physics. D/T mixtures used in fusion reactors cause surface changes to materials that are radically different than surface changes from H_2 plasmas due to differences in mass and cross section. Changing the mass of one of the surface bombarding species in a plasma cause very different surface effects to a material. a-C:H is a good model material for hydrocarbon systems because of its wide range of tunable properties.[2.7] In the present work, we studied the interaction of Ar, H_2, and Ar/H_2 plasmas with a-C:H films. We report models for the surface modification and erosion of a-C:H films when exposed to Ar, H_2 and Ar/H_2 plasmas at various ion energies and plasma densities.

2.2 Experimental details and methods

Deposition and erosion of a-C:H films was carried out using an inductively coupled plasma reactor that has been described in previous publications.[2.22] Briefly, a 13.56 MHz rf power supply with an L-type matching network powers a planar coil above a quartz window. A substrate electrode was independently biased at 3.7 MHz to control ion energies. The distance between the substrate electrode and the quartz window is 8 cm. Si substrates (2.5 cm x 2.5 cm) were thermally attached to the cooled bottom electrode (10° C). A base pressure of 5 x 10^{-6} Torr was achieved

before deposition of a-C:H films. CH_4 plasma was used for deposition of ~80 nm thick a-C:H films with 20 sccm (cubic centimeter per minute at standard temperature and pressure) flow rate, 300 W source power, and the substrate bias potential set to -200 V. Film properties were extracted from optical modeling of ellipsometric data. Initial film surface sp^2:sp^3 ratios were characterized by vacuum transferring deposited a-C:H films to a VG ESCA Mk II x-ray photoelectron spectrometer (XPS) equipped with a non-monochromatized Mg Kα x-ray source (1253.6 eV). sp^2:sp^3 ratios were found by deconvolving the C 1s peak at 285 eV, and has been established by previous work.[2.23] Initial a-C:H film properties were found to be ~33% H and ~22% sp^3 bond hybridization.

For the erosion of a-C:H films, three different plasma chemistry types were used: Ar, H_2, and Ar/H_2 mixtures. For Ar plasmas, a source power of 300W, a flow of 40 sccm, and a pressure of 1.33 Pa was used. For H_2 plasmas and Ar/H_2 mixture plasmas a source power of 600 W, a total flow of 90 sccm, and a pressure of 4 Pa was used. Plasma densities on the order of 10^{16} m^{-3} (H_2 discharges) to 10^{18} m^{-3} (Ar discharges) were determined by Langmuir probe measurements. Plasma densities of Ar/H_2 mixture plasmas were between 10^{16} m^{-3} to 10^{18} m^{-3} depending on gas percentages. Major components of Ar plasmas interacting with the surface are singly ionized Ar ions/metastables and fast Ar atoms. Surface active components of H_2 plasmas at these pressures/plasma densities are expected to be primarily H^+/H_2^+/H_3^+ ions and reactive H atoms.[2.24] For Ar/H_2 mixtures at 4 Pa the composition of the plasma largely depends on relative concentrations of the Ar and H_2 feed gases. At low % H_2 (<10%), Ar^+ and ArH^+ are the predominant ions. As % H_2 increases, the

average ion mass decreases, i.e. the density of Ar^+ and ArH^+ ions decreases while the density of H^+, H_2^+, and H_3^+ ions increases.[2.25]

Real-time changes during the growth and erosion of the a-C:H films were measured using a single-wavelength (632.8 nm) ellipsometer operating in the polarizer-compensator-sample-analyzer configuration. Data was collected every 200 ms during growth and erosion of a-C:H films. The angle values of ψ and Δ (shown in Figs. 2.1 & 2.6) are related to the film's complex index of refraction and thickness.[26] Atomic force microscopy (MFP-3D, Asylum Research Inc., Santa Barbara, CA, USA) measurements were performed on films in tapping mode (after deposition of a-C:H and after erosion at several conditions) to ensure film topography did not influence optical measurements. Films were found to be smooth after both deposition and erosion in H_2 and Ar plasmas (root mean square roughness < 1 nm). The initial film C:H ratio was fit using an established relationship of the complex index of refraction to the density and H content of a-C:H.[2.7] Ellipsometry, coupled with ion current density measurements, also allowed determination erosion rates and yields of C atoms from the surface.

2.3 Results and discussion

2.3.1 Ar plasma on a-C:H

With direct Ar ion bombardment of a-C:H, physical sputtering of surface atoms is the dominant effect. Heavy Ar atoms sputter light C and H atoms from the surface and cause bond-breaking and displacement of the atoms near the surface. As physical sputtering is related to the relative yields for surface atoms, a relative H:C concentration change can be expected. The relative yield of the H and C atoms is

dependent on their differences in mass and bond strength. During the transient region of time between the initial bombardment and steady-state erosion, the ratio of C:H atoms rapidly changes. The formation of an H-depleted layer can be seen as the sputtering of a binary alloy system, with two atoms of different sputter yields (EQ. 2.2). Calculating concentration change in the modified layer can be carried out by balancing the C and H atomic flux from the surface. In the steady-state erosion regime, where the film thickness is being uniformly eroded, the relative sputter rates ($\Gamma_{C,SS}$ and $\Gamma_{H,SS}$) should reflect the initial film concentration, independent of ion energies.

$$\frac{\Gamma_{C,SS}}{\Gamma_{H,SS}} = \frac{C_C}{C_H} \tag{2.7}$$

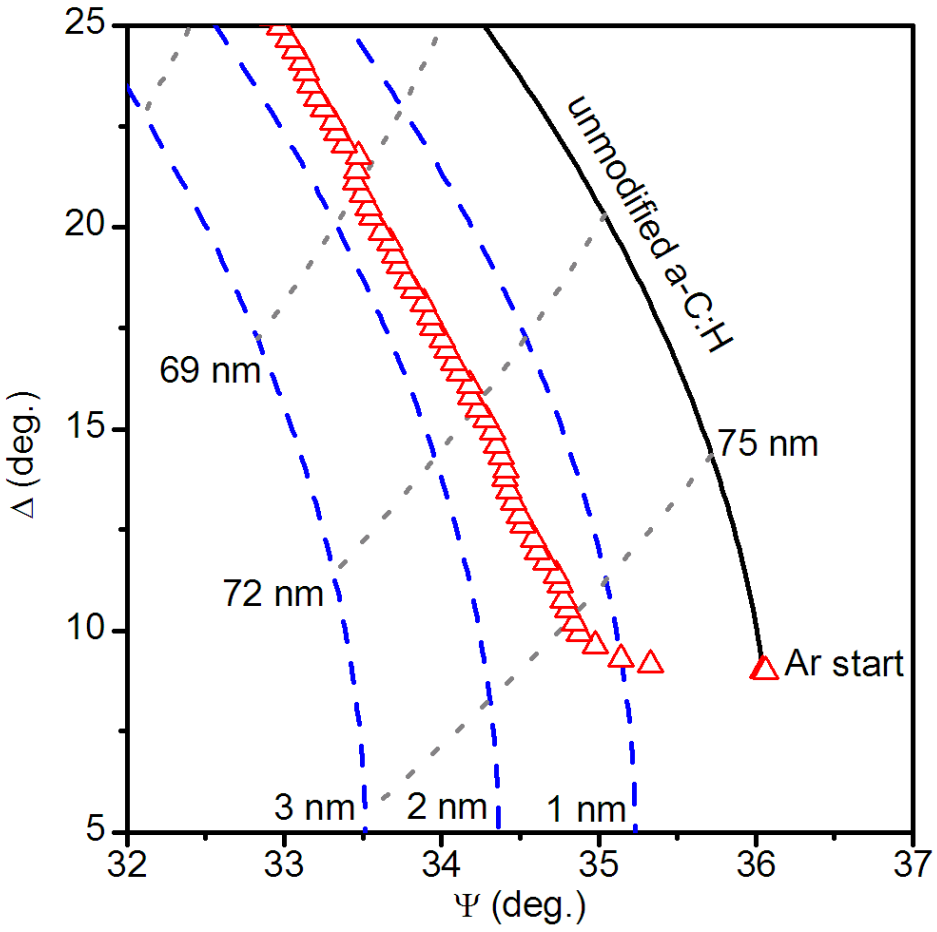

Figure 2.1: *Real-time ellipsometric data and map of the erosion of a-C:H using an rf bias of -200 V for Ar plasma. The erosion data is shown as the open triangles. Data is collected every 0.2 seconds. After ~1 second of erosion (Ar ion flux of 1.5 x 10^{17} ions cm^{-2}, 75 nm unmodified a-C:H thickness) the surface modification is in steady state. The dashed lines parallel to the deposition curve represent 1 nm increments of 11% H a-C:H (n-ik = 2.4-0.55i) on the surface. The dotted lines intersecting the deposition curve represent thicknesses of unmodified a-C:H (n-ik = 2.1-0.06i) in 3 nm increments.*

The loss of H in excess of the concentration ratio in EQ. 2.7 during the transient regime should correspond to an H deficiency in the surface layer. The formation of the H-depleted layer in the transient time regime causes an increase in the density of the film near-surface layers. Additional increases to surface density can be expected through atomic peening, which causes the C atoms to have smaller interatomic spacing.[2.27] This change in density can be characterized in real-time using ellipsometry. Ellipsometric measurements of the film were taken during erosion of a-C:H with Ar plasma and Ar^+ ion energies up to 200 eV. For Ar, the applied rf bias plus plasma potential (7-10 V) gives the maximum ion energy. A map containing the erosion data and simulated film thicknesses of H depletion is shown in Fig. 2.1. From the erosion data, we see a rapid decrease in angles of ψ, followed by an increase in angles of Δ. In this regime, these changes signify an increase in optical density followed by erosion. We recently reported on the sensitivity in this region of ψ-Δ space to changes in an a-C:H film's optical density.[2.28] From the MD simulations (section B.), we predict there to be a hard, H-depleted layer close to the surface. Using MD to estimate the thickness of Ar^+ ion modification on a polymeric material was previously confirmed using XPS deconvolution of valence band spectra and C 1s peak structure degradation post plasma treatment.[2.10] For 200 eV ions, we predict the layer to be ~11% H and ~2 nm thick in steady state. Hopf *et al*.[2.29] reported a relationship for the complex index of refraction to a-C:H H concentration and bulk density. Using this information we find that the unmodified a-C:H has ~33% H and a complex index of refraction n-ik of 2.1 -0.06i and bulk density of 1.9 g cm^{-3}. An a-C:H film with 11% H (n-ik = 2.4-0.55i, ρ = ~2.5 g cm^{-3}) is simulated in thickness

increments of 1 nm above the unmodified a-C:H. Using the ellipsometric data and the optical indexes of the deposited film and a harder a-C:H (at 11% H), we can construct a map for the erosion trajectory (fig. 2.1). We observe that the final steady state thickness of between 1.6 - 1.7 nm (when the erosion data moves parallel to the deposition curve) is slightly lower than the predicted thickness of ~2 nm. This map can be visualized as a multilayer's thickness vs. ion fluence. The Ar plasma erosion of a-C:H's total film thickness vs. ion fluence is shown in Fig. 2.2. Looking at the film in this format shows us how fast this modification saturates into steady-state erosion. Within 1 second of Ar plasma erosion (Ar ion fluence of 1.5×10^{17} ions $cm^{-2}\, s^{-1}$), the total film thickness vs. time (erosion rate) is linear and the modified layer is formed. This erosion rate remains constant until the film is eroded back to the silicon substrate.

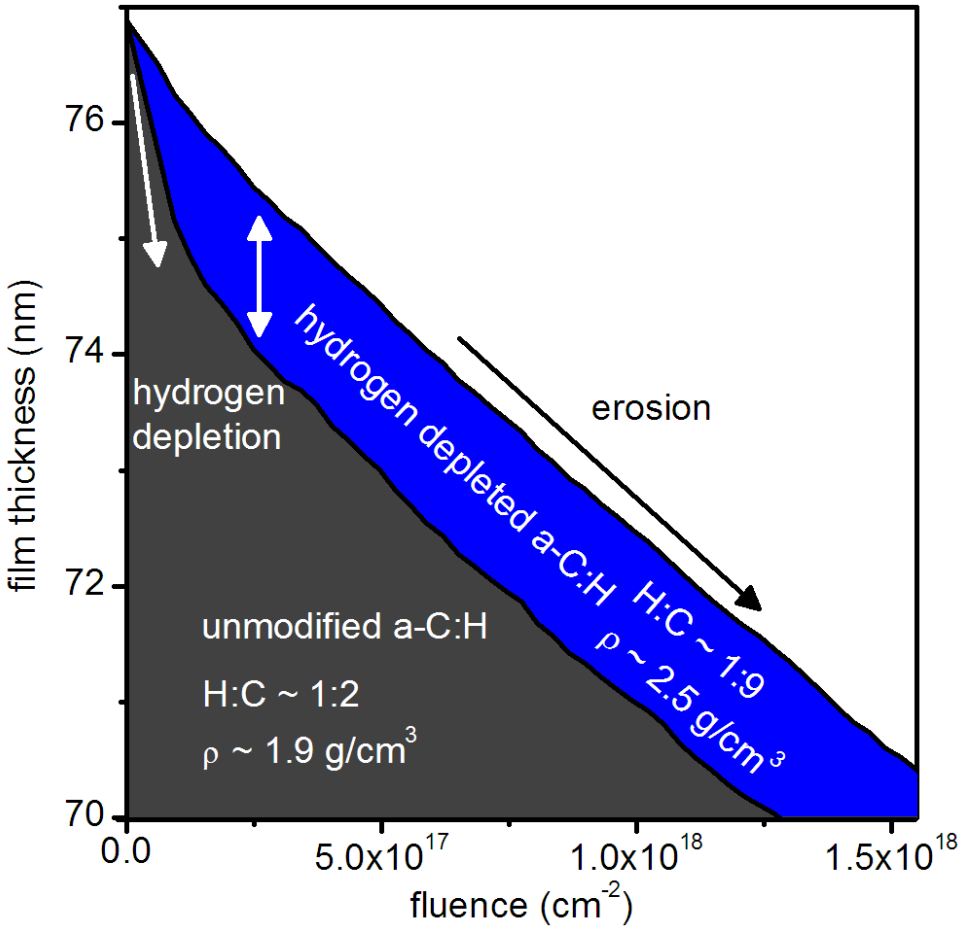

Figure 2.2: *Total and unmodified film thickness vs. fluence for the erosion of a-C:H by Ar plasma (-200 V rf bias voltage). This plot was obtained by extracting the fluence-dependent thicknesses in the multilayer elipsometric model of Ar plasma erosion of a-C:H and using Ar^+ fluence.*

2.3.2 MD simulations of Ar^+ on a-C:H

MD simulations, to examine bombardment of a model a-C:H cell by Ar^+ ions, were performed using a Tersoff–Brenner style reactive empirical bond order potential to describe C-H interactions[2.30] and a Molière potential[2.31] to describe the interaction between Ar and other species. Newton's equations of motion are integrated numerically with the velocity Verlet algorithm using a time step of 0.1 fs. The

Berendsen thermostat was used to control the system temperature. The simulated a-C:H cell was prepared by the following method: first, 30% of the C atoms in a initially diamond carbon cell (2.8 nm x 2.8 nm x 5.6 nm) were randomly replaced by hydrogen atoms, the cell was then heated and equilibrated at 6000 K. After subsequent cooling to 300 K, the surface was relaxed for 30 ps. The total simulation time for one impact is 1 ps. The dimensions of the obtained a-C:H cell were approximately 3 nm x 3 nm and 7.2 nm deep, with 8119 atoms in the initial film and an average density of 2.1 g cm^{-3}. The bottom layer of the cell was kept rigid to avoid transition in space. All atoms in the cell, except those in the rigid layer, were subject to the Berendsen thermostat.[2.9] Periodic boundary conditions were applied in the lateral (x-y) planes of the cell. The initial a-C:H cell properties such as sp^3 fraction and H content have been calculated. The sp^3 fraction in the cell is calculated from the number of four-fold coordinated C atoms over the total number of two-, three-, four-fold coordinated C atoms in the cell.[2.32] We found that the initial a-C:H cell's properties (20% sp^3, 28% H) were close to those obtained experimentally (~22% sp^3, ~33% H). Between each ion impact, the cell was allowed to cool to 300 K before the next ion impact. It is assumed that nothing happens in the cell between ion impacts except the desorption of weakly bound species and cooling. One implication of this assumption is that time between impacts is not included in the simulation procedure. The total simulation time associated with the series of ion impacts (to be compared to experiment) is therefore defined by the number of ion impacts per unit area, or fluence (ions cm^{-2}).[2.33]

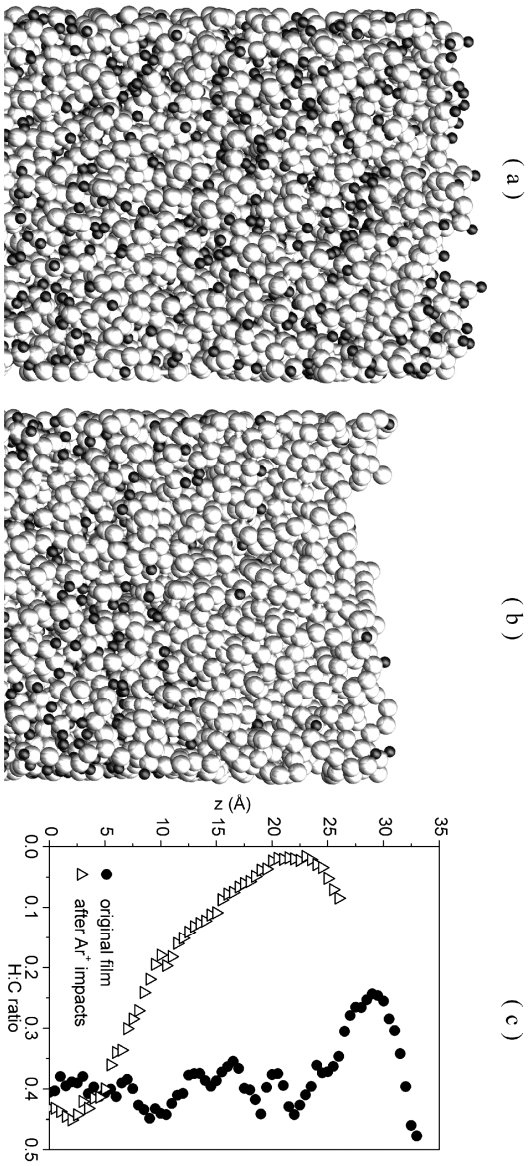

Figure 2.3: *MD simulation cell of a-C:H film (a) before and (b) after 3000 impacts of 200 eV Ar^+ ions (top 3.5 nm of 7.2 nm cell shown). The white atoms represent C atoms, while the black atoms represent H atoms. The difference in height between the cells reflects the loss of thickness and densification due to Ar^+ ion bombardment. (c) Hydrogen-to-carbon ratio depth profile of a-C:H film as a function of depth. Closed circles represent values obtained before Ar^+ ion impacts, while the open triangles represent values obtained after 3000 Ar^+ ion impacts.*

MD simulations of ion impacts are useful for determining concentration and density changes to a-C:H surfaces from a pure non-reactive ion bombardment case. An MD simulation of Ar+ ions impinging on an a-C:H surface for different ion energies was investigated. A side view of the model unit cell surface upon bombardment with Ar^+ ions of 200 eV impact energy is shown in fig. 2.3. Initially (fig. 2.3(a)), the surface and bulk of the cell have a hydrogen concentration of ~28%. After 3000 impacts (fig. 2.3(b)), it was observed that the system is in a steady-state of erosion. Inititial ion bombardment to steady state erosion is observed in fig. 2.4 as a function of the ion fluence. As shown in fig. 2.4, sputter yield decreases up to a certain fluence (about 1×10^{16} ions cm^{-2}) and then becomes constant. The steady-state modified layer thickness and the final H:C ratio was then obtained after 3000 impacts (about 4×10^{16} ions cm^{-2}). The number of ions required to reach saturation is in the same order of magnitude with the fluence measured experimentally. In order to monitor the chemical modification of the near-surface region during ion impacts, the hydrogen-carbon (H:C) ratio in the near-surface region was calculated as a function of the z coordinate (normal to the surface). The 'zero' value of the z coordinate corresponds to the bottom position of the selected near-surface region shown in fig. 2.3(a,b). The average value of the hydrogen-carbon ratio for each z coordinate was obtained from the volume enclosed between two planes with $z \pm 2.5$ Å coordinates. The depletion depth is then defined by the region that the H:C ratio is lower than the original value. The near-surface region showed an increase in density and a change in chemical makeup after ion impacts. The H concentration went from ~28% to ~11% for 200 eV Ar^+ ions. This was quantified by measuring the counting the H:C ratio in

the densified layer. The thickness of the densified layer was found to be ~2 nm. For 50 and 100 eV Ar^+ ions, the H content dropped to ~19% and ~14%, respectively. The H-depleted layer thickness also decreased to ~0.5 nm and ~1.0 nm, respectively. This MD simulated Ar modified and H-depleted layer has previously been reported for the polymer polystyrene using a similar simulation method.[2.9] A similar degree of H depletion was seen for 100 eV Ar^+ on polystyrene as for the present case of 200 eV Ar^+ on a-C:H. The H depletion magnitude and depth for the present study as well as the case for polystyrene noted above are both in good agreement with experimental values found in ellipsometric data and analysis.[2.34]

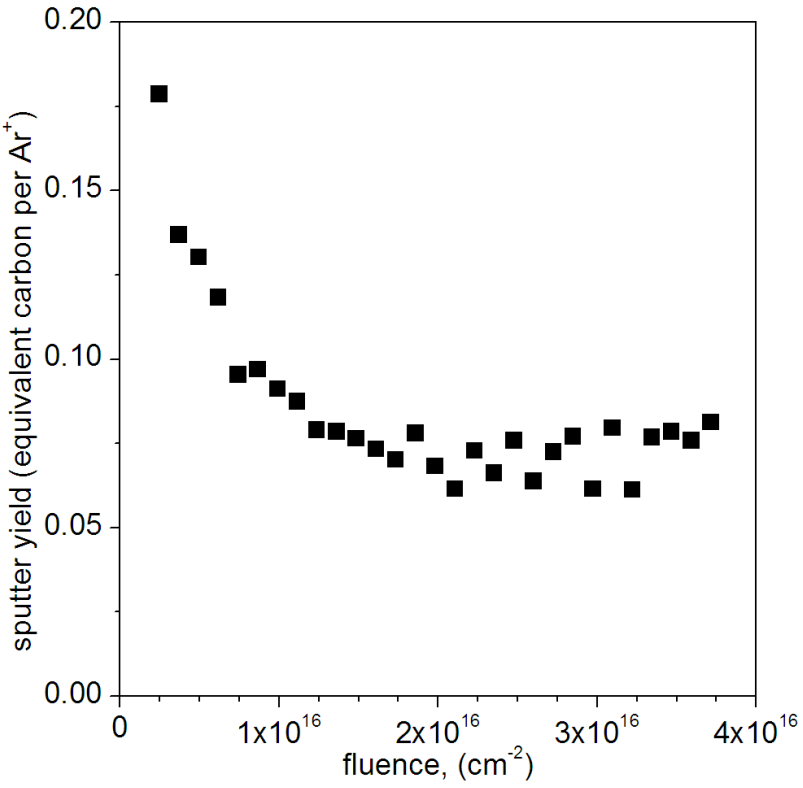

Figure 2.4: *MD calculated C sputter yield as a function of ion fluence during the 200 eV Ar^+ bombardment of the a-C:H film cell.*

With increasing ion energies, an increase in modification thickness and a

decrease in the H:C ratio of the layer was found with MD simulations. By comparing this for all the erosion cases, we can evaluate the MD model. Fig. 2.5 shows the comparison of a-C:H modified layer thicknesses found by ellipsometric monitoring of erosions, for thicknesses found by MD simulations, and TRIM calculated average penetration depths. TRIM calculations were performed using the SRIM program and a-C:H properties similar to those of the experimental film (density, H:C ratio, etc.).[35] The comparison confirms that the MD model is tracking the ellipsometric results well. The MD predicted modified layer thickness as a function of ion energy is in agreement with the estimates from ellipsometry. These values are also in agreement with TRIM-calculated average ion penetration depths. In the ion energy range investigated, the predicted depth of modification is dependent on the ion energy and inversely dependent on the density of the a-C:H material. As the ion energy increases, the average penetration depth increases. If the starting density of the a-C:H is lower, the initial depth of modification will also be higher.

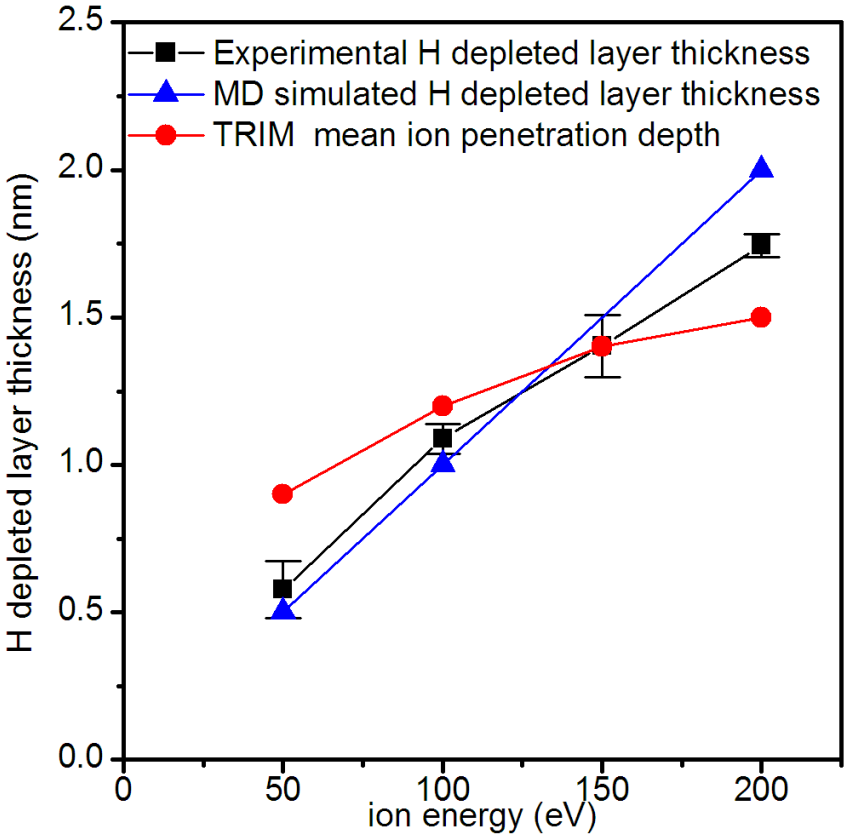

Figure 2.5: *A comparison of the H-depleted layer thickness vs. ion energies for Ar plasma on a-C:H. The triangles connected represent MD simulated thicknesses of the Ar modified layer. The circles represent TRIM calculated average ion penetration depths. The squares represent ellipsometrically determined thicknesses.*

We note that the near-surface changes in composition and density differ significantly from the as-deposited film to the steady state condition. The near-surface region becomes denser and the penetration depth decreases with ion fluence, until a steady state is reached. Ellipsometry is ideally suited for precise in-situ detection of this near-surface evolution.

2.3.3 H_2 plasma on a-C:H

When a-C:H surfaces (of the density and composition used in this study) interact with H atoms and/or hydrogen ions, a soft, polymeric layer is formed at the surface.[2.12] This effect of hydrogenation is of importance for fuel retention in graphite elements facing fusion plasmas of D/T mixtures. Hydrogen is seen to penetrate, even at low substrate temperature and low ion energies, to depths greater than a nm. In Fig. 6, data for the erosion of a-C:H by H_2 plasma is shown. Ellipsometrically (in terms of the angle of ψ), the modification seen is the opposite of the Ar plasma surface densification. ψ and Δ are seen to increase and achieve steady-state erosion parallel to the deposition curve after ~10 seconds (H_2 plasma ion flux of 2.0×10^{17} ions $cm^{-2} s^{-1}$). Superimposed on the plot is the trajectory for the unmodified a-C:H, lines for thicknesses of unmodified a-C:H (~33% H, ρ = ~1.9 g cm^{-3}, n-ik = 2.1-0.06i) in 5 nm increments, and lines for thicknesses of H-saturated a-C:H (~50% H, ρ = ~1 g cm^{-3}, n-ik = 1.55-.001i) in 2 nm increments. As compared to Ar plasma on a-C:H, the formation time to achieve steady state is much longer (10^{18} ions for H_2 plasma at 100 V rf bias vs. 10^{17} ions for Ar plasma at 200 V rf bias). A study of the map shows that as the H-saturated layer forms, the a-C:H film swells to larger than its initial thickness. This is reflected in terms of thickness vs. fluence in Fig. 2.7. The total film thickness is seen to swell in the initial 10^{18} ions before being etched. It is also seen that after the modified layer is formed, the erosion proceeds in a steady-state. At all low substrate bias potentials (-100 V and below) the total thickness swells before material is removed.

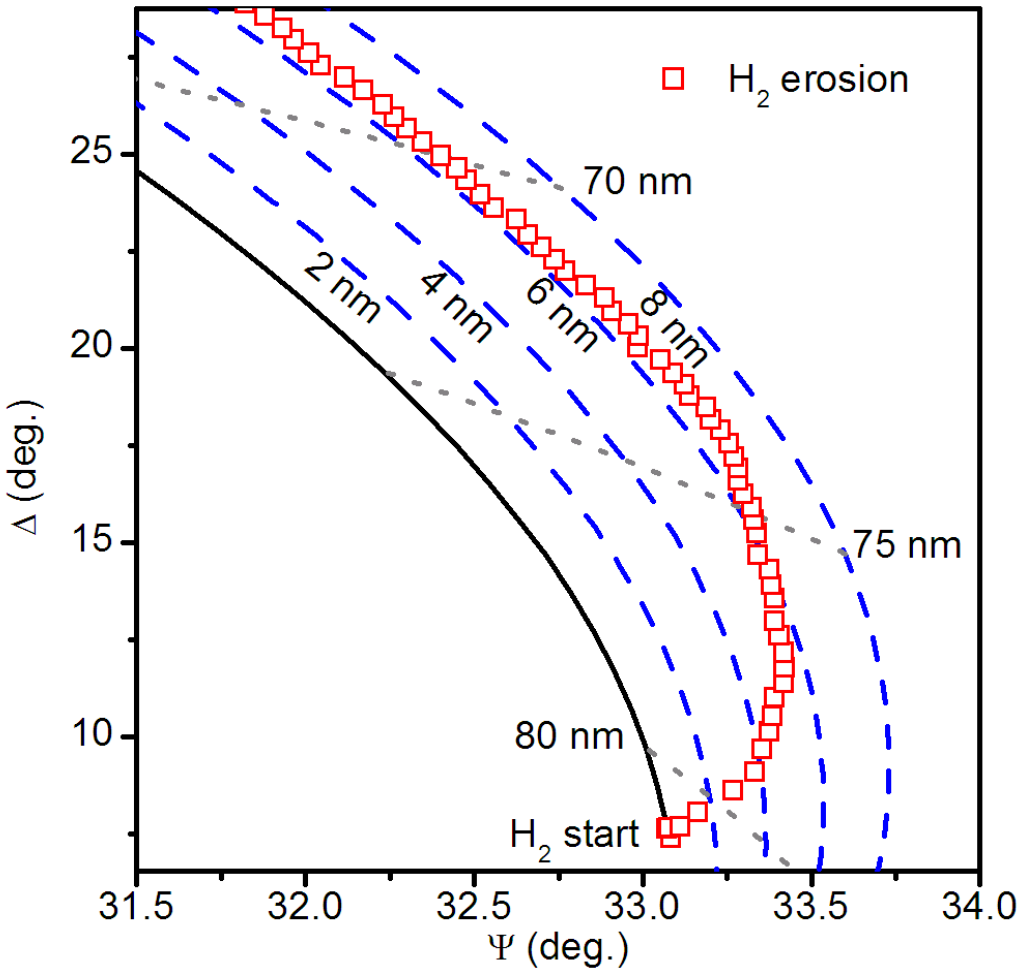

Figure 2.6: *Real-time ellipsometric data and map of the erosion of a-C:H by H_2 plasma (-100 V rf bias voltage). Initial film thickness was 81 nm. Open squares represent erosion data. Data is collected every 0.2 seconds. After ~10 seconds of erosion (H_x^+ ion fluence of 2 x 10^{18} ions cm^{-2}, 75 nm, underlayer thickness) the modification is in steady state. The dashed lines parallel to the deposition curve represent 2 nm increments of ~50% H a-C:H (n-ik = 1.55-0.001i) on the surface. The dotted lines intersecting the deposition curve represent thicknesses of unmodified a-C:H (n-ik = 2.1-0.06i) in 5 nm increments.*

The depth of modification obtained from ellipsometry data simulations of H_2 plasma modification of a-C:H appears to be high. Previous studies of H atom diffusion and H ions on a-C:H predict (for these energy ranges) that the modification depth should be of the order of ~2 nm.[2.20] From TRIM simulations, we expect the ion modified layer to scale with ion energy. From the data, the highest degree of modification is seen for the lowest ion energies (Fig. 8). This behavior may be related to the sputtering regime change that occurs within these bias voltages. EQ. 1 describes the total erosion yield to be related to the sum of the chemical and physical sputtering. At low hydrogen ion energies (< 100 eV), chemical sputtering is the dominant erosion mechanism of a-C:H. Physical sputtering by H^+ ions begins at a threshold of ~35 eV.[2.16] When H^+ ion energy is greater than 100 eV, physical sputtering of a-C:H by the ions becomes the dominant erosion mechanism. As bias voltage is increased, E_i increases. To understand how the degree of modification and C yield are related, it is important to consider the ion characteristics of this discharge. In H_2 plasma, with our chamber geometry and operating powers, the plasma ion type distribution changes greatly with pressure. Gudmundsson showed in a similar ICP plasma chamber with similar H_2 plasma parameters, the ions are mostly a mixture of H_2^+ and H_3^+.[24] At our operating pressure and density, we can expect a near 1:1 ratio of H_2^+ to H_3^+ with only negligible quantities of H^+(less than 1:10 H^+:H_2^+). This is in contrast to previous work exploring H_2 plasmas on a-C:H where low pressures 0.4 to 1.5 Pa) were used and there may have been a higher contribution from H^+. von Keudell *et al.* [2.20] showed that when a 90 V bias was applied to the surface, the hydrogenation effect was diminished. In their work the effective ion energy

deposition could be higher than seen in this study because of a higher degree of H^+ in their work.

At high bombardment energies (greater than 1000 eV), molecular H_2^+ ion interactions with solids can behave approximately as individual atomic ions with each ion having half the energy due to surface-induced dissociation and TRIM simulations can be used to predict penetration and modification of ions to a-C:H.[2.36] As energies decrease, this approximation could break down. In this study, we utilize ion energies up to 200 eV. Low energy molecular ions of isotopes of hydrogen, deuterium and tritium, impinging on a-C:H surfaces have been investigated using MD simulations.[2.37, 2.38] Krstic *et al.* [2.37] showed that, because of charge neutralization by electron capture, dissociation is highly probable for impinging H_3^+ and D_3^+ as they have no stable relaxed state, even with minimal rovibrational energy. Some experimental work exists on how low energy H_2^+ and H_3^+ ions (and molecular ions of other hydrogen isotopes) interact with hydrocarbon surfaces. Harris *et al.* observed that the yields of low energy hydrogen molecular ions (H_2^+, H_3^+) were higher than atomic H^+ ions, when normalized to energy per atom. Energy per atom normalized yields for H_2^+ and H_3^+ over the yield of H^+ were 1.47±.22 and 2.54±0.28, respectively.[2.39] Zhang *et al.* finds a similar increase in molecular ion yields over atomic ion yields using low energy D ion beams on graphite.[2.40]

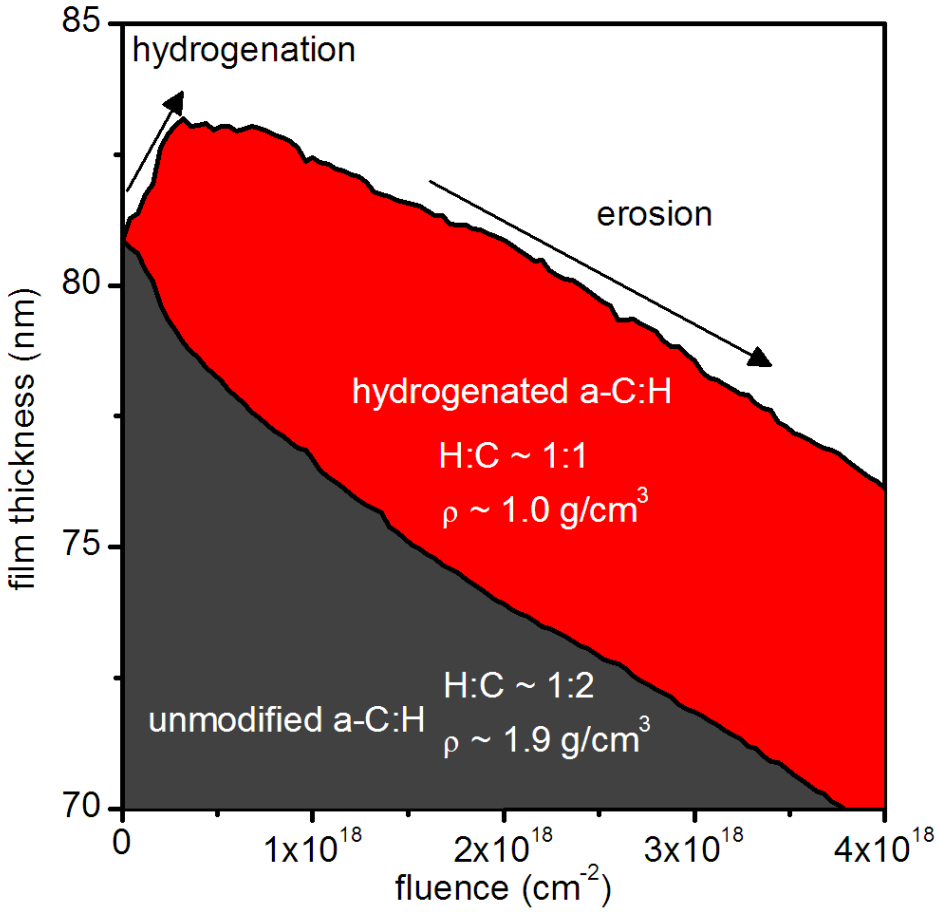

Figure 2.7: *Total and unmodified film thickness vs. fluence for the erosion of a-C:H by H_2 plasma (- 100 V rf bias voltage). This plot was obtained from extracting the fluence dependent thicknesses in the multilayer elipsometric model of H_2 plasma erosion of a-C:H and using H_x^+ fluence.*

In our plasma, with H_2^+ and H_3^+ being the predicted predominant ions in near-equal quantities, we can estimate the average ion energy per AMU by dividing by the bias potential shown on the x-axis of Fig. 2.8. For understanding how the energy deposition and effective energies per impinging atom effect the yield and degree of modification, we assume that all molecular ions impacting the surface of a-C:H behave as individual atomic ions with an equal atomic fraction of the substrate bias

voltage as the energy.[2.16] Applied substrate bias potential could be roughly divided by the average number of atoms per ion and used to calculate the energy per bombarding H atom. A clear change can be seen between 75-100 V (~30-40 eV if divided by 2.5 AMU as the average ion mass), where we expect to first observe some physical sputtering (~35 eV) of the C atoms. Unlike previous beam studies[2.18,2.39] where no increase in the C atom yield is seen experimentally at these low ion energies, we observe a sharp increase in the C atom yield. With an unknown quantity of H^+ in the plasma, this increase seen in yield could also be due to higher energy ions impacting the surface. We also see the impact of this increase in yield on the degree of modification of the material. After this critical energy, the degree of modification drops off rapidly. As the hydrogen chemical modification of upper a-C:H layer is a slower process (diffusion by atoms/dissociated neutrals deeper into the film), the increased sputter yield quickly outstrips its formation.

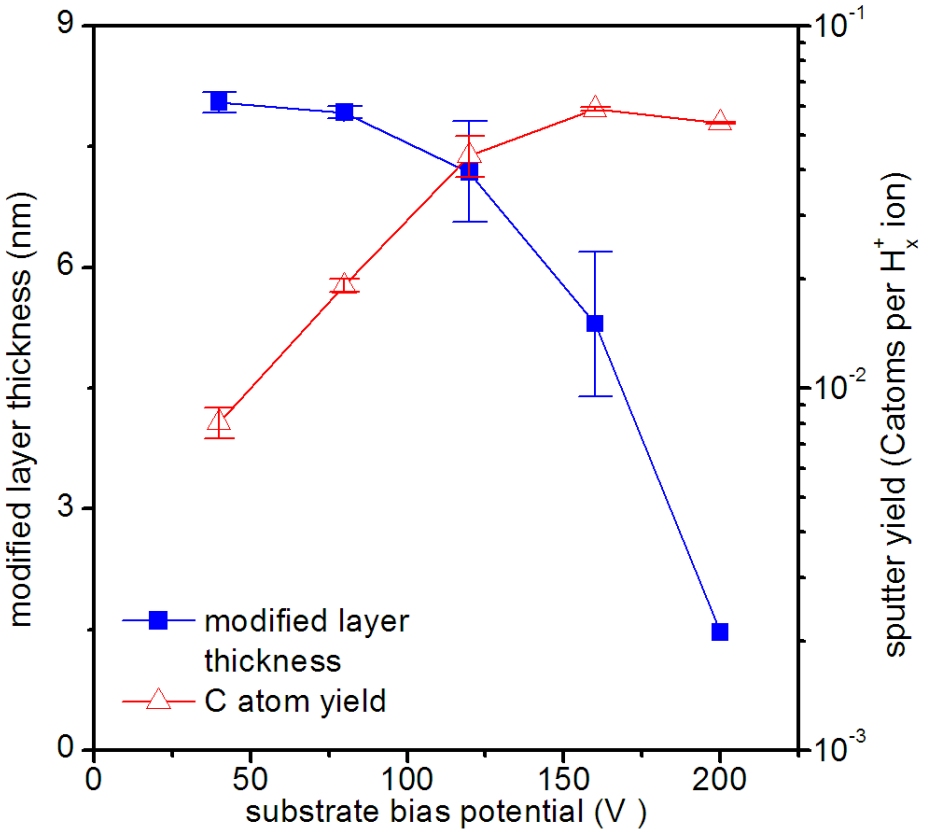

Figure 2.8: *The effect of the substrate bias potential on the hydrogenated layer thickness (closed squares) and C atom yield (open triangles) is shown. As substrate bias potential is increased, C atom yield increases while hydrogenated layer thickness decreases.*

2.3.4 Ar/H_2 plasma on a-C:H

Our investigation shows that Ar and H_2 plasma exposed a-C:H have opposite surface effects. Ar plasma causes surface densification and hydrogen depletion, while H_2 plasma causes surface hydrogenation and the formation of soft, low density a-C:H layers. Ar/H_2 plasma mixtures have properties that change with Ar and H_2 concentrations. When adding small amounts of H_2 to Ar plasma, free H atom concentration near the surface increases. Also, as % H_2 increases the ion type

transitions from Ar^+ and ArH^+ to H^+, H_2^+, and H_3^+. After ~10% H_2 addition, the predominant ions are H_3^+ and Ar^+.[2.25] As H_2 flows increase above this point, H_3^+ becomes greater while amount of Ar^+ is diminished. In Ar/H_2 mixtures, the plasma density is seen to change over a wide range for different chemical compositions. FIG. 9 shows the erosion rate and plasma density vs. flow of H_2 in Ar. At 4 Pa Gudmundsson[24] showed with a plasma mixture of 30% Ar a plasma density of 4.9 x 10^{16} m^{-3} while our experiments shows a plasma density of similar order at 3.0 x 10^{16} m^{-3}. The plasma density is seen to decrease (due to energy lost to H_2 molecular states) rapidly with increasing H_2 flows. While the plasma properties are known to change greatly with different Ar/H_2 stoichiometries, the effect of Ar/H_2 plasma mixtures on a-C:H surface modification and erosion rates has not been previously investigated. The addition of H atoms to a-C:H surfaces being bombarded with heavier ions has been previously shown to increase the erosion yield.[41] Because of the availability of chemically reactive atoms and a mixture of heavy and light ions, we can expect to observe changes to the erosion rate and chemical changes to the surface.

For H_2 addition up to 10%, an increase in the erosion rate is seen (Fig. 2.9). This highlights the increase in erosion yields caused by chemical sputtering, and is due to the increasing availability of reactive H at the surface. From EQ. 5 and the discussion above, we would expect to see an increase in chemical sputtering, along with H incorporation beyond H repopulation, if reactive H atom fluxes are higher than the H atom depletion rates through physical and chemical sputtering. Because the exact ion composition is unknown, accurate sputter yields could not be determined. Above 10% H_2, the erosion rates are seen to decrease. At higher flows of

H_2 in Ar, the erosion rate of the surface may become limited due to insufficient Ar ion bombardment relative to reactive H species. At conditions of pure H_2, the erosion rate is still significantly higher than for pure Ar, while the plasma density has dropped by almost two orders of magnitude.

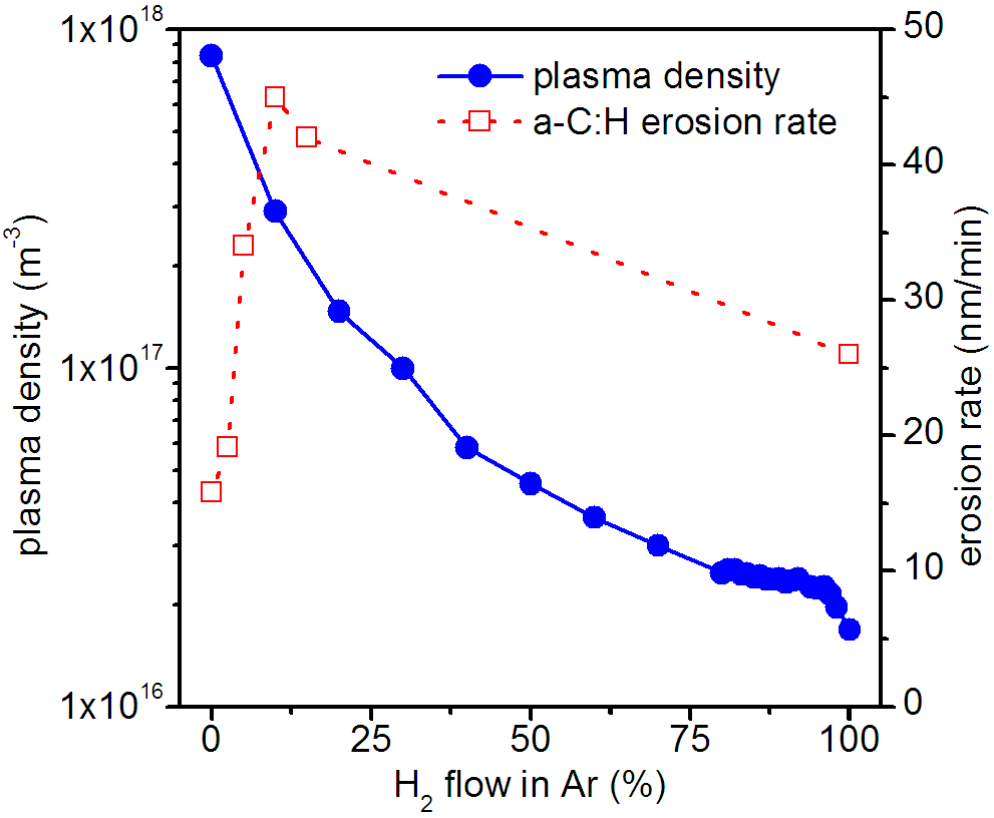

Figure 2.9: *The dependence of plasma density (left y-axis, closed circles with solid line) and a-C:H erosion rate (right y-axis, open squares with dotted line) on the % H_2 flow in Ar during steady-state erosion in Ar/H_2 plasma mixtures is shown.*

For erosion with pure Ar plasma in section A., we found H depletion of the surface. For erosion with pure H_2 plasma in section C., we found H saturation of the surface. The modification of the a-C:H surface varied with plasma Ar:H_2 composition. In Fig. 10, the change in the a-C:H surface areal density of H and C

atoms vs. the flow percentage of H_2 in Ar is shown. The modified layer thicknesses were found using index of refraction values described in sections A and C for H depletion and H saturation, respectively. The changes in the C and H atom areal densities were found using Schwarz-Selinger *et al.*'s[2.7] relationship for a-C:H film % H and density. Using the relationship for density and % H of the modified layers, along with knowledge of the steady-state thickness of modification the C and H atomic density changes were estimated. With small amounts of H_2 addition (2.5% total flow) to Ar plasma, the H depletion caused by Ar ion bombardment is diminished. Through ellipsometric modeling, this is seen as a loss of more than half the modification depth. While optically this can be shown with our two layer model, more realistically the modification depth by the Ar ions should remain constant, independent of $\%H_2$ in the plasma. The difference with increasing % H_2 flow is in the near-surface diffusion of H passifying the broken bonds, the increasing number of H_x ions interacting with the surface, and a diminishing amount of Ar^+ ions. One possible explanation is that this film surface could resemble a two layer gradient structure. Near the surface, the film is saturated with H, while deeper into the film, the H:C ratio is lower than the deposited a-C:H. In Fig. 10, the change in H:C ratio in steady-state illustrates the net chemical effects. At 5% H_2 flow added, there is initial surface H depletion, followed by slight long term hydrogenation. This may be that the initial Ar ions are able to cause many bond-breaking events near the surface, leading to densification until H atoms diffuse in and passify the broken bonds. In steady state erosion, the reactive H atoms are able to create a net loss in surface density. Above

5%, there is hydrogenation to increasing degrees, without an initial densification period.

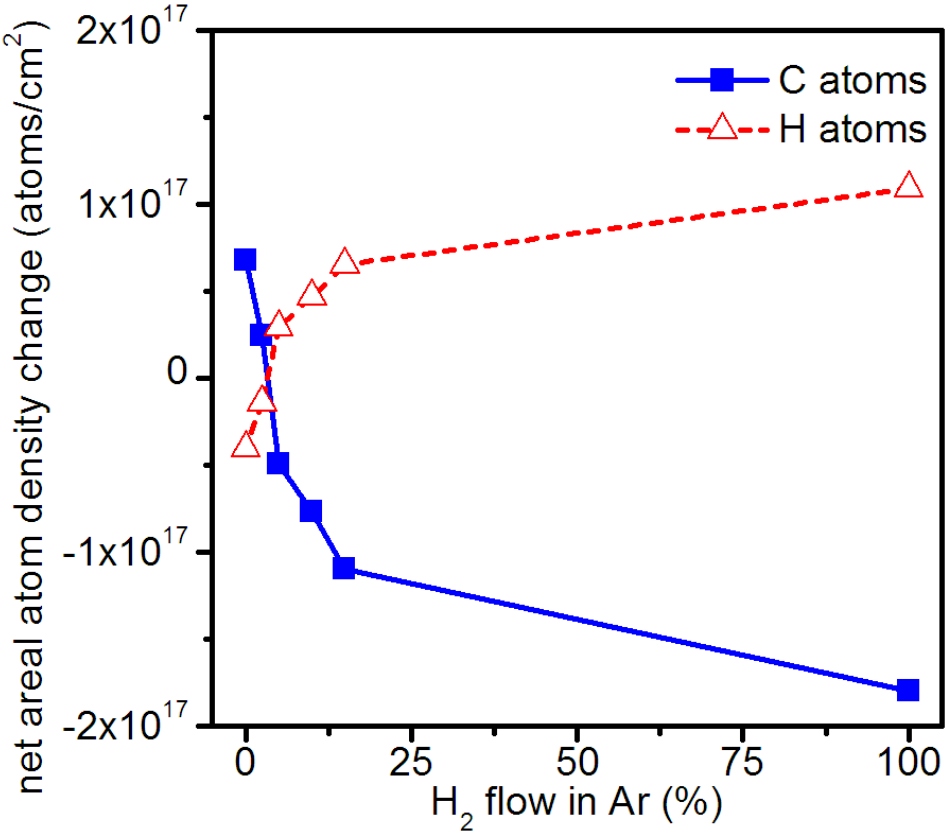

Figure 2.10: *The dependence of net areal atom densities of H (open triangles with dashed line) and C (closed squares with solid line) atoms on % H_2 flow in Ar during steady-state erosion in Ar/H_2 plasma mixtures is shown.*

This large repopulation/hydrogenation to a hydrocarbon surface due to small H_2 additions to Ar plasmas has not been previously reported. In a recent simulation by Maya *et al.*[2.42] 150 eV Ar bombarded a-C:H, followed by bombardment by low-energy, reactive atomic H atoms. This simulation showed repopulation of Ar cleaved C-C bonds by H. This simulation used a highly physical sputtering condition (45° incident angle), so the penetration depths are much shallower than we would expect

for our current experiments. With a significant amount of H_x^+ and reactive neutrals concurrently bombarding the surface, a high concentration of H could be significantly deeper. In future work, we will explore how this competition of effects can translate to polymeric systems.

2.4 Conclusions

In conclusion, the surface modification of a-C:H films with various Ar/H_2 plasma compositions and ion energies has been studied. In agreement with MD simulations, in-situ ellipsometry of Ar plasma on a-C:H shows a large increase in surface density due to selective sputtering of H atoms over C atoms. This depletion leads to the formation of a steady-state, H-poor a-C:H modified surface region. This surface densification increased in thickness and H loss when ion energies were increased. In contrast, H_2 plasmas interacting with a-C:H show a large loss of surface density due to H incorporation and diffusion during erosion. The degree of H incorporation was found to decrease with larger ion energies due to large increases in erosion rate by physical sputtering. During erosion with combined Ar/H_2 flow in plasmas, the effect on the a-C:H surface varied widely. This allows for control of film chemistry and density during erosion by a simple change in chemistry and ion energy. With less than 5% H_2 addition, film surfaces are H-depleted. Above 10% H_2 addition the surfaces show a net loss in density in steady-state. With H_2 addition approaching 100%, the film surface becomes increasingly H-saturated. Characterizing the surface modification of a-C:H using different plasma chemistries with competing chemical effects can help to improve understanding of fundamental plasma-material interactions and process design for device manufacture.

Chapter 3: Determination of Ar metastable atom densities in Ar and Ar/H_2 inductively coupled low-temperature plasmas

N. Fox-Lyon, A.J. Knoll, G.S. Oehrlein

Department of Materials Science and Engineering and Institute for Research in Electronics and Applied Physics, University of Maryland, College Park

J. Franek, M. Koepke

Department of Physics, West Virginia University, Morgantown

V. Demidov

Department of Optics and Spectroscopy, St Petersburg State University, St Petersburg, Russia

Department of Physics, West Virginia University, Morgantown

V. Godyak,

Department of Electrical Engineering and Computer Science, University of Michigan, Ann Arbor

Journal of Physics D: Applied Physics 46 , 2013

Abstract

Ar metastable atoms are important energy carriers and surface interacting species in low-temperature plasmas that are difficult to quantify. Ar metastable atom densities ($N_{Ar,m}$) in inductively coupled Ar and Ar/H_2 plasmas were obtained using a model combining electrical probe measurements of electron density (N_e) and temperature (T_e), with analysis of spectrally resolved Ar plasma optical emission based on 3p → 1s optical emission ratios of the 419.8 nm line to the 420.1 nm line. We present the variation of $N_{Ar,m}$ as the Ar pressure and the addition of H_2 to Ar are changed comparatively to recent adsorption spectroscopy measurements.

3.1 Introduction

Due to the ease of manipulation of plasma-generated atomic and ion species and energies in Ar/H_2 plasma, this plasma mixture is a topic of recent study with applications from cleaning deposits in fusion devices to controlling surface properties of polymers and hydrogenation of transistors.[3.1-3.3] Quantitative measurements of absolute particle (ions, reactive neutrals, metastable atoms, etc.) densities and surface fluxes are required for monitoring this manipulation in these applications. Recently, several research groups have reported measurements and created models for predicting the plasma parameters and ion compositions of Ar/H_2 plasmas.[3.4-3.6] Sode *et al.* recently showed unpredicted results in molecular ion compositions and electron behavior of H_2/Ar plasmas at different chemical compositions.[3.6] Metastable species formation are also important electron energy-loss mechanisms and are significant for surface reactions in Ar plasmas along with H atom creation in Ar/H_2 plasmas, though they are notoriously hard to quantify through direct plasma observation techniques. Ar metastables have long lifetimes, carry significant energy that can be transferred to atoms/molecules causing Penning ionization/dissociation, and occur at high densities in low temperature plasmas.[3.7-3.9] Ar metastable atoms in Ar plasma and Ar plasma mixtures have been used for low-energy patterning of surfaces[3.10,3.11] Quantification of metastables in Ar plasmas[3.12-3.14] and Ar/reactive gas mixtures[3.15-3.17] by optical methods has been a topic of great interest. In the Ar/H_2 global model presented by Kimura and Kasugai, an increase in $N_{Ar,m}$ with small increases in H_2 gas is predicted in Ar plasma at pressures of 20 mTorr and above.[3.4] They predict that further increasing H_2 flow into Ar plasma results in a leveling and a decrease in the $N_{Ar,m}$.

Wang *et al.* have reported accurate $N_{Ar,m}$ measurements for Ar plasmas at different pressures and containing H_2 impurities using absorption spectroscopy. Their measurements show that $N_{Ar,m}$ has a local maxima as pressures are increased and decreases rapidly with H_2 addition.[3.17]

DeJoseph and Demidov used the relative emission intensities of 419.8 nm and 420.1 nm Ar lines to study the behavior of Ar metastable atoms in plasmas.[3.18-3.20] The Ar emission of the 3p to 1s transitions display a unique ratio of intensity depending on whether the 3p state is excited by direct electron excitation or stepwise excitation. The line at 419.8 nm is excited almost exclusively due to direct ground-state excitation while the intensity of the 420.1 nm line strongly depends on $1s_5$ metastable atom density. Boffard *et al.* recently used these line ratios to probe the EEDF of dense inductively coupled Ar plasmas at different pressures.[3.14] These line ratio values of emission intensities of the 419.8 nm line to the 420.1 nm line (radiation from Ar levels $3p_5$ and $3p_9$ populated by excitation from the Ar ground state to the Ar level $1s_5$ metastable state, respectively) can be used in conjunction with electron properties (T_e and N_e) to calculate $N_{Ar,m}$. Using Jung *et al.*'s Ar excitation cross-sections,[3.21] Adams *et al.* used this model to predict quantitative $N_{Ar,m}$ for pulsed Ar plasmas[3.22] and it will be briefly outlined here. The intensity of the aforementioned lines is:

$$I_{420.1} = K_{1a} N_e N_a + K_{1m} N_e N_{Ar,m} \quad (3.1)$$

$$I_{419.8} = K_{2a} N_e N_a + K_{2m} N_e N_{Ar,m} \quad (3.2)$$

where N_a is the neutral gas density, $K_{1a,\ 2a}$ are the electron optical excitation rate constants of the upper levels Ar emission lines from the ground states at 420.1 nm

and 419.8 nm, respectively, $K_{1m,\ 2m}$ are the electron optical excitation rate constants from Ar metastable states at 420.1 nm and 419.8 nm, respectively. These rate constants are determined by:

$$K[cm^3 s^{-1}] = 5.93 \times 10^7 \int_0^\infty \sigma(\varepsilon) fp(\varepsilon) \varepsilon d\varepsilon \quad (3.3)$$

where σ is the cross-section,[3.21] ε is the electron energy, and $fp(\varepsilon)$ is the measured EEDF (found from Fig. 3.1). The $N_{Ar,m}$ can then be calculated numerically by:

$$N_{Ar,m} = (K_{2a} N_a I_{420.1}/I_{419.8} - K_{1a} N_a)/(K_{2m} - K_{1m} I_{420.1}/I_{419.8}) \quad (3.4)$$

This model does not account for contributions to the 419.8 nm emission line due to electron excitation from resonance level Ar atoms. These contributions become increasingly significant above pressures of 5 mTorr.[3.14] Boffard *et al.* showed the number densities of resonance level Ar atoms increased linearly from ~5 mTorr to 15 mTorr before plateauing. This leads to a slight underestimation of metastable density in our measurements at the pressures explored, as the emission of the metastable state decreases above these pressures.

3.2 Experimental details and methods

The experimental plasma characterization work was performed using an inductively coupled plasma (ICP) system described in previous studies. [3.23] A source power of 300 W was applied to a 3 turn coil through an L-type matching network to maximize inductive power coupling to the plasma. A total flow of 50 sccm (standard cubic centimeters per minute at STP) was used for all conditions. For Ar/H_2 mixtures, H_2 flow in Ar (quoted in terms of %) denotes a percentage of total flow volume in sccm units. A downstream throttle valve was used to control operating pressures. The confined plasma region was bounded by a 195 mm diameter ring, with a dielectric-

window-to-bottom-substrate distance of 150 mm. To obtain EEDF, T_e, and N_e, Langmuir probe measurements were performed using a VGPS universal probe system[24] compensated to the drive frequency of the plasma and its harmonics. The plasma density, electron temperature and reaction rates are found as appropriated integrals of the measured EEDF.[3.24,3.25] Optical emission measurements were performed using a SPEX 750M spectrometer (1200 lines/mm grating) equipped with a Hamamatsu PMT and a fiber optic cable that sampled the plasma 100 mm from the dielectric window. The emission of interest (419.8 nm to 420.1 nm) was resolved by scanning in increments of 0.01 nm.

3.3 Results and discussion

The effects of Ar pressure and H_2 additive gas on plasma species on the EEDF are shown in Fig. 3.1. Increasing pressure from the baseline curve of 10 mTorr increases the density of the plasma (area under the curve) and decreases T_e (average electron energy). This density increase and electron cooling effect is due to an increase in electron-neutral collisions at higher pressures. H_2 addition to Ar decreases the plasma density and increases T_e. Unlike Sode *et al.*'s observations of the EEDF shape and integral, at our conditions, the measurements show only slight changes in average electron energy (slope of EEDF in its Maxwellian part) while N_e is seen to decrease drastically. This loss in density with only slight increase in electron energy is due to H_2's additional electron collisional energy losses of molecular dissociation and excitation of vibrational and rotational energy levels.[3.4]

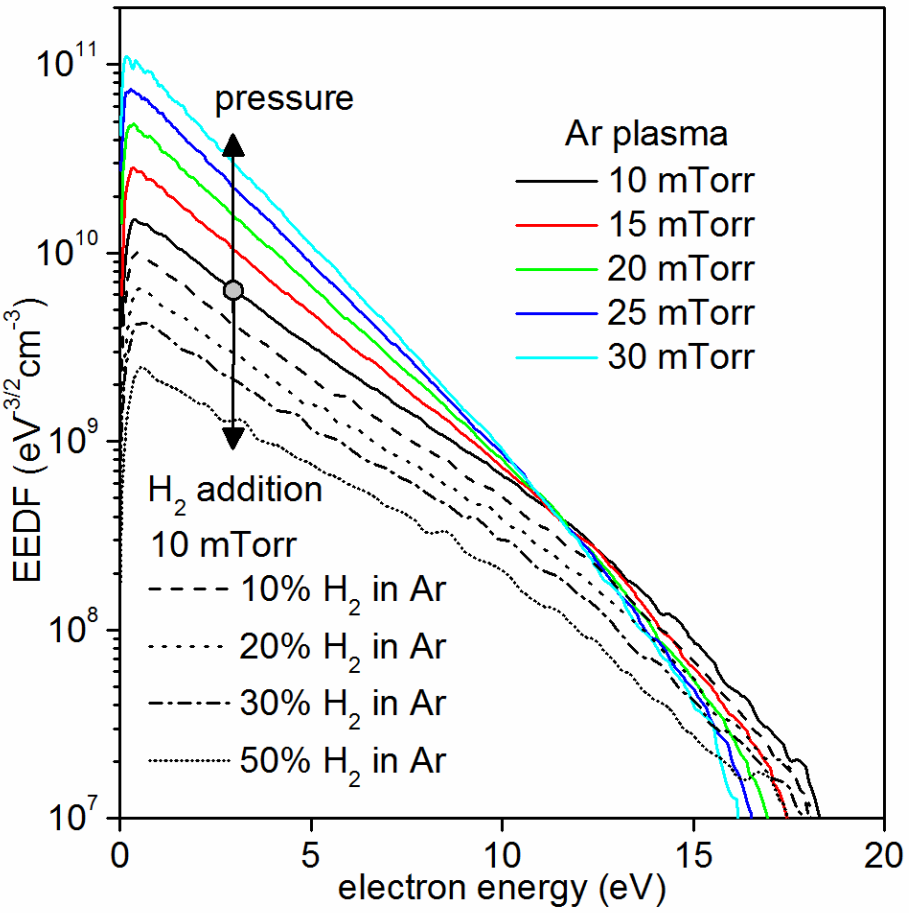

Figure 3.1: *Electron energy distribution functions of Ar plasmas at different pressures (10-30 mTorr) and H_2 flow additions (at 10 mTorr with additions from 10% to 50% H_2). Coloured lines represent different pressure Ar plasmas, while the broken lines represent different H_2 admixtures to Ar plasmas. The solid black line represents the baseline condition (10 mTorr, 300 W) used for H_2 flow additions. The range of EEDFs validity is limited by the level of $2x10^7$.*

Varying pressure and H_2 additive gas has two opposite effects on T_e and density. The change in electron properties with pressure and H_2 additive parameters is shown in Fig. 3.2(a,b). Fig. 3.2(a) shows that T_e decreases from ~3.4 eV at 5 mTorr

to ~2 eV at 30 mTorr while N_e increases from ~5 x 10^{10} cm^{-3} at 5 mTorr to ~3.5 x 10^{11} cm^{-3} at 30 mTorr. Godyak *et al.* found similar effects of pressure on T_e, N_e, and EEDF's in comparable inductively coupled Ar plasmas.[3.23] Fig. 3.2(b) shows that, at 10 mTorr, H_2 addition increases T_e from ~2.9 eV at 0% H_2 addition to ~3.2 eV at 30% H_2 addition and decreases N_e from ~8 x 10^{10} cm^{-3} at 0% H_2 addition to ~3 x 10^{10} cm^{-3} at 30% H_2 addition. This large decrease in N_e has been observed previously for H_2 addition to Ar plasma.[3.4-3.6,3.27] The electron properties obtained from the EEDF data (Figs. 3.1 and 3.2) were inserted into EQ. 3.3 for finding reaction rates.

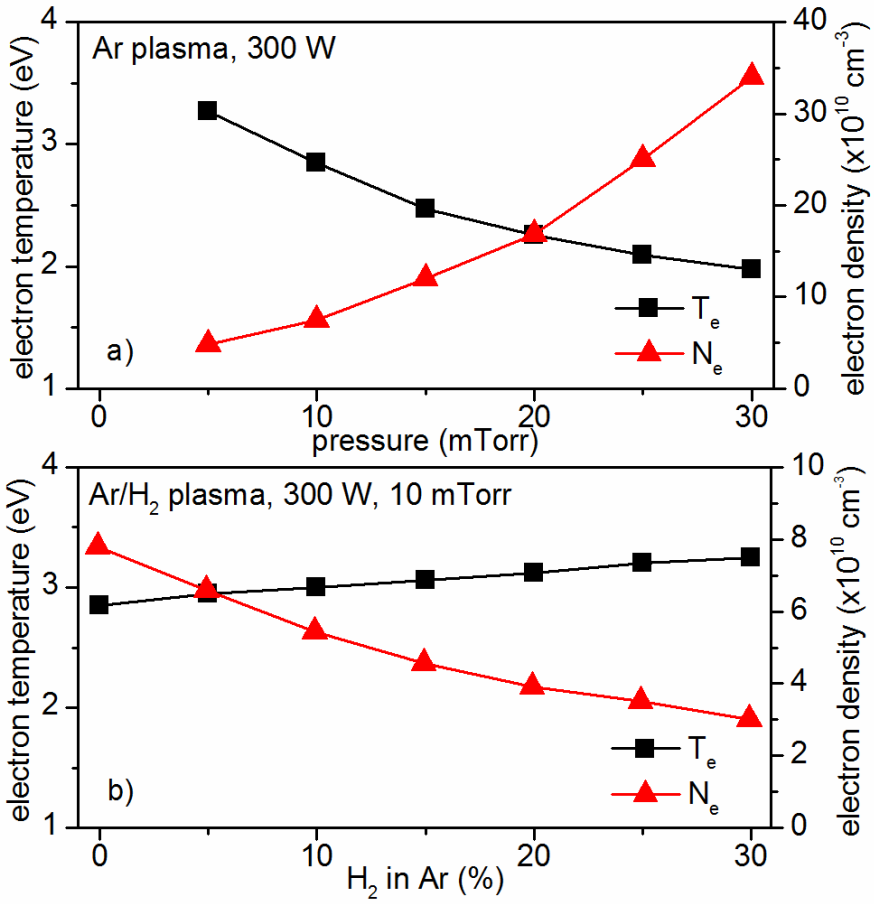

Figure 3.2: *T_e's (triangles) and N_e's (squares) of (a) Ar plasmas at different pressures (10-30 mTorr) and (b) H_2 flow additions (at 10 mTorr with additions from 0% to 30% H_2).*

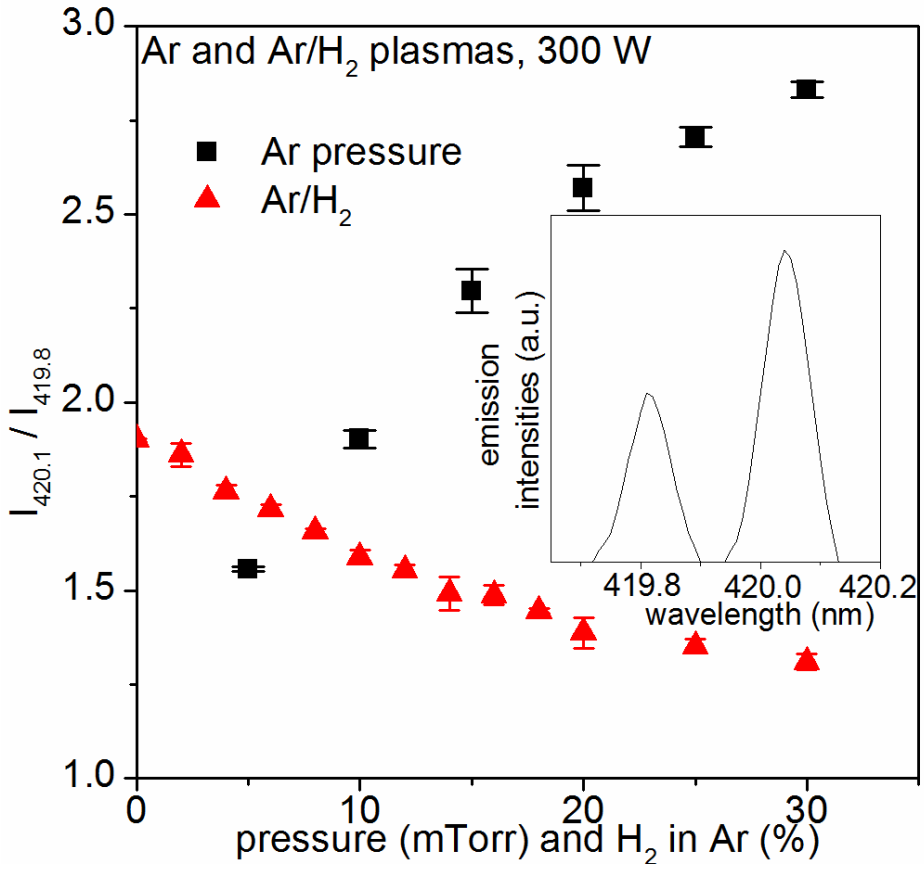

Figure 3.3: *420.1 nm and 419.8 nm emission ratios of Ar plasmas at different pressures (squares, 5-30 mTorr) and H_2 flow additions (triangles, 10 mTorr with additions from 0% to 30% H_2). Inset shows baseline emission profile data of region around the two peaks Ar plasma at 10 mTorr, 300 W condition.*

The final calculated values of $N_{Ar,m}/N_e$ ratio for the Ar pressures series and the H_2 addition to Ar series are shown in Fig. 3.4. For Ar, increasing pressures decreases $N_{Ar,m}/N_e$. This can be explained by increased collision-induced cooling at higher pressure decreasing electron temperatures that are relevant to excitation. While the relative density decreases, $N_{Ar,m}$ encounters a localized maximum between 10 and 15 mTorr, a range that lowers at higher/lower pressures. This increase could result from

N_e increasing faster than T_e decreases once T_e decreases below the threshold for excitation. The model is in agreement with previously published studies of Ar plasmas pressure dependencies showing an increase in density with pressure.[3.12,3.14,3.16] The decrease in $N_{Ar,m}$ is in agreement with Boffard *et al.*'s result using laser absorption at pressures higher than 10-15 mTorr (in a much denser Ar plasma).[3.16] In Ar/H_2 plasmas, $N_{Ar,m}$ decreases with addition of H_2, in agreement with the absorption spectroscopy measurement of Wang *et al*.[3.17] A localized increase of $N_{Ar,m}$ was not seen at low flows of H_2 in Ar cases as seen in Kimura and Kasugai's global model simulations.[3.4] Unlike increasing the pressure, H_2 addition caused no localized increase in $N_{Ar,m}$, since it H_2 addition results in no increase in the value of N_e. Small changes (~10%) in T_e seem to have little effect on modeled $N_{Ar,m}$ it seems to follow the decrease in N_e.

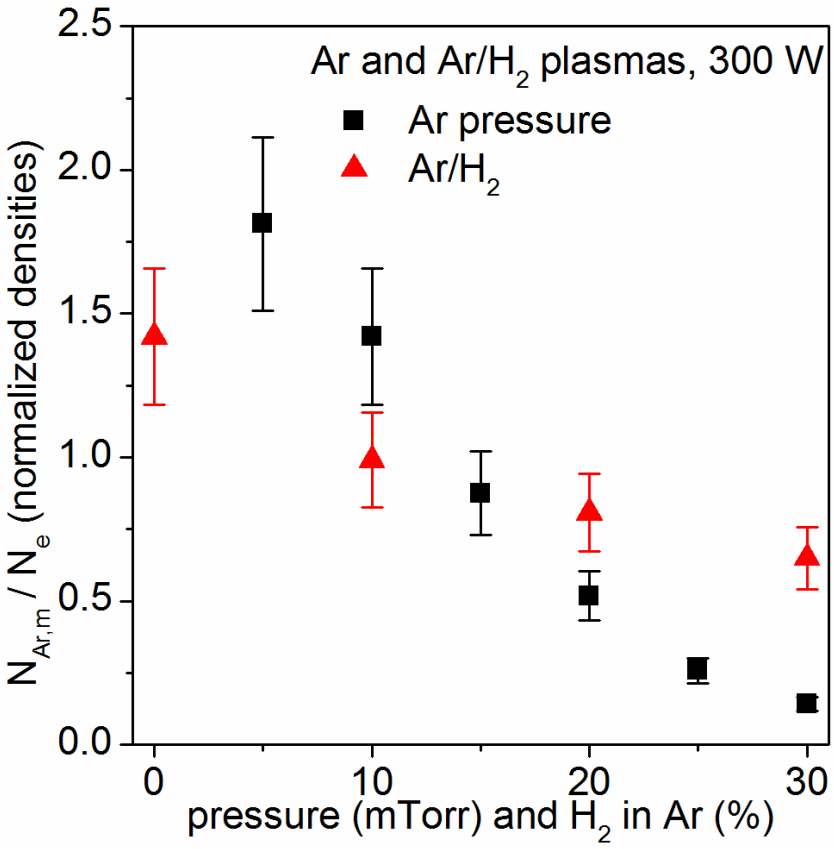

Figure 3.4: *Ratios of modeled $N_{Ar,m}$'s normalized to N_e's of Ar plasmas at different pressures (squares, 10-30 mTorr) and H_2 flow additions (triangles, 10 mTorr with additions from 0% to 30% H_2).*

This method could be useful qualitatively in situations where Langmuir probe and laser absorption methods are unavailable for measuring T_e and N_e (e.g. an industrial plasma processing tool). With knowledge of the 420.1 nm / 419.8 nm line intensity ratios and changes to absolute intensities, relative $N_{Ar,m}$ behavior can be qualitatively estimated directly from optical emission spectroscopy. Absolute values require accurate measurements for T_e and N_e. In Ar/H_2 plasmas using this method, $N_{Ar,m}$ appears to be qualitatively insensitive to small uncertainties in T_e and N_e. If only optical emission spectroscopy measurements were available, the 420.1 nm /

419.8 nm line intensity ratio decrease of ~65% over the parameter space follows qualitatively the behavior of $N_{Ar,m}$. With full information of T_e and N_e , the model allows for a quantitative expression of $N_{Ar,m}$ decreasing to ~55% its original value. For Ar plasma at different pressures, with both the T_e and N_e varying highly, this method becomes less effective without knowledge obtained using both Langmuir probe and 420.1 nm / 419.8 nm line intensity ratios.

3.3 Conclusions

In summary, we used electrical and optical plasma characterization data in combination with cross section data and a model of the population/deexcitation of Ar excited states to obtain $N_{Ar,m}$. EEDF measurements reflect increases in N_e and decreases in T_e as Ar pressure increases, while H_2 addition causes large decreases in N_e and marginal increases in T_e. Emission ratios of the 420.1 nm to 419.8 nm line increase as pressure is increased, while a decrease in intensity is seen for increasing H_2 addition. In low pressure Ar plasmas, Ar metastable atoms have the highest density if normalized to plasma N_e. As pressure increases, the N_e increase outpaces the increase in $N_{Ar,m}$, which levels off around 30 mTorr due to a drop in T_e. With the addition of H_2, a relative decrease is seen in $N_{Ar,m}$ relative to N_e, but without as sharp of a decline as with pressure. This optical method has shown to be useful for obtaining Ar metastable densities with satisfactory accuracy and precision at different plasma pressures and with H_2 gas additions, in agreement with rigorous quantitative diagnostics seen in literature.

Chapter 4: Effect of surface derived hydrocarbon impurities on Ar plasma properties

N. Fox-Lyon, G.S. Oehrlein

Department of Materials Science and Engineering and Institute for Research in Electronics and Applied Physics, University of Maryland, College Park

V. Godyak,

Department of Electrical Engineering and Computer Science, University of Michigan, Ann Arbor

Journal of Vacuum Science and Technology A, submitted

Abstract

We report on Langmuir probe measurements that show that hydrocarbon surfaces in contact with Ar plasma cause changes of electron energy distribution functions due to the flux of hydrogen and carbon atoms released by the surfaces. We compare the impact on plasma properties of hydrocarbon species gasified from an etching hydrocarbon surface with injection of gaseous hydrocarbons into Ar plasma. We find that both kinds of hydrocarbon injections decrease electron density and slightly increase electron temperatures of low pressure Ar plasma. For low percentages of impurities (~1% impurity in Ar plasma explored here), surface-derived hydrocarbon species and gas phase injected hydrocarbon molecules cause similar changes of plasma properties for the same number of hydrocarbon molecules injected into Ar with a decrease in electron density of ~4%.

4.1 Introduction

Plasma-surface interactions are dominated by high energy species (ions, photons, metastable atoms, fast neutral atoms) and reactive species (dissociated atoms and molecules). Inadvertent addition of reactive impurities to inert plasmas affects plasma properties and processing using these discharges. For example, Ar plasmas with small N_2, O_2, and H_2 admixtures show large changes in plasma properties.[4.1-2] In particular, H_2 addition impacts ion chemistry, electron energy distribution, and metastable atom densities.[4.1,4.3-4.4] The source of these reactants is not limited to gas flow into the chamber; the processing chamber walls can also release reactants into the plasma. This effect has been demonstrated for chlorine plasma-based etching of silicon.[5] The sensitivity of plasmas to reactants demonstrates the importance of controlling impurities derived from the reactor walls.[4.6] Common plasma chamber sidewalls are conditioned stainless steel alloys, with minimal outgassing of impurities into the chamber during plasma processing. Deposition of volatile films onto these walls can lead to release of reactant species during plasma processing.

Quantification of wall-derived reactant species is important for improving current and future plasma processing applications.[4.7] The effect of impurities/etch products derived from surfaces interacting with plasmas has been looked into for process endpoint detection. Endpoint detection by electrical and spectroscopic characterization techniques of plasma processes has been used extensively in device manufacture to determine when to stop etching.[4.8-4.10] Endpoints of processes can be detected by optical changes when the surface derived species no longer emit while

changes to the electrical properties of the plasma (*e.g.* the electron density (N_e), electron temperatures (T_e), rf bias impedance, etc.) can also tell the state of surfaces, walls, and gaseous species flowing into the plasma.[4.10]

Hydrocarbon-Ar plasma interaction is of great interest for multiple applications. Hydrocarbon gas (CH_4, C_2H_2, etc.) additions to Ar plasmas are used for deposition of carbon films and synthesis of nanoparticles.[4.11,4.12] Ar plasmas are used for etching polymeric hydrocarbons (such as photoresists). As substrate areas increase and atomic layer control of etching surfaces becomes necessary, controlling the densities and energetics of plasma species will be very relevant.[4.13,4.14] Carbon coated walls have also been proposed for improving etch process reproducibility and species control.[4.15,4.16] In applications where significant flows from etching hydrocarbon surfaces could cause unanticipated changes to plasma properties, it will be important to predict changes to plasma properties. In this study we look at the effect of such effects on electron energy distribution functions (EEDF), to see how the N_e and T_e are affected by surface derived hydrocarbons, and how these changes compare to changes caused by gaseous hydrocarbon impurities.

4.2 Experimental details and methods

The work was performed in an inductively coupled plasma reactor with a coil driven at 13.56 MHz for plasma generation through a dielectric window. For etching films a cooled substrate was biased at 3.7 MHz for controlling ion energies.[4.17] A base pressure of $<5x10^{-6}$ Torr was reached before igniting plasmas to minimize residual chamber impurities (environmental adsorbed O_2, H_2O, N_2, etc.). Ar plasmas were then run for 5+ minutes to achieve steady-state wall heating to prevent time-

dependence in measurements. Precise flow of gas impurities was performed using a parallel stabilizing gas line in conjunction with an automatic butterfly valve, allowing for input of the correct flow of depositing gas at high speeds without a large pressure increase. To emphasize minute impurities in the plasma, 40 sccm was the total combined flow rate of Ar and hydrocarbon gases (CH_4 admixtures and surface derived hydrocarbon species). The Langmuir probe used in this study is designed to collect highly accurate measurements of EEDF, N_e, and T_e under depositing plasma conditions by fast sweep speeds, ion bombardment, and electron heating.[4.18] Between each voltage sweep, a brief period of intense ion bombardment (at -30 V) and a small period of electron heating (at +35 V) kept the iridium probe clean and glowing. This prevents build-up of insulating layers and ensures that the work function remains constant, allowing for high confidence in measurements near the plasma potential during sweeps. Collection of plasma properties can be done continuously, allowing for time-resolved monitoring during the plasma process.[18]

To achieve varying C_xH_y flows during surface-derived hydrocarbon-plasma interaction studies, amorphous hydrocarbon (a-C:H) films were grown with surface areas ranging from 25 mm^2 – 130 mm^2 and subsequently placed onto the substrate. Plasma conditions for similar films in this system have previously been described.[4.19] In this study, films were grown without substrate bias in CH_4 plasmas, leading to polymeric, H-saturated hydrocarbon films. During growth, films were optically characterized according to a-C:H index-chemical described by Schwarz-Selinger *et al.*[4.20] The optical index of these films was n=~1.55 which is equivalent to a ~48% H film with a density of 1 g cm^{-3}.[4.20] Typical species etched at low Ar ion energies from

these a-C:H films are C and H atoms, H_2 molecules and unsaturated/saturated hydrocarbon molecules (subsequently called C_xH_y). a-C:H films were monitored during plasma exposure using in-situ ellipsometry to find surface→plasma C_xH_y fluences. Using measured erosion rates as well as the hydrocarbon surface area and composition, we calculate equivalent C_xH_y flows into the plasma. Flow % of C_xH_y in Ar was approximated as the number of C atoms being removed for clearer comparison to CH_4. Substrate biases to obtain >1 % total flow from the surface ranged from -25 V to -100V, achieving etch rates greater than 25 nm/min. When a-C:H is not present on the substrate, these biases induce negligible changes to electron population properties (EEDF, N_e, and T_e) using appropriate filtering techniques.4.[21] As this lower driving frequency inefficiently couples to electrons, substrate bias does not cause significant increase in the sheath length and ion currents are constant in this Ar plasma–substrate bias regime. Without applied bias, a-C:H erosion rates are minimal (<1 nm/min), allowing for chamber heating/conditioning and baseline probe traces before significant carbon introduction. CH_4 addition causes deposition onto cool, remote, unbiased surfaces in the plasma such as the substrate, sidewalls, and the dielectric window.

4.4 Results and discussion

The introduction of small flows of CH_4 had an immediate impact on plasma properties. Figure 4.1 shows the effect of CH_4 flow on the Ar plasma EEDF. With the introduction of CH_4 into the plasma, the N_e drops, especially those with lower energy. By 4% addition, almost a 30% decrease in EEDF integrated area is seen. The depletion of low energy electrons can be explained, in part, by electron energy

coupling to CH_4 dissociation and molecular states. A similar effect was observed in recent studies with H_2 addition to Ar plasmas.[4.3,4.22,4.19] The overall decrease in electrons is due to decreasing degrees of ionization with CH_4 addition. Due to deposition onto grounding surfaces facing the plasma (and non-negligible increase in the sheath resistance), the peak of the EEDF begins to shift to higher energies with CH_4 addition. The effect of surface derived hydrocarbons on the plasma is also displayed and shows a slight decrease in low energy electrons (similar to CH_4 addition). As the flows from the surface are much smaller than the CH_4 flows, this impact on plasma properties is much less. The maximum equivalent flow from the surface for these cases is ~1%.

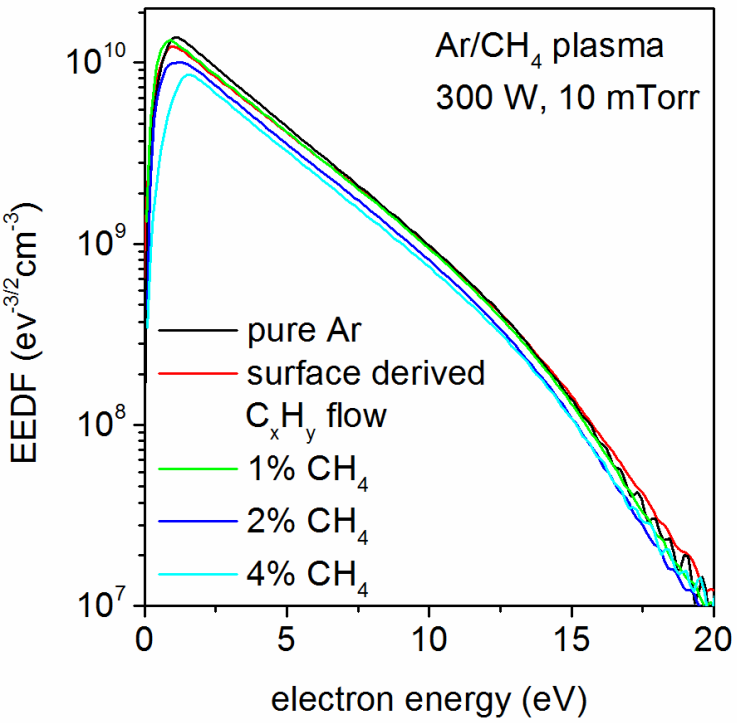

Figure 4.1: *Electron energy distribution functions of Ar plasmas with varying amounts of CH_4 added to plasma from surface and gaseous sources. EEDF measurements have high accuracy to ~<5 x 10^7 $eV^{-3/2}cm^{-3}$.*

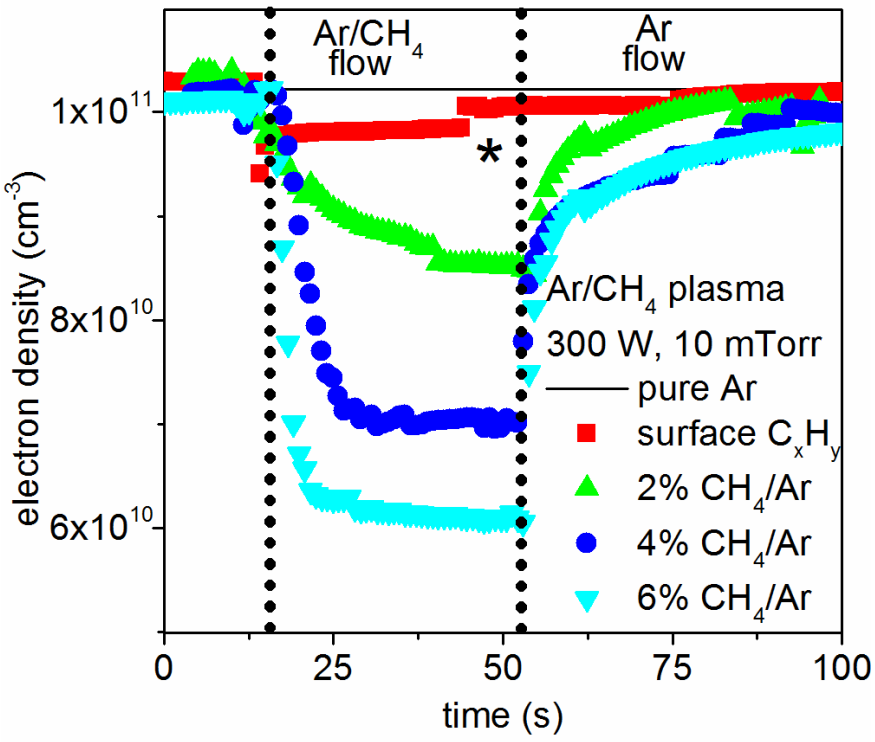

Figure 4.2: *The time-dependent effect of C and H flow into the plasma. CH_4 flow or bias are switched on (at ~20 seconds), increasing the flow of C and H into the plasma. CH_4 flow or bias is switched off (at ~50 seconds), decreasing the flow of C and H into the plasma. The '*' denotes the surface C_xH_y case when the substrate bias was switched from -100V to -50V. In this case, stabilizing the voltage and achieving steady-state surface etching took several seconds.*

The changes caused by hydrocarbon addition to Ar plasma are time-dependent and reversible. Fig 4.2. shows the response of Ar plasma electron density to hydrocarbon addition with time. When CH_4 is introduced into the chamber, N_e quickly drops. The small, quick spike in N_e observed for some cases is due to a transient pressure increase due to valves switching before stabilization. For most cases (besides the low, 2% CH_4 case) the decrease in electron temperature stabilizes and saturates within ~10 seconds. The slower saturation of the 2% CH_4 case may be due to the initial depletion of most CH_4 from the plasma from deposition onto the substrate and exposed walls. After CH_4 flow is turned off, the electron density recovers to initial levels. At higher flows (above 2%) this effect takes longer, likely due to a buildup of volatile hydrocarbon species on the walls. Surface derived C_xH_y has a faster rate of interaction upon the Ar plasma. The case shown here is a surface etched at -100V, before being switched to being biased at -50V, and finally with bias turned off. The source of C_xH_y, in this case, is immediately removed from the chamber and the plasma relaxes to its original properties.

Corresponding extracted plasma densities and electron temperatures of CH_4 addition and surface derived hydrocarbon cases are shown in Fig. 4.3. N_e decreases drastically with the addition of CH_4. Electron temperature increases very slightly at high CH_4 additions, due to the depletion of low energy electrons. This effect is similar to the addition of other reactive molecules to Ar plasma,[4.3,4.23] and can be explained by a drop in density due to depletion of electron energy through molecular vibrational processes. Comparatively, surface derived C_xH_y behaves in a very similar way for N_e. At the highest amounts of etching (equivalent to flows of ~1% CH_4), a decrease in N_e

similar to the decrease seen with CH_4 addition is observed. As T_e changes from CH_4 addition in this low regime are minimal, a drop in T_e from surfaces was not expected. T_e seemed to decrease slightly in this regime but changes are within the experimental error of the temperature measurement.

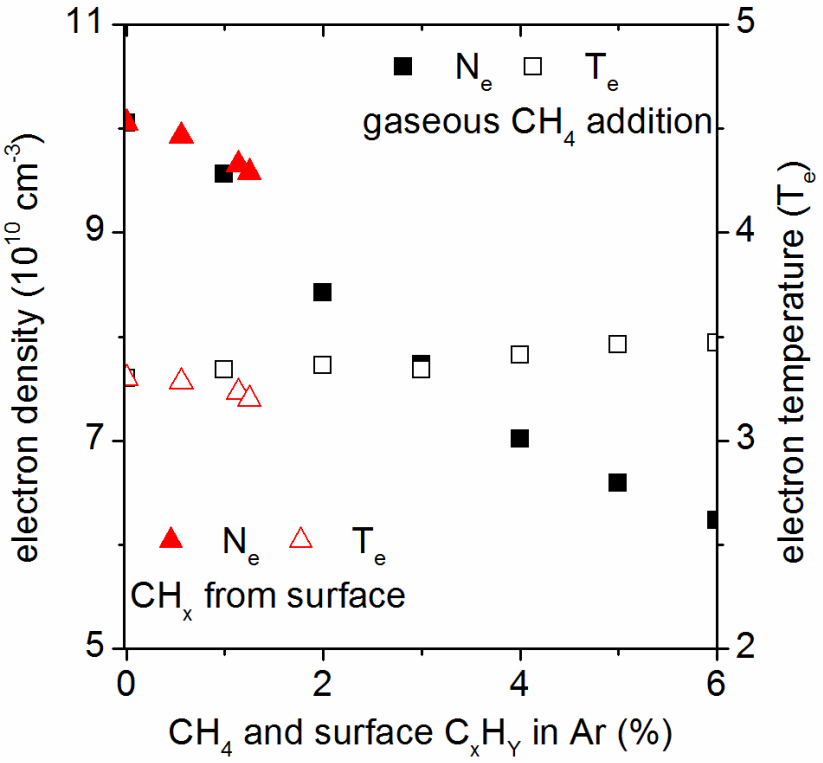

Figure 4.3: *Electron densities and temperatures vs. CH_x flow into the plasma. Black squares show the electron effect of flowing CH_4 on the Ar plasma. Red triangles show the electron effect of erosion of a-C:H effects on the Ar plasma.*

The speed limitations and the gas residence time of the CH_4 cases is showcased here, as it takes longer for the valves to actuate and flow CH_4 (~100's of ms) than for a biased surface to begin etching (~10's of μs). Also, when the flow of CH_4 is turned off, there is a fast response (related to the gas residence time) and a

slower response (related to adsorbed C_xH_y and H_2 coming off the walls). N_e in surface derived carbon cases is also seen to recover from its decrease faster. This is due to the sole location of hydrocarbons within the chamber no longer emitting significant C_xH_y, whereas in CH_4 cases much more chamber surface area is coated with volatile hydrocarbons.

The maximum magnitude of change to N_e by 1% surface/gaseous hydrocarbon emission is ~4% the initial N_e (~1.1 x 10^{11} →~9.6 x 10^{10}). Above 2% addition with gaseous CH_4 flow, the decrease in N_e is greater and linear up to 10% addition, with a decrease of ~8% in N_e per %CH_4 added to the plasma. Though these changes in N_e are significant, for etching/deposition applications, the reactive addition may have large consequences. The etch rate of hydrocarbons can rise with these small additions saturated with H atoms. Similarly to small C_4F_8 additions to Ar plasmas increasing the etch rate of SiO_2 films by F atom reactivity, H atoms drastically increase the etch rate of hydrocarbons.[4.24] Planning plasma processes to have large flows from the substrate and long-term redeposition/etching from plasma-facing surfaces is important for controlling properties and reproducibility, and will become a greater consideration as etching surfaces increase and surface derived impurities constitute significant fluxes into the plasma.

4.5 Conclusions

We conclude that small amounts of hydrocarbon impurities can drastically affect plasma electron behavior. A distinct 4% drop in N_e has been observed when only ~1% flows of hydrocarbons are introduced into the reactor from surface sources. With large surface areas and ion energies, an almost equivalent flow from the surface

compared to gaseous CH_4 flow can be achieved. The drop in N_e of surface hydrocarbon sources compares well with CH_4. Plasma properties quickly react to the addition of hydrocarbon impurities and returns to original properties once gaseous impurities are removed from the chamber. These effects show that impurity flow from surfaces affects plasma properties when high surface areas of reactive materials face the plasma, and introduces time-dependent plasma properties.

Chapter 5: Controlling asymmetric photoresist feature dimensions during plasma-assisted shrink

N. Fox-Lyon, D. Metzler, G.S. Oehrlein

Department of Materials Science and Engineering and Institute for Research in Electronics and Applied Physics, University of Maryland, College Park

D. Farber, T. Lii

Texas Instruments, Dallas

Journal of Vacuum Science and Technology A, in preparation

Abstract

Plasma-assisted shrink (PAS) of features, involving plasma deposition onto sidewalls to shrink features has been described in the past for symmetric features. In this work we explore shrinkage of asymmetric features using fluorocarbon-based plasma deposition. Using top-down and cross-section scanning electron microscopy (SEM), we find the dependencies of this shrink process on top-down blanket deposition thickness, pressure, source power, and deposition plasma chemistry with the aim of achieving the best 1:1 ΔL:ΔW shrink of asymmetric features. In a baseline condition (Ar/20% C_4F_8 plasma, 400 W, 20 mTorr) we find conformal coating from the top to the bottom of a narrow trench and shrinking from ~100 nm to ~50 nm. For strongly asymmetric features, the long dimension (above ~100 nm) sidewall deposition rates scale closely to top-down blanket deposition as neutral arrival is not feature-impeded and growth rate depends only on the sticking/reaction probabilities. In feature dimensions below ~100 nm, sidewall deposition rates decrease rapidly with feature size, as neutral arrival becomes feature-limited as the solid acceptance angle of neutrals and/or low-energy ions is diminished. At higher deposition thicknesses, asymmetric shrink increases, leading to large disparities in ΔL and ΔW. For best 1:1 ΔL:ΔW shrink of features, we find conditions of lower deposition thicknesses, higher pressures, lower powers, and smaller amounts of C_4F_8 fraction to be best.

5.1 Introduction

Recently, plasma-assisted shrink (PAS) has been proposed as a method to shrink sizes of patterned photoresist (PR) features.[5.1–5.3] PAS relies on using polymerizing plasmas to deposit films that cover sidewalls of features after initial patterning. These films could shrink features by 10's of nanometers with sequential deposition/etching cycles. Some success has been reported of shrinking ~100 nm *circular* contact holes and trenches with depositing hydrocarbon and fluorocarbon plasmas up to ~60 nm shrink. [5.1, 5.4–5.7] These processes do not shrink perfectly, and there is some distortion of the pattern that increases with shrink magnitude. While using PAS has been effective for shrinking symmetric circular contact holes, successful PAS of asymmetric contact holes and features has not been reported.

Hydrocarbon- and fluorocarbon-based plasmas have shown some success for PAS and feature sidewall deposition. [5.1, 5.4–5.7] Fluorocarbon-based plasmas are used extensively in etching of dielectric films for device manufacture and deposition of low-k materials.[5.8, 5.9] Fluorocarbon deposition on sidewalls during dielectric and silicon etching is an established method to control feature dimensions.[5.10, 5.11] A FC-based deposition step during the Bosch process (cyclic process to etch high AR features through silicon vias) protects silicon sidewalls by passivation.[5.12, 5.13] The sidewall passivation step and the thickness of the passivation layer has been studied extensively.[5.14] By tuning plasma chemistries, thin fluorocarbon films coat sidewalls and protect silicon from reactive species (atomic fluorine, etc.) during etch. These fluorocarbon-based plasmas could possibly be extended beyond sidewall preservation during etch to PAS processes. Etching applications in asymmetric features and

features with high AR show problems with getting sufficient passivation of sidewalls and available etch reactants at the bottom of features.[5.15, 5.16] This effect, known as RIE lag, results in major difficulties for etching of high-aspect ratio features.[17,18] This work investigates the problem of shrinking asymmetric holes uniformly, the physical limitations of depositing in shadowed features, and which plasma parameters can give the best results.

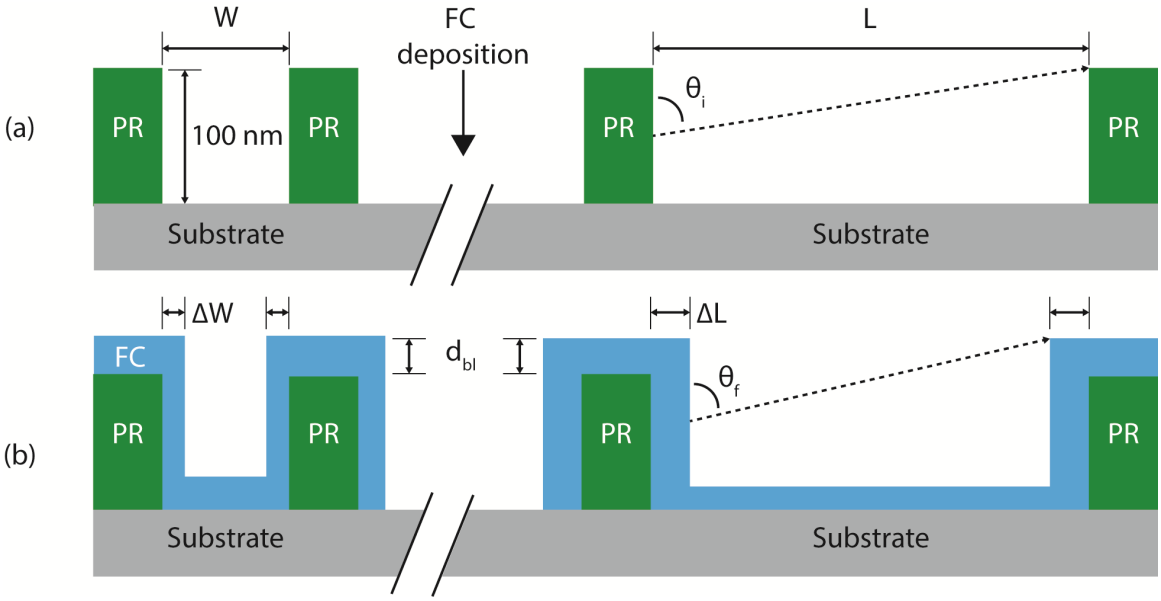

Figure 5.1: *(a) Example cross section views of asymmetric photoresist features on a substrate before FC deposition. (b) Example changes in length (ΔL) and width (ΔW) with deposition of a FC film.*

There is difficulty in equally shrinking features with very short, confined dimensions versus those with longer dimensions, and there is a dependence of shrink on initial critical dimensions. Figure 5.1 shows schematics for an asymmetric feature and introduces terminology used in analysis of this study. Figure 5.1 (a) shows a model of PR features on a substrate from two perspectives (length, L, and width, W) before a fluorocarbon PAS process. The height of the PR film is ~100 nm. Figure 5.1

(b) is an example of an ideal fluorocarbon PAS shrink process with uniform shrink of large and small feature dimensions of varying initial sizes. ΔL is the change in the longer feature dimension, and ΔW is the change in the shorter feature dimension. Top-down blanket deposition (d_{bl}) is the total fluorocarbon film thickness deposited during the shrink process on a monitor blanket wafer. Ideally, PAS would minimize net d_{bl}, ΔL is equal to ΔW, and the sidewalls would be uniformly coated. The polar angle, θ, for the direct acceptance of fluorocarbon plasma species, changes depending on the AR of the feature and its location in the feature.

5.2 Experimental details and methods

An inductively coupled plasma reactor, described in previous publications,[5.19] was used for the PAS process. Briefly, a 13.56 MHz rf power supply with an L-type matching network powers a planar coil above a quartz window. A substrate electrode can be independently biased at 3.7 MHz to control ion energies. The distance between the substrate electrode and the quartz window is 8 cm. PR samples (2.5 cm x 2.5 cm) were thermally attached to the substrate electrode whose temperature was held constant at 10° C. A base pressure of 5×10^{-6} Torr was achieved before all plasma processes. Plasmas for PAS processes were Ar/C_4F_8 mixtures with varying gas composition, source powers, and neutral pressures to tune deposition properties. Labelle *et al.* previously investigated the blanket deposition dependencies (composition, deposition rate, optical index, etc.) of these films while varying plasma properties.[5.20]

193 nm PR blanket films and patterns were used to study deposition rates and shrink by PAS in this study. Patterned films consisted of PR features (~100nm in

initial height) on silicon substrates (pristine features of different AR's are shown in Fig. 2 (a-c)). Deposition rates were monitored by *in situ* ellipsometry of blanket 193 nm PR films during PAS processing to determine end points of plasma processes. We find the index and thickness of top-down deposited fluorocarbon films using a multilayer ellipsometric model accounting for the 193nm PR film index and thickness.[5.20] Scanning electron microscopy (SEM) was used to measure initial feature sizes and the changes to features caused by PAS and cyclic processes. Dimensions of features were measured using Digimizer line-drawing software coupled with the microscope scale. Statistical calculation of line lengths were performed multiple times per feature type.

5.3 Results

As reported previously for fluorocarbon PAS processes,[5.7] the Ar/C_4F_8 plasma deposition drastically changed the dimensions of features. After 60 nm d_{bl} (Fig. 5.2 (d-f)), a buildup on the sidewalls and bottom of the trenches is observed (Fig. 5.2 (d)). Cross sections of the features with fluorocarbon coating shows uniform trench (~100 nm W and >5 µm L, initial) sidewall deposition from the top of the feature to the bottom, and compares well with top-down SEM measurements (Fig 5.2 (e)). A net increase in total film thickness matches closely to that seen in the blanket film. In some initially narrow areas (~65 nm W), complete occlusion of the feature is observed (seen in Fig. 5.2 (f) in the long, narrow feature near the top).

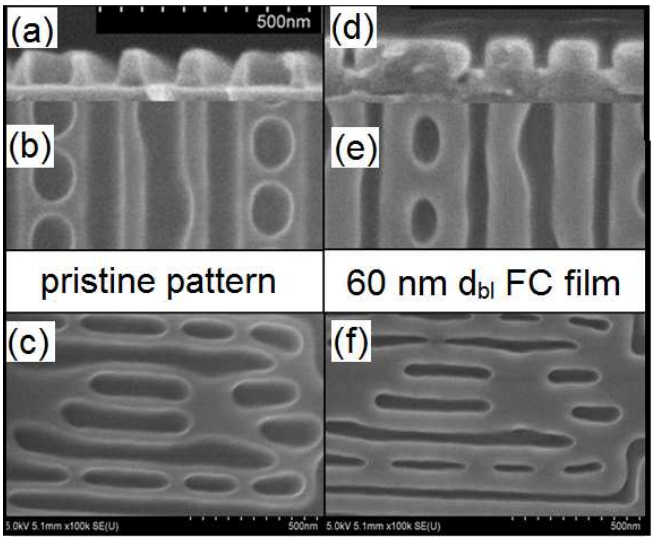

Figure 5.2: *Cross section and top-down SEM micrographs of photoresist features before ((a), (b), and (c)) and after FC deposition ((d), (e), and (f)). (a) and (d) show the cross section of holes and long lines shown from a top-down perspective in (b) and (e). (c) and (f) show features of varying asymmetries.*

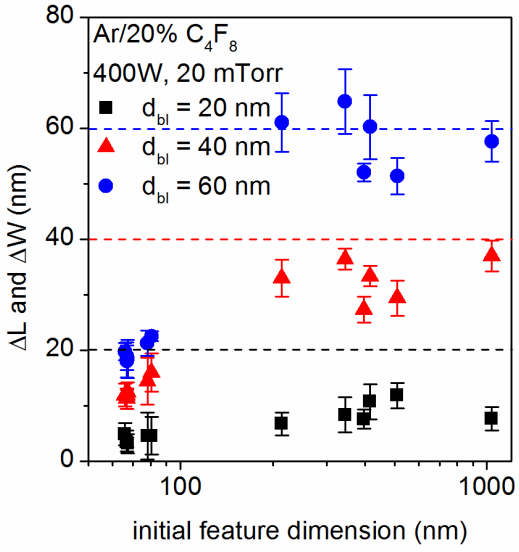

Figure 5.3: *Feature size dependence on change in dimensions (ΔL and ΔW) at different top-down deposition thicknesses for standard condition. The horizontal lines represent corresponding thicknesses of d_{bl}.*

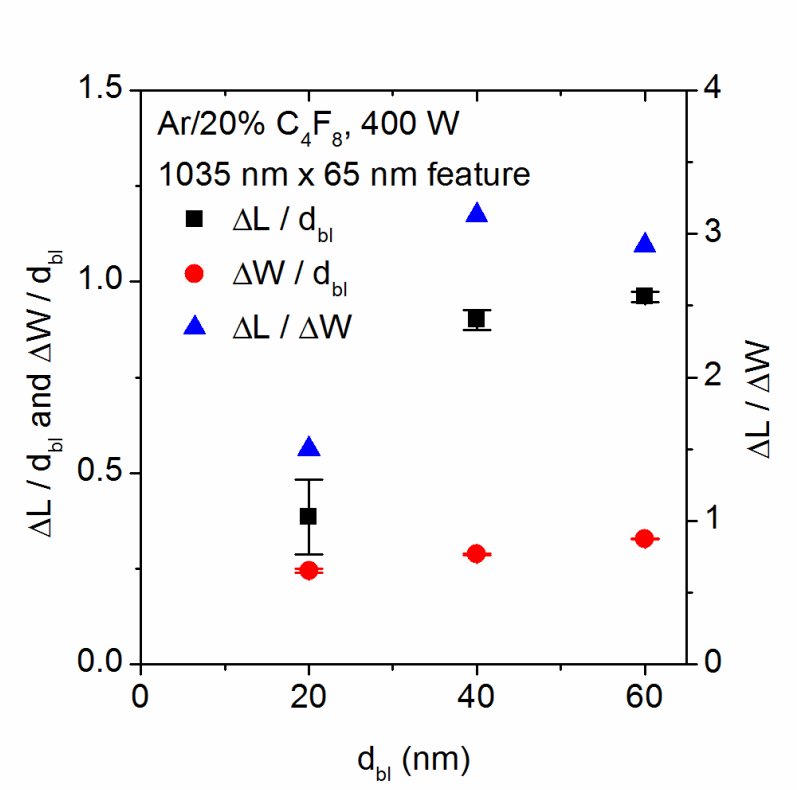

Figure 5.4: *Changes in dimensions (ΔL and ΔW) normalized to d_{bl} and ΔL over ΔW for different deposition thicknesses.*

Changes to feature ΔL and ΔW with different initial dimensions are shown in Fig. 5.3. The fluorocarbon PAS process was carried out for three deposition thicknesses (20 nm, 40 nm, and 60 nm) on the different feature dimensions. As top-down deposition increased from 20 nm to 60 nm, ΔL and ΔW increased. Initially in the 20 nm deposition case, the sidewall deposition rate is slower. Once above 20 nm d_{bl} is deposited, the shrink rate matches well with top-down deposition (40 nm and 60 nm cases). A clear difference in feature shrink rates is seen between larger and smaller features. Larger feature dimensions (L>100 nm) shrink at about twice the top-down deposition thickness for 40 nm and 60 nm top down deposition. The differences for a highly asymmetric feature (1035 nm x 65 nm) are highlighted in Fig.

5.4. At 20 nm d_{bl}, ΔL is close to ΔW. As d_{bl} increases, ΔL increases faster than ΔW for highly asymmetric features. The rate of increase of ΔW with d_{bl}, in contrast to ΔL, does not follow d_{bl} at higher values.

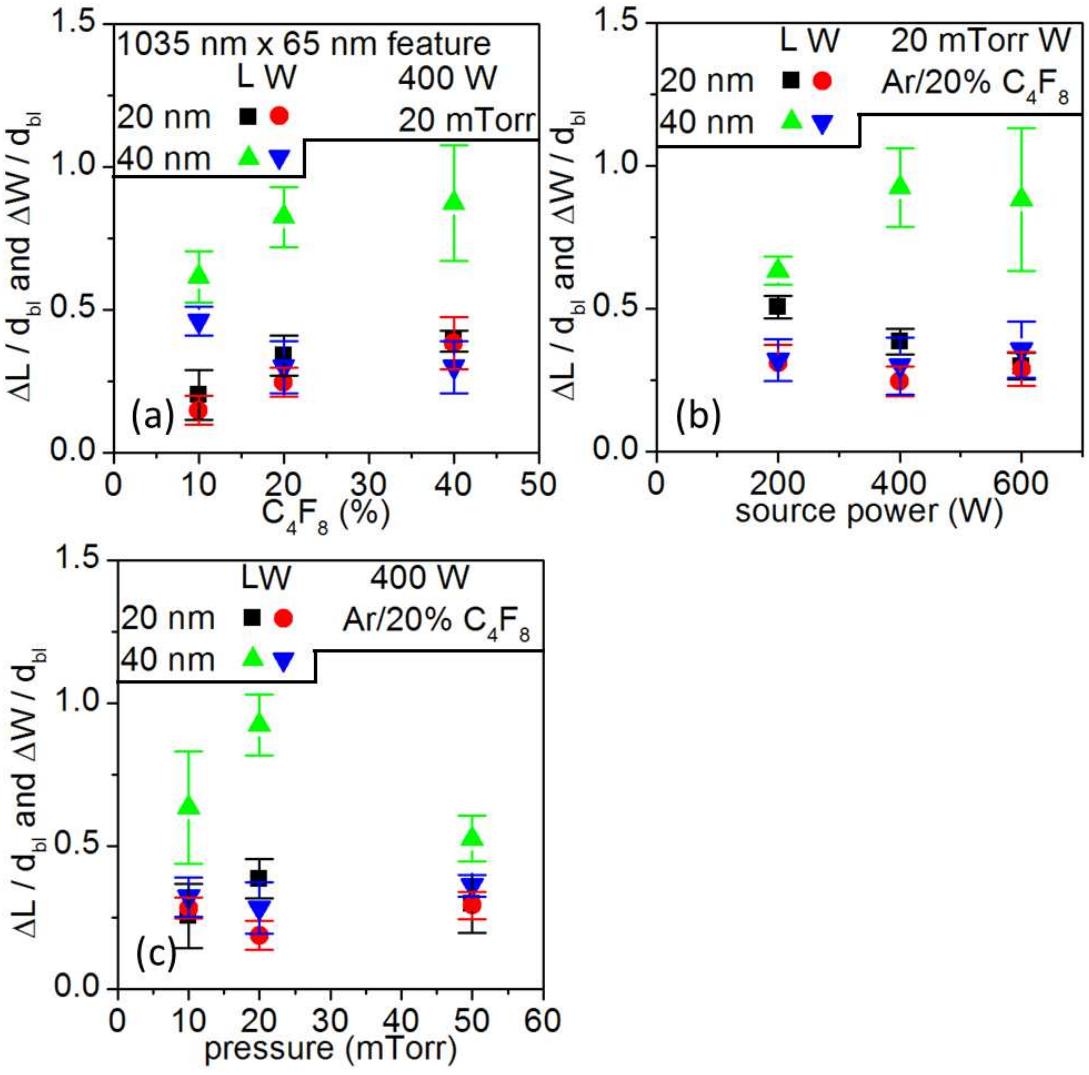

Figure 5.5: *Changes in dimensions (ΔL and ΔW) for d_{bl} 20 nm and 40 nm for different C_4F_8 (a) concentrations, (b) source powers, (c) and pressures.*

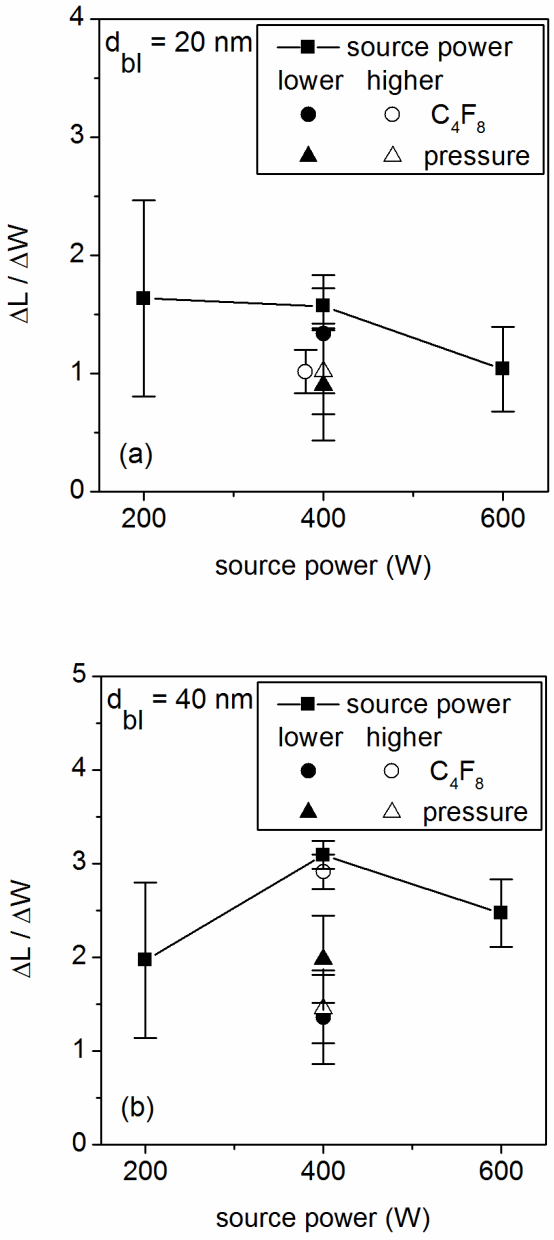

Figure 5.6: *ΔL over ΔW at two different deposition thicknesses, (a) 20 nm d_{bl} and (b) 40 nm d_{bl}, for different deposition parameters. The 400W, 20 mTorr, 20% C_4F_8 case is the baseline which the pressure and chemistry parametric studies are anchored to. To improve clarity between data points the higher C_4F_8 case was offset on the x axis in the d_{bl} = 20 nm case.*

Plasma parametric dependencies for asymmetric feature shrink were also explored. Figure 5.5 shows the effects of plasma fluorocarbon chemistry, chamber pressure, and applied source power on the ΔL and ΔW of highly asymmetric features (1035 nm L x 65 nm W) at different d_{bl}. The total change of ΔL and ΔW is normalized to d_{bl}. An increase in both ΔL and ΔW per d_{bl} is seen with increasing $\%C_4F_8$ in Ar/C_4F_8 plasma (Fig. 5.5 (a)). Increasing source power above 200 W dramatically increases the ΔL per d_{bl} (Fig. 5.5 (b)). An increase in source power at these conditions greatly increases plasma density and dissociation. Figure 5.5 (c) indicates that there is a local peak of ΔL at 20 mTorr when changing the pressure. These results are normalized (ΔL/ΔW) and displayed relative to the baseline condition (400 W, 20 mTorr, 20% C_4F_8 in plasma) in Fig. 5.6.

5.4 Discussion

During plasma etching of oxides with fluorocarbon gases, steady-state fluorocarbon films are formed as intermediates to etching products.[5.21] C_4F_8 molecules in the plasma are dissociated into FC film precursors that deposit onto plasma facing surfaces.[5.22] The composition, etch and deposition rates, and thickness are determined by plasma parameters such as depositing gas chemistry/concentration, plasma density, ion energy, etc.[5.20] Fluorocarbon film deposition is highly dependent on depositing species fluxes, and reactivity of surface sites. The sticking coefficient (s) expresses the reaction probability that an incident fluorocarbon species will deposit onto surfaces. For fluorocarbon films, this probability is increased with ion-induced surface defects/ reactive sites. Low energy ion bombardment can break

bonds, sputter fluorine and create reactive sites for additional bonding and film buildup to occur.[5.23]

There are two regimes of deposition into high aspect ratio features. Blanket films and low AR features are in a surface-reaction limited regime where the deposited film thickness is independent of feature size and the deposition rate depends on S.[17] The deposition rate can be expressed as:

$$DR = \frac{M}{\rho N_A} s J_n \tag{1}$$

where DR is the deposition rate, J_n is the flux of neutrals to the surface and s is the effective sticking coefficient for a depositing neutral, and will reflect factors like synergistic ion bombardment, etc., ρ film density, N_A Avogadro's number, and M the mass per mole.

The neutrals in our deposition plasma have molecular flow characteristics (interaction with the wall/surfaces before interacting with another gaseous neutral). When depositing into geometrically shadowed features, the sticking coefficient remains constant while the flux of species into the film is constrained as they begin to interact with feature sidewalls. PAS shares the issue of deposition into asymmetric features of feature impact on incident particle as has been discussed for aspect-ratio-dependent-etching using fluorocarbon plasmas and plasma-enhanced atomic layer deposition.[5.15,5.17,5.24] The cause of non-uniform deposition and etching in small features has been explained by several processes including ion shadowing/deflection, neutral shadowing, and Knudsen transport of neutrals.[5.15, 5.17] As ions in our deposition plasma have only low energies and are highly directional, the neutral behavior may dominate deposition onto the feature sidewalls. The solid angle of

acceptance on a sidewall changes drastically in small asymmetric features and neutrals may experience shadowing. The polar angle of neutral acceptance, Θ, of the feature will change drastically during shrink. For example, if the feature in Fig. 5.1 (a), had initial L and W dimensions of 300 nm and 100 nm, respectively, the polar angle of acceptance half-way down the feature is

$$\theta = tan^{-1}(AR) \tag{2}$$

where the AR is defined as

$$AR_x = \frac{x}{d_{PR}} \tag{3}$$

where x is the L or W of the feature and d_{PR} is the length from the top of the feature to the angle origin. For this example Θ_L is 80° while Θ_W is 63°. This initial angle changes after deposition of 20 nm fluorocarbon film onto each side of the sidewalls (Fig. 5.1 (b)). The polar angle of acceptance decreases from 80° to 79° and from 63° to 50° for Θ_L and Θ_W, respectively. The effect of neutral shadowing on acceptance angles is readily apparent and gets worse as features shrink during the deposition process. We can expect that as feature sizes are constrained, scattering of low-energy ions will increase and fewer depositing CF_x species will migrate to the bottom of the features.

Beyond shadowing effects, the flow of neutrals in high AR features will behave collisionally with the sidewalls. Coburn and Winters created a conductance model of Knudsen (collisional) transport of species to the bottom of high AR holes, relative to the flux at the top of the hole:[5.25]

$$J_b S_b = J_t - (1-k)J_t - k(1-S_b)J_b \tag{4}$$

Where J_b and J_t are the fluxes to the bottom and top the hole, respectively, S_b is the sticking coefficient at the bottom of the feature, and k is related to the time-dependent aspect ratio.[5.17] The more interactions with sidewalls, the higher the probability of deposition. At high AR, depositing neutrals may not deposit deep into features if interaction lengths become too short. The deposition may be constrained and taper close to the top of the feature.

While we see no evidence of tapering deposition at our conditions, AR effects are seen when depositing into the asymmetric features. We see a sharp transition (~100 nm) when the deposition transitions from a surface-reaction limited regime to a flux limited regime (by intervening feature parts) (Fig. 5.3). At very low depositions, the features all initially grow slower than d_{bl}. Deposition into patterned features has a lag period during which the coating shows only ~1/2 of the d_{bl} amount, with d_{bl} being 20 nm. This could be due to initial surface conditions on patterned features and the resolution/contrast limitations of our SEM images of the polymer due to charging. Above 20 nm d_{bl}, large feature dimensions (100+ nm) shrink in a fashion that follows d_{bl} closely. This is direct evidence for features that are surface-reaction limited; the flux of depositing species is near-identical to those seen by the blanket surface. Features below 100 nm do not change dimensions closely with d_{bl}. A decrease in shrink is seen as feature sizes get smaller. These features fit the criteria for the flux-limited regime. The feature sidewalls are getting much less neutral deposition than the larger features. Changing plasma parameters from this baseline condition can affect the dependence on these relative changes (ΔL:ΔW). Figure 5.6 shows the combined effects of changing parameters at different deposition thicknesses. At 20

nm d_{bl} (Fig. 5.6 (a)), the effects of the change in parameters is obscured by the large error bars and the insensitivity of the SEM images, though we would like to point out that the relative ΔL and ΔW differences are much lower for less deposition. At 40 nm d_{bl},(Fig. 5.6 (b)) effects become clearer.

At higher %C_4F_8 flows there is very little change from the baseline condition in relative ΔL:ΔW. This is evidence that starting with 20% C_4F_8, the process is on the high end of neutral-ion fluxes for this ion energy, leading to favoring deposition in surface-reaction limited feature dimensions. Decreasing %C_4F_8 in plasmas is advantageous for better 1:1 ΔL: ΔW shrink. Deposition in the narrow (< ~100 nm) dimensions is still limited by neutral incidence and the density of depositing species is lower for all surfaces. It is possible that for low %C_4F_8 in Ar ion etching effects reduce growth on ion-exposed surfaces[26] As relative ion bombardment increases in these open areas (due to an increase in ionization at lower %C_4F_8 and a decreased flux of depositing neutrals), film deposition is suppressed, giving comparable deposition rates to short dimension features. The relative shrink for both the 20 nm and 40 nm d_{bl} cases are within 5% of each other.

The effect of source power on the process is shown in Fig. 5.5 (b) and 5.6. As source power is increased from 200 W to 600 W, a larger ΔL per d_{bl} is achieved, while ΔW per d_{bl} remains constant. With increasing source power, the degree of dissociation and available depositing species increases greatly, allowing for more deposition. While the density and energy of ions also increases, the sputter rate without additional ion energy is very low. At higher powers the degree of asymmetric

shrink is amplified, due to a lower amount of sputtering of surface-reaction limited feature dimensions relative to deposition, similar in effect to raising the $\%C_4F_8$ flow.

Chamber pressure had the highest ΔL:ΔW at 20 mTorr. Above and below 20 mTorr, less ΔL and ΔW per d_{bl} was observed, along with lesser differences in ΔL/ΔW. At lower pressures, plasma density drops along with densities of fluorocarbon depositing species. Lower pressure have previously been seen to help control FC species in high AR features when etching SiO_2.[5.17] As changing ion:neutral ratios in features can affect deposition rates, another parameter that will be important for future work to investigate is ion energy. Since substrate electrode was kept floating we did not constrain the ion energy. At lower pressures and higher powers, ion energies can increase dramatically. Applying a bias also controls directionality of ions, allowing for more anisotropic distributions of ions in features.

5.5 Conclusions

Fluorcarbon-based plasmas were investigated with the goal to achieve 1:1 ΔL:ΔW PAS of asymmetric features. We find that fluorocarbon plasmas can shrink trench and hole sidewalls conformally and to a high degree (e.g. 100 nm shrunk to 50 nm in width). We find that diffusion of neutral species into features for deposition is highly AR dependent, similar to problems described in AR dependent etching of silicon using fluorocarbon plasmas. Through tuning plasma properties from our baseline condition, we were able to find conditions where ΔL:ΔW gets closer to 1:1. Minimizing ΔL and ΔW by short depositions (20 nm d_{bl}) conserved the asymmetry due to the flux limitations getting worse at smaller dimensions. Decreasing fluorocarbon gas admixture (from 20% to 10%) improved asymmetric shrink by

decreasing neutral deposition on surface-reaction limited feature dimensions, bringing them closer to flux-limited depositions in small dimension features. Going to higher/lower pressures (10 mTorr and 50 mTorr relative to 20 mTorr, respectively) also helped as plasma properties changed dramatically.

Chapter 6: Isotope effects on plasma species of $Ar/H_2/D_2$ plasmas

N. Fox-Lyon, G.S. Oehrlein

Department of Materials Science and Engineering and Institute for Research in Electronics and Applied Physics, University of Maryland, College Park

Journal of Vacuum Science and Technology B, in preparation

Abstract

We studied the influence of isotopes on the Ar/H_2 and Ar/D_2 plasmas using Langmuir probe and ion mass analyzer measurements at several pressures relevant to low temperature plasma surface processing. As up to 50% H_2 is added to Ar plasma, electron energy distribution functions show a decrease in electron temperature (from 2.5 eV to 3 eV for 30 mTorr with 50% addition) and a decrease in electron density (2.5×10^{11} $cm^{-3} \rightarrow 2.5 \times 10^{10}$ cm^{-3} at 30 mTorr with 50% addition). At lower pressures (5 and 10 mTorr) these effects are not as pronounced. This change in electron properties is very similar for Ar/D_2 plasmas due to similar electron cross-sections for H_2 and D_2. Ion types rapidly transition from predominantly Ar^+ to molecular ions ArH^+/H_3^+ and ArD^+/D_3^+ with the addition of H_2 and D_2 to Ar, respectively. At high pressures and for the heavier isotope addition, this transition to molecular ions is much faster. Higher pressures increase the ion-molecules induced formation of the diatomic and triatomic molecular ions due to a decrease in gaseous mean-free paths. The latter changes are more pronounced for D_2 addition to Ar plasma due to lower wall-loss of ions and an increased reaction rate for ion-molecular interactions as compared to Ar/H_2.

Introduction

Ar/H_2 plasmas are of interest to for control of defect levels during graphene deposition,[6.1,6.2] doping transistors,[6.3] and control of hydrocarbon surface properties.[6.4] Recent works have aimed at characterizing plasma properties and surface interacting species in Ar/H_2 plasmas.[6.4–6.12] At low pressures (1-100 mTorr), major surface interacting species in Ar/H_2 plasmas are ions, reactive H atoms, UV/VUV photons and Ar metastable atoms. Gudmundsson first measured the ion mass and energy distributions for most ion types present (H^+, H_2^+, H_3^+, and Ar^+).[6.5,6.6] Kimura and Kasugai[6.7] and Hjartarsson *et al.*[6.8] then collected electrical/optical data and modeled the complete system using a global model, but without direct quantified ion composition measurements. They found that plasma density decreased rapidly with the introduction of H_2 into the pure Ar plasma. They showed that the ArH^+ ion should make up a significant portion of ions. Sode *et al.* recently measured calibrated ion mass distributions for Ar/H_2 plasmas that accurately described the ion types more completely. One of his reported findings was that the ArH^+ ion is a much more substantial fraction within the plasma. Sode *et al.* also measured dissociation fractions and free H atom density in the Ar/H_2 plasmas.[6.9, 6.10] Wang *et al.*[6.11] and Fox-Lyon *et al.*[6.12] recently reported on the effect of H_2 addition to Ar plasma on Ar metastable atom concentrations using optical methods and probe measurements.

Sode *et al.* described the measurement of all surface relevant ion types with different flows of H_2 in Ar plasma (0-100% H_2 in Ar plasmas, 7.5 mTorr, with a constrained electron density, $N_e = 3 \times 10^{10}$ cm^{-3}).[10] Their work effectively predicted the change in ion composition when only changing the gas fraction of H_2, by

adjusting the N_e through applied rf power modulation. For the purposes of surface processing, we are interested in how the plasma changes with only one parameter changing at a time. We are also interested in how different conditions (such as pressure) affect the density and energy of species within the plasma. At higher pressures, plasma species mean-free paths decrease, leading to more molecule-electron and molecule-ion collisions. As the predominant molecular ions in Ar/H_2 mixtures (ArH^+ and H_3^+) are only formed by ion-molecule collisions, we can expect that ion composition distributions will be drastically different. In this study we explore the effects of chamber pressure has on plasma electron energy distribution functions (EEDF) and ion composition distribution.

Another area of interest is plasma characterization of the low-H_2 flow regime in Ar/H_2 plasmas. When etching hydrocarbons at low pressures, we found that the plasma-surface interactions transitions from a purely physical sputtering regime to a chemical sputtering regime when up to 20% H_2 is added to Ar plasma.[6.4] The etch rate becomes significantly higher and large degrees of surface re-hydrogenation of the H-depleted surface is observed. Even with small hydrogen flows in Ar (~10% H_2 in Ar), the surfaces experienced up to a 3-fold increase in etch rate.[6.4] Kimura and Kasugai predicted a very rapid transition of ion types and electron densities when small amounts of H_2 is added to Ar plasmas.[6.7] Sode *et al.*'s experimental measurements of ion distributions encompasses large spans of H_2 flow, but with minimal information in this transition regime where the predominant ion transitions from Ar^+ to ArH^+.[6.10] Ion mass plays a large role in surface modification and etching of hydrocarbon films. D^+, in place of H^+, has been used to compare ion mass effects

on collisional energy transfer at surfaces.[6.13] There have been no experimental measurements of ion mass distributions and electron behavior with D_2 addition to Ar plasmas in this processing regime. We compare the effect of D_2 flow has on Ar plasma properties and species.

Experimental details and methods

$Ar/H_2/D_2$ plasma characterization and reactive etching of hard hydrocarbons was studied using an inductively coupled plasma reactor. This reactor has been described in previous publications.[14] The plasma is generated by a planar coil above a quartz window with a 13.56 MHz rf power supply with an L-type matching network. Ion energies to the substrate electrode are controlled by independently biasing at 3.7MHz. The plasmas used in this study were carried out at 5-30 mTorr and 300 W applied rf source power. Substrate bias was only used during deposition/etching of hydrocarbon films. Ar/H_2 and Ar/D_2 ion compositions were characterized using a HIDEN quadrupole ion mass spectrometer with a sampling orifice located near the substrate electrode. Ion masses of 1-42 AMU's were scanned and integrated individually to find the total relative composition of species. For purposes of compositional analysis of relative concentrations, ion intensities were normalized to their transmission coefficient (in this AMU range, it is approximately $1/M_{ion}$). High-resolution measurements of EEDF, N_e, and average electron temperature (T_e) were obtained using a Plasma Sensors Langmuir probe .[6.15]

Results and discussion

EEDF's were obtained for Ar/H_2 and Ar/D_2 plasmas at 10 and 30 mTorr at 0%, 25% and 50% H_2 and D_2 admixtures (Fig. 6.1). The electron behavior changes significantly with the addition of reactant species and increases in pressure. With increasing molecular gas flow, the integrated area of the distribution decreases, while increasing pressure causes an increase. The integrated area corresponds to the N_e, displayed in Fig. 6.2(a). The reduction in N_e is more pronounce as pressures increase due to an increase in inelastic electron-molecule collisions. At 30 mTorr, N_e decreased by a factor of almost 10 (~2.5x 10^{11} cm^{-3} → ~2.9 x 10^{10} cm^{-3}) with 50% H_2 or D_2 addition to Ar plasmas. The average value for the distribution corresponds to the T_e displayed in Fig. 6.2(b). With increasing H_2/D_2 flow in Ar plasmas, a slight increase is seen in T_e. Again, this effect is more pronounced at higher pressures, when electron-molecular collisions increase. At 30 mTorr, T_e increased from ~2.5 eV to ~3 eV with H_2/D_2 addition to Ar plasmas. The electron behavior of Ar/H_2 and Ar/D_2 plasmas is very similar, showing little isotope effect on electron properties. The insensitivity to the type of molecular gas was expected, as the electronic excitation and ionization cross-sections of H_2 and D_2 molecules are very similar for low energy electrons.[6.16] Ar metastable atoms are also of interest to materials processing and have large changes have been observed upon introduction of H_2 and other impurity gases into Ar.[6.11,6.12] Ar metastable atom densities are governed by generation (Ar atom densities, N_e, and T_e) and quenching (molecule-metastable atom collisions, wall-metastable atom collisions, and short lifetimes). Using an optical technique reported previously,[6.12] we found that densities of Ar metastable atoms is similar with H_2 and

D_2 addition to Ar plasmas, without large differences. This conclusion makes sense as Ar densities and EEDF's are near-identical for both H_2 and D_2 addition and there is minimal molecule-metastable atom quenching. At low pressures (below ~75 mTorr), mean-free paths between neutrals is much larger than the chamber wall, and lifetimes of Ar metastable atoms are shorter than interaction lengths.[6.17, 6.18]

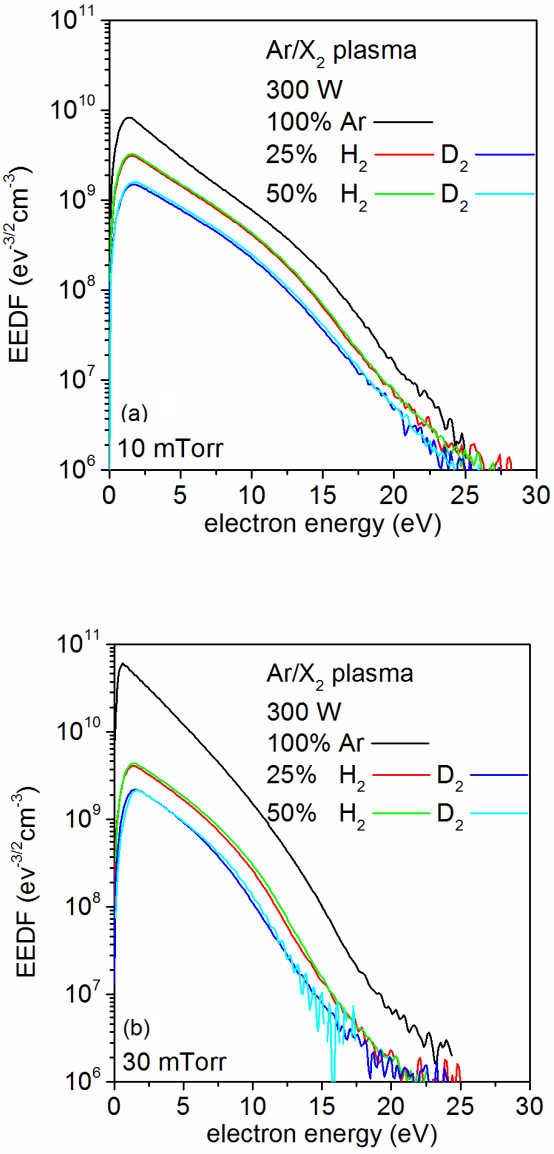

Figure 6.1: *Electron energy distribution functions for Ar/H_2 and Ar/D_2 plasmas at 10 mTorr (a) and 30 mTorr (b).*

Ion composition distribution effects from pressure, $\%H_2$ and $\%D_2$ flow in Ar plasma, and isotope effects is shown in Fig. 6.3. At low pressures (10 mTorr), the relative amounts of Ar^+, H_3^+, H_2^+, and H^+ matches well with data presented by Sode *et al.* at (7.5 mTorr).[6.10] The Ar^+ ion rapidly diminishes with H_2 addition. At higher pressures, the relative prevalence of these light ions switches. H_2^+ and D_2^+ are suppressed at higher pressures due to the interaction with neutral H_2 and D_2 atoms, respectively, to form triatomic ions. The formation of molecular ArH^+ is mainly by Ar^+ collisions with an H_2 molecule.[9] This ion-neutral collision causes dissociation of the H_2 molecule and formation of an ArH^+ ion. At higher pressures, the transition to molecular ions is faster. Similarly to the effect pressure has on electron properties, this if due to an increase in molecular interactions with charged ions in the plasma and neutral molecules. The significantly lower mean-free paths become apparent.

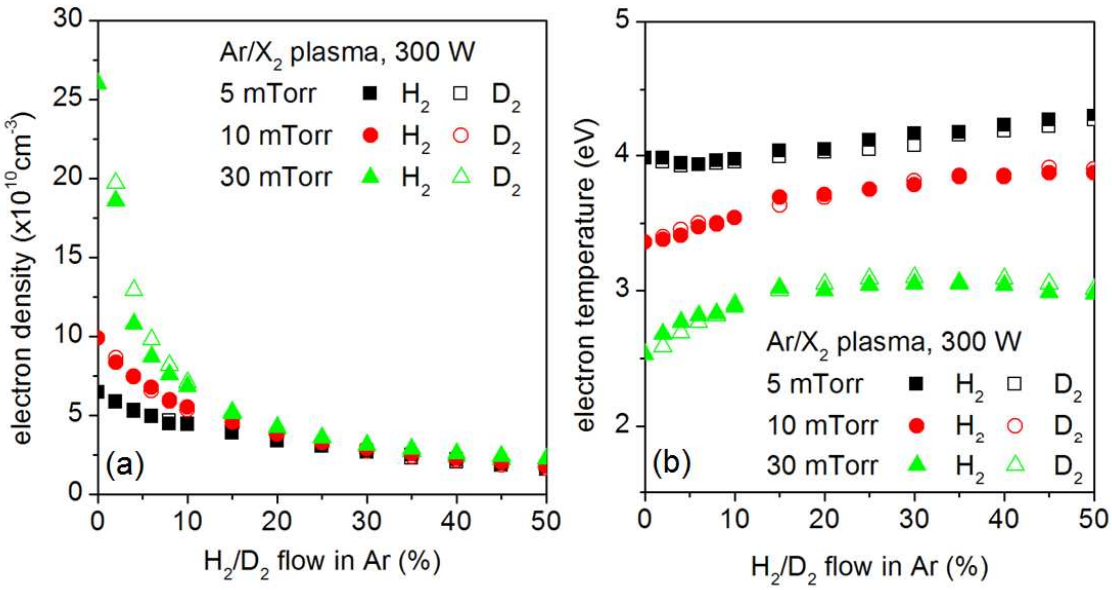

Figure 6.2: (a) *N_e's for Ar/H_2 and Ar/D_2 plasmas at various pressures. (b) T_e's for $Ar/H_2/D_2$ plasmas at various pressures.*

D_2 addition to Ar plasma, relative to H_2 addition, appears to cause a faster transition to higher measured densities of molecular ions. This could be due to its mass-dependent lower loss rate to walls. The transit time is much lower for H containing molecular ions, leading to depletion within the plasma bulk. Another reason for this is that as the predominant molecular ions are only formed by molecule-ion collisions, the larger collisional cross-section of deuterium atoms causes increased. The important ions for hydrocarbon surface interacts are Ar^+, ArH^+, and ArD^+. These ions can impart the most energy into surfaces and effectively sputter C and H. In Fig. 6.4, these ions are displayed for different pressures. The depletion rate of Ar^+ ions and the formation rate of ArH^+ ions and ArD^+ ions increases with pressure. D_2 addition is favored for the formation of molecular ions in each case.

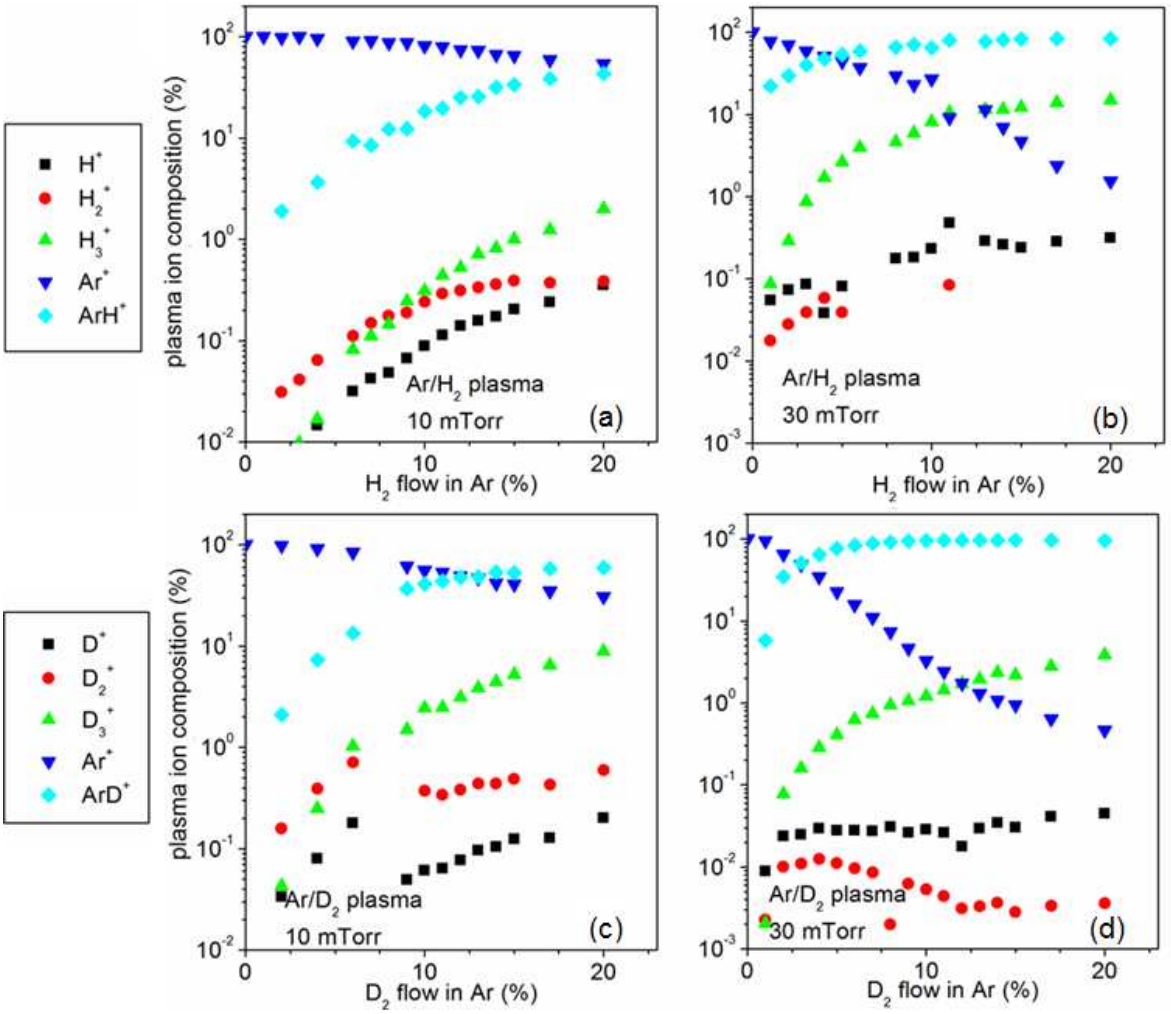

Figure 6.3: *Ion composition distributions for Ar/H_2 and Ar/D_2 plasmas at 10 mTorr and 30 mTorr.*

With these large differences in Ar/H_2 and Ar/D_2 ion composition distributions and molecule-ion interactions, hydrocarbon surfaces can interact differently. Figure 6.5 shows the results of etching a hard hydrocarbon in dilute Ar/H_2 and Ar/D_2 plasmas. The hard a-C:H film etched in this study were grown using a CH_4 plasma with high energy bombardment of the substrate. During deposition, the films were monitored using in-situ ellipsometry to gauge the thickness and optical index of refraction. Hardness of the films was confirmed using Hopf *et al.*'s optical index of

refraction-bulk property (H:C ratio and density) relationship of a-C:H films and the film's properties.[6.19] The substrate was actively cooled with a chiller to 10° C.

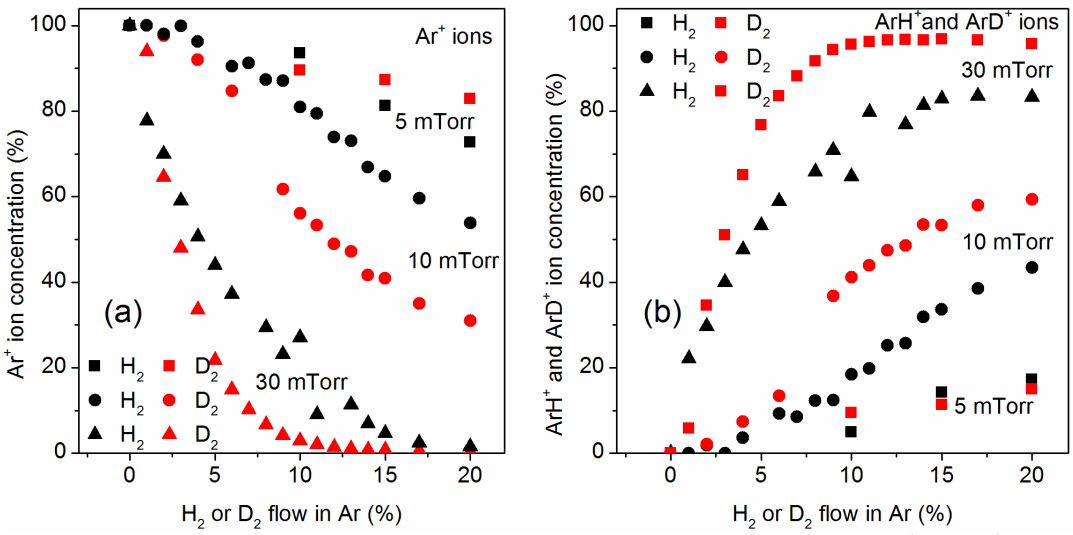

Figure 6.4: *Ion mass differences for major surface-interacting ions (Ar^+, ArH^+ and ArD^+) in $Ar/H_2/D_2$ plasmas at 5 mTorr, 10 mTorr, and 30 mTorr.*

The etch yield for D_2 containing plasmas is much greater than H_2 containing plasmas. This higher rate is possibly due to several causes. Firstly, the higher degrees of dissociation by molecule-ion impacts could lead to higher reactivity at surfaces. This higher reactivity could mean a higher chemical sputtering rate for D_2 cases. Secondly, for all $\%H_2$ and $\%D_2$ conditions, the average ion mass is higher for Ar/D_2 plasmas than Ar/H_2 plasmas. This higher ion mass means a more effective transfer of energy into the a-C:H film, leading to higher etch rates. Thirdly, the molecular ions contain D, which can sputter hydrocarbons at much lower energies due to its higher mass. As molecular ions split their energy relative to their mass, D atoms end up with more kinetic energy from ArD^+ molecular ions than H atoms from ArH^+ molecular ions.

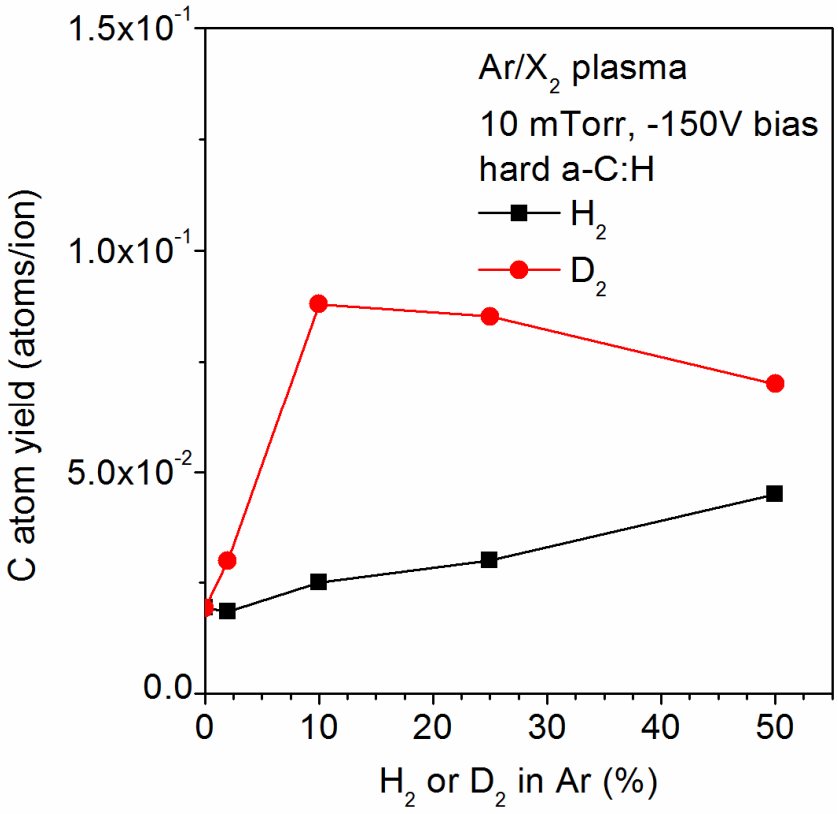

Figure 6.5: *Etch yield differences in Ar/H_2 and Ar/D_2 plasmas.*

Little work exists on the how energy is split when low-energy molecular ions interact with surfaces. For H_3^+/D_3^+ molecular ions, there is evidence that energy is split equally for each atom.[6.20] Harris *et al.* saw a potential molecular size effect of larger molecules advantageously having higher sputtering rates than single atomic ions with normalized energies. Our results could suggest that ArD^+ and ArH^+ and other molecular ions are significantly better at sputtering hydrocarbon films than Ar^+ ions.

Conclusions

We explored the effect chamber pressure and molecular gas isotopes have on Ar/H_2 plasma species. Large decreases in N_e (by ~10x seen for 30 mTorr cases, by ~10x seen for 30 mTorr cases, by ~4x for 10 mTorr cases, and by ~3x for 5 mTorr

cases) were observed with the addition of H_2 and D_2 to Ar plasmas. For EEDF's, N_e, and T_e, D_2 addition to Ar did not significantly differ from H_2 addition. While D_2 molecules have similar electron cross-sections to H_2 molecules, they have slightly larger collisional cross sections. This effect, coupled with the slower loss of D-containing molecular ions at walls, leads to higher amounts of molecular ions in the plasma with D_2 addition than for H_2 addition. For all reactive molecule flows in Ar plasmas, D_2 created a higher percentage of ions relevant to surface interaction with hydrocarbons. the etch yield of hard a-C:H was higher for D_2 addition than H_2 addition due to having more relevant ions, having relatively heavier molecular ions, and more free D atoms for reactivity (due to ion-molecular interactions).

Chapter 7: Graphitic hydrocarbon surface interactions with H_2/D_2 plasmas

N. Fox-Lyon, G.S. Oehrlein

Department of Materials Science and Engineering and Institute for Research in Electronics and Applied Physics, University of Maryland, College Park

Journal of Vacuum Science and Technology B, in preparation

Abstract

Etch rates and modification of hydrocarbons during reactive plasma etching depends on surface composition and the energy and chemistry of incident plasma species. In this study, we explore how plasma-deposited hydrocarbon films with varying hydrogen content and densities interact with hydrogen and deuterium plasmas at different ion energies. The predominant surface interacting species are H_3^+ and D_3^+ and reactive atoms. We observe that films with high %H and low density etch significantly faster than low %H films and high density (48% H vs. 31% H). By normalizing etch rates with hydrocarbon densities to get C atom yields, we observe that there is only minor dependence of C atom removal on the %H content of the a-C:H film. Soft/hard films are modified differently by plasmas with hard films up taking additional carbon at the surface during etching, while soft films losing hydrogen in surface layers. By modulating the energy of incident hydrogen/deuterium ions, the surface behavior (densification or hydrogenation/deuteration) can be controlled during etching. Deuterium causes less surface modification due to significantly higher etch rates (up to 10x higher than H_2, depending on conditions).

Introduction

Reactive plasma surface functionalization and modification of soft hydrocarbon and graphitic materials is an area of interest to biomaterials, device manufacture, and high temperature plasma-material interactions.[7.1–7.4] Hydrogen (H) and other reactive plasma functionalization of graphene/hydrocarbons is an promising avenue for doping and surface modification.[7.5,7.6] In low pressure inductively coupled plasmas, H plasma etching of hydrocarbons is dominated by reactive H atoms and molecular ions (H^+, H_2^+, H_3^+).[7,8] Isotope effects are interesting to investigate not just because of use of deuterium/tritium (D/T) isotopes in fusion plasma, but since it provides information on the impact of bombarding ion mass on behavior and evolution of hydrocarbon surfaces. Large amounts of work have been done investigating H/D plasma species interacting with graphitic hydrocarbons at low pressures and powers.[7.9, 7.10] Hopf *et al.* investigated the effect of H^+ vs. D^+ ion bombardment on hydrocarbon films.[7.10] Due to D's higher mass, kinetic energy transfer to surface atoms/molecules is larger, leading to higher etching yields. Using TRIM.SP[11] models and experimental etching data, they predicted the individual chemical and physical sputtering components to etching hard amorphous hydrocarbons with the isotope ions. Oehrlein *et al.* studied interaction of H and D atoms with hydrocarbon films.[7.12] There is limited information on how the hydrocarbons of varying densities and hydrogen content are etched and modified differently in H/D plasmas. In soft polymers, the effect of reactive atom concentration (O) on the Ar sputter rate can be expressed with the Ohnishi parameter[7.13]:

$$Etch\ Rate \propto \frac{N_T}{N_C - N_O} \tag{7.1}$$

Where N_T is the total number of atoms, N_c is the number of C atoms, and N_o is the number of oxygen atoms. For triatomic polymers:

$$N_C = N_t - N_O - N_H \quad (7.2)$$

Where N_H is the number of H atoms. It is clear that if O and H atom densities decrease, or C-C bonding increases, the etch rate will decrease. This effect has not been heavily explored for situations where density and hydrogen content changes, as seen in amorphous hydrocarbon (a-C:H) films. For polymers with few O atoms (polyethylene), Chaudhury *et al.* did not see an etch rate Ohnishi parameter dependence.[7.14] In the present work, we studied the influence of initial %H in a-C:H films has on etching behavior in H_2/D_2 plasmas. We report the effect ion mass has on the etch rate and surface modification at different ion energies and chemistries.

Experimental details and methods

Plasma characterization and deposition/etching of hydrocarbons was carried out using an inductively coupled plasma reactor, described in previous publications.[7.15] Plasma deposited hydrocarbons can be ideal systems for learning about plasma-surface effects. Amorphous plasma-deposited hydrocarbon (a-C:H) films can have properties ranging from soft (H-rich) to hard (graphitic), depending on plasma deposition conditions.[7.16] Soft a-C:H have a high H:C ratio and have a large percentage of sp^3 bonding (C-H). Conversely, hard a-C:H have little hydrogen incorporation, are very dense, and dominantly graphitic (sp^2) bonding. Polymeric a-C:H films are typically deposited with H-rich hydrocarbon gases at low ion energies and cooled substrates. Graphitic a-C:H films require higher C:H ratio feed gases,

significant ion bombardment (to sputter off H to prevent incorporation), and becomes easier at higher temperatures.

An inductively coupled plasma reactor was used for plasma deposition and H_2/D_2 etching of films. Briefly, a 13.56 MHz rf power supply with an L-type matching network powers a planar coil above a quartz window. Ion energies to the substrate electrode are controlled by independently biasing at 3.7 MHz. The quartz window is located 8 cm over the substrate electrode. H_2/D_2 plasmas were operated at 600 W source power and 30 mTorr chamber pressure. a-C:H films for this study were grown using CH_4 plasma. During deposition, the films were monitored using in-situ ellipsometry to gauge the thickness and optical index of refraction. Hopf *et al.* established a relationship between the optical index of refraction of plasma deposited a-C:H films and the film's properties (H:C ratio, density).[7.16] The plasma deposition was carried out at 10 mTorr and 300 W applied rf source power. The substrate was actively cooled with a chiller to 10° C. To achieve different a-C:H hydrogen contents and densities, the parameter used was the substrate bias. Substrate bias (ion energy) allows for flexible growth of films having hard soft properties with even H saturated feed gases.[7.16] When no substrate bias was applied, and the electrode was floating, the minimal ion bombardment causes a film to be deposited that is ~48% H, and a density ~1 g/cm^3. At the maximum substrate bias investigated in the study (-200 V), films of ~31% H and a density ~1.9 g/cm^3 were obtained.

H_2 and D_2 ion compositions were characterized using a HIDEN quadrupole ion mass spectrometer with a sampling orifice located near the substrate electrode. Ion masses of 1-6 AMU's were scanned and integrated individually to find the total

relative composition of species. For purposes of compositional analysis of relative concentrations, ion intensities were normalized to their transmission coefficient (in this AMU range, it has been show that the coefficient is approximately M_{ion}^{-1}).[7.17,7.18]

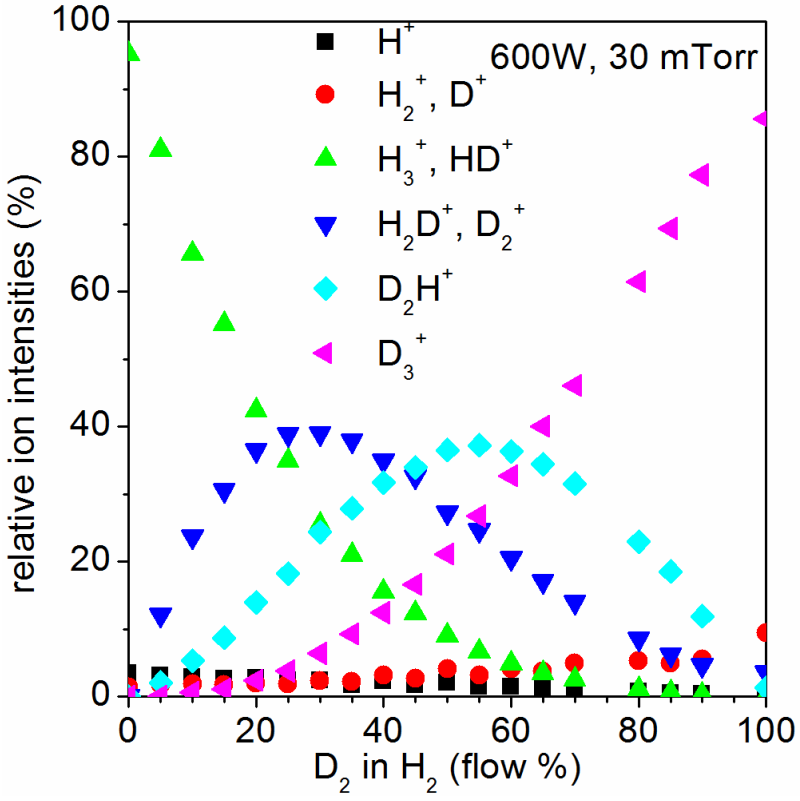

Figure 7.1: *Ion concentrations for H_2/D_2 plasma mixtures with different D_2 impurity flows in H_2 plasma. In mixtures, different ions of masses 2-5 AMU's cannot be distinguished due to mass overlapping, so they are presented as the total sum at each mass.*

Results and discussion

a-C:H surfaces are mainly affected by reactive atoms and ions in the plasma (no effect on surfaces was seen from UV/VUV, when all other species were filtered out by a UV/VUV transparent MgF_2 filter). As molecular dissociation fractions and

free H/D atoms of these plasmas are very similar (with D_2 having a slightly higher dissociation fraction),[7.20] it is seen that differences in ions control surface effects. The predominant ions in both H_2 plasma and D_2 plasma cases are found to be H_3^+ and D_3^+, respectively (shown in Fig. 7.1 at the 0% and 100% D_2 addition to H_2 cases, respectively), with very low amounts of atomic ions and diatomic molecular ions. These results are unlike Gudmudsson's ion distributions with conditions in similar pressures and electron temperatures where a near-equal mixture of triatomic and diatomic molecular ions was seen.[7.7,7.8] Recent works by Sode *et al*. and Kimura *et al.* show that the predominant species should be triatomic ions, consistent with the results in this study. [7.21–7.23] The dominant surface-interacting ions in pure H_2 and D_2 plasmas at these conditions are therefore H_3^+ and D_3^+ ions, respectively. When gas chemistries are changed from pure H_2 to D_2 containing plasma mixtures, the ion species in the plasma change. Figure 7.1. shows the relative ion species as they transition from predominantly H_3^+ ions to D containing ions. Between ~30% and ~60% D_2 flow in H_2 plasma, the predominant ions are molecular ion mixtures of H and D atoms. Between ~30% to 45% D_2, H_2D^+ is the predominant ion, while from ~45% to ~60% the predominant ion is D_2H^+. Above 60% D_2 addition, the predominant ion becomes D_3^+. The earlier transition to D atom dominated ions can be explained by a enrichment in plasmas due to differences in mobility and losses at the wall.[24] Reactions and formation of mixed HD molecules and ions has been heavily studied in fusion and astrophysics topics.[7.25] At low pressures and energies limited work has been done on characterizing expected ions in mixed plasmas. Our measurements are in good agreement with theoretical predictions and experimental

work on H_2/D_2 mixtures in plasmas at low temperatures.[7.24] The average ion mass (Fig. 7.2) during the transition from H_2 to D_2 plasmas is seen to increase linearly, as the relative amounts of triatomic, diatomic, and atomic ions changes very little.

Substrate bias potentials (V_{SB}) can be directly related to the ion energies experienced by the etching hydrocarbons. The applied substrate bias plus the plasma potential (~15V, at these conditions) account for the high energy peak position of the ion energy distribution. For atomic ions, the effective ion energy experienced at the surface is this value. At high energies, molecular ions (of uniform atomic type/weight) at surfaces behave as individual atomic ions with energies divided between each ion.[7.26] At low energies explored in this study, molecular ions have been found to behave slightly differently. At a-C:H surfaces, Krstric *et al.* modeled how molecular H and D ions dissociate near surfaces (due to charge neutralization be electron capture) and split energies among each atom.[7.27] Experimentally through ion beam studies, it was shown that energy normalized molecular ions of H and D atoms have slightly higher etch yields than respective atomic ions, signifying that the energy distribution is not even or other effects are occurring.[7.28, 7.29]

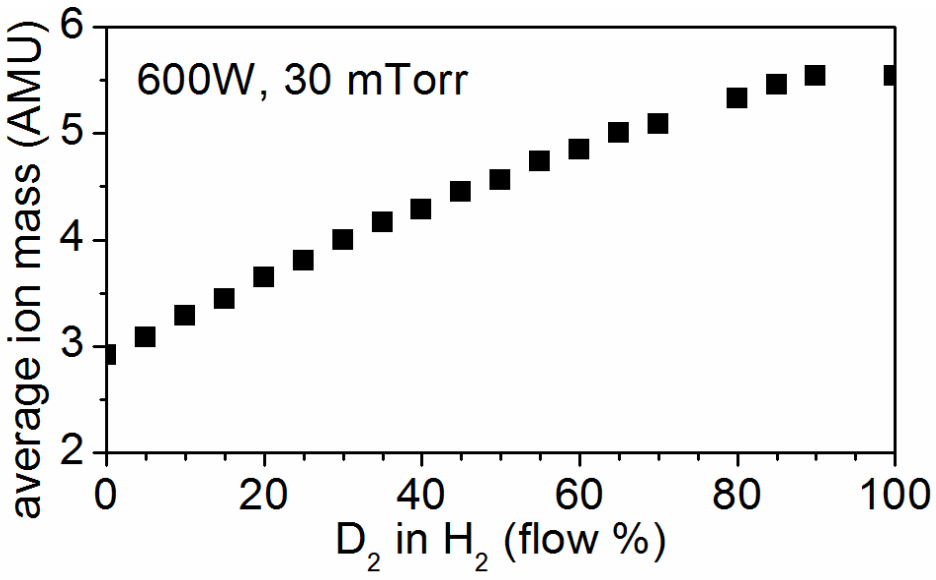

Figure 7.2: *Average ion masses in H_2/D_2 plasmas with different D_2 impurity concentrations. These values were obtained by averaging the total ion flux by the average weight of the ions for various $\%D_2$ flow conditions.*

Hydrocarbon surfaces interacting with H_2 and D_2 plasmas etched at significantly different rates. Figure 6.3 shows the etching of various hydrocarbons with H_2 and D_2 plasmas with bias voltages ranging from -50V to -200V. For all types of film and substrate bias potentials, D_2 plasmas had higher etch rates. The transition from chemical sputtering to physical sputtering regime, as described by TRIM simulation for hard a-C:H films by Hopf *et al.*[10], is evidenced by the differences in low energy etching rates of D_2 and H_2 plasmas (Fig. 7.3 (a,b)). At low energies (below ~35 eV, or 100 V with molecular ion energy splitting normalization), the difference between D_2 and H_2 plasmas etching hydrocarbons is very large. As noted by Hopf *et al.*[10], D ions can effectively etch below 15 eV, while H ions cannot. With normalization of ion energies, i.e. (plasma potential $+V_{SB}$)/3, the energies each ion fragment contributes is ~20 eV at -50V V_{SB}. This energy is insufficient to achieve

sputtering with H ions. Above ~-100V V_{SB}, the etch rates closely reflect the mass differences in the ions. Starting from lower %H in the initial hydrocarbon film, the differences are not as large because of a decreased amount of chemical sputtering, due to limitations in available H atoms to create volatile products at the surface. For both H_2 and D_2 plasmas soft H-saturated a-C:H etched faster than the hard, graphitic a-C:H. The etch rates (seen clearly in the spacing of the D_2 plasma data) increased as %H in the initial film surface increased. At moderate to high biases, the 48% H film ER is only a factor of ~2 to 3 higher for H_2 and D_2 plasmas, respectively. The biggest jump in ER effect is seen in the 35-42% range for both H_2 and D_2 plasmas. The differences in the etching behavior of the hydrocarbons are due to the surface interacting species and the initial film composition and density.

Surface modification of hydrocarbons is also seen to be drastically effected by initial film properties, ion energy, etch rate (as seen in Fig. 7.4).We previously investigated this effect on hard a-C:H for Ar, H_2 and Ar/H_2 plasmas.[7.17] Using a 2-layer ellipsometric model for a modified layer on an a-C:H film, we can find the etch rates of the a-C:H film and an approximate degree of surface modification. As there are two unknowns in this model, the depth of modification must be determined to find the index of refraction of the surface layer. This was obtained using 90% ion-atom displacement event depths (d_{mod}) from TRIM.SP code for films of various density and ions of various energies. For more information about the TRIM.SP code, surface binding energies and other parameters for a-C:H films we refer to Hopf *et al.'s* work.[10] We obtained the index of modified layers feeding these depths into a model for the analysis of the real-time ellipsometric data for the hydrocarbon film etching.

Described in Eq. 7.2., the difference of this index from the underlying film (Δ_n) is multiplied with d_{mod} to get an relative optical density, ρ_{mod}.

$$\rho_{mod} = d_{mod} * \Delta_n \quad (7.2)$$

At low initial %H (31%) and V_{sb}, the modification to the surface is highest and there is a decrease in optical density. This is due to the high degree of hydrogenation required before etching takes place (as discussed earlier for this regime's suppressed yield).

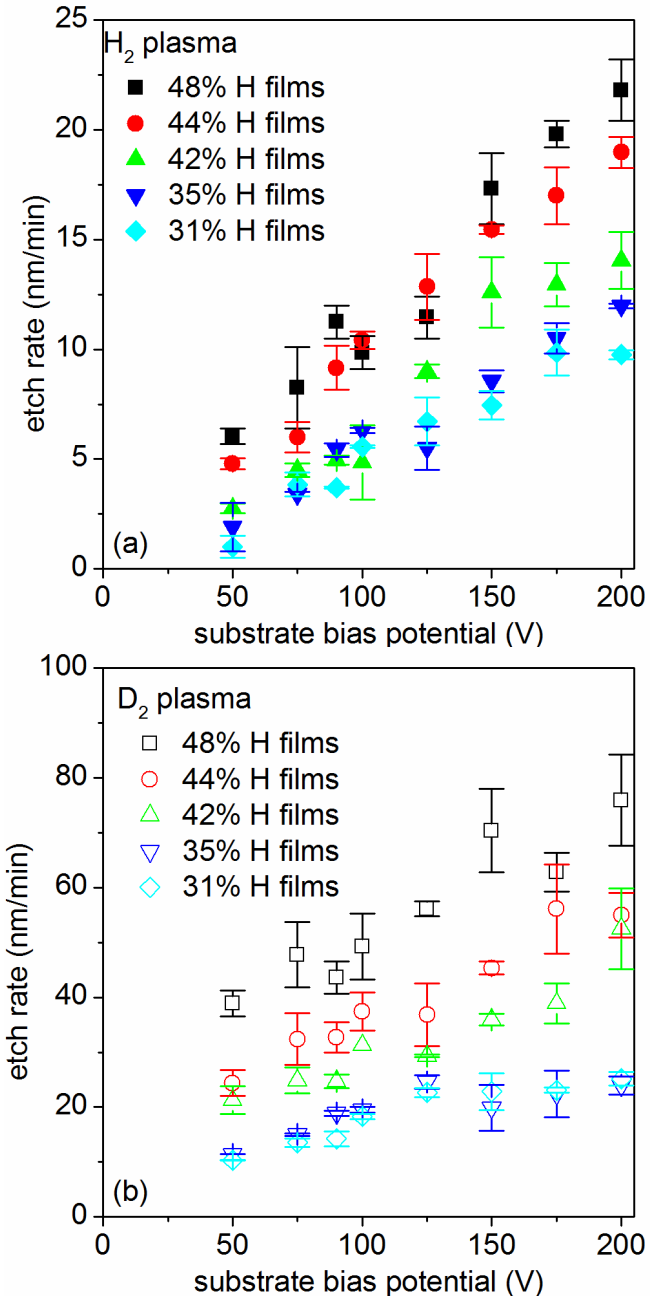

Figure 7.3: *Etch rates for various hydrocarbons (graphitic → soft) in (a) H_2 (closed symbols) and (b) D_2 plasmas (open symbols) from -50V substrate bias to -200V substrate bias in 10-25V increments.*

When the initial film has the highest %H (48%), the optical index is increased as the film is saturated with H before etching, leading to depletion of H in surface

layers during steady-state etching. Moller *et al.* showed that hydrogen/deuterium bombardment causes H atoms in soft a-C:H to selectively sputter and diffuse out as H_2 molecules, which leads to the net increase in optical density.[7.30] In intermediate %H films, the degree of modification decreases as the film composition is closer to a composition advantageous to etching. At 35% H it is observed that the optical index switches from lower to higher optical density in the modified layer when substrate bias (above -75V) is increased. The increasing importance of physical sputtering actually decreases the required H in the surface layer for etching, leading to a depletion of H in the film. We previously reported a similar switch effect of surface density when etching hard hydrocarbons while varying the plasma chemistry in Ar/H_2 plasmas.[17] D_2 plasma is seen to suppress the effects of loss of hydrogen in the soft a-C:H films. The high etch rate (4-8 times higher than H_2 in 48% H films) prevents the formation of highly modified layers. In 31% H films D_2 causes slightly less loss in density as, again, higher etch rates disrupt the formation of H/D rich layers. von Keudell *et al.* showed this effect for soft/graphitic films being etched in H_2 plasmas.[31] Interestingly, we observe that when modulating the bias through critical physical sputtering thresholds, a switching from higher to lower surface density than the initial moderately hydrogenated film can be obtained. This switching can be controlled finely in real-time until the thickness of the film has been fully etched back to the substrate. This effect could be used to tailor the type of surface modification a film undergoes during etching.

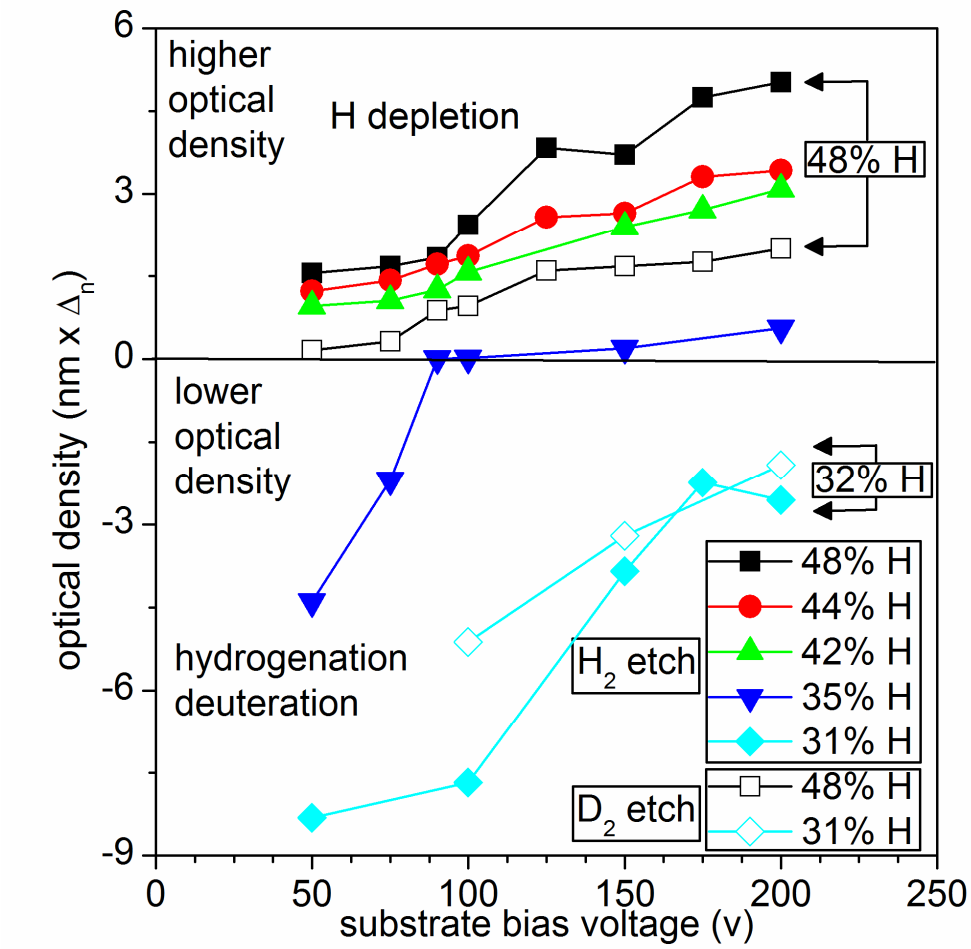

Figure 7.4: *Modified layer optical density (thickness of modified layer by TRIM.SP DP90 and index derived from ellipsometric data) of hydrocarbons of different %H contents etched by H_2 plasmas at various V_{SB} (-50V to -200V). Above zero, a net increase in optical density in the modified layer on was observed (decrease in %H and an increase in density). Below zero, a net decrease in optical density in the modified layer was observed (increase in %H and a decrease in density). Closed symbols represent H_2 plasma etching, while open symbols represent D_2 plasma etching.*

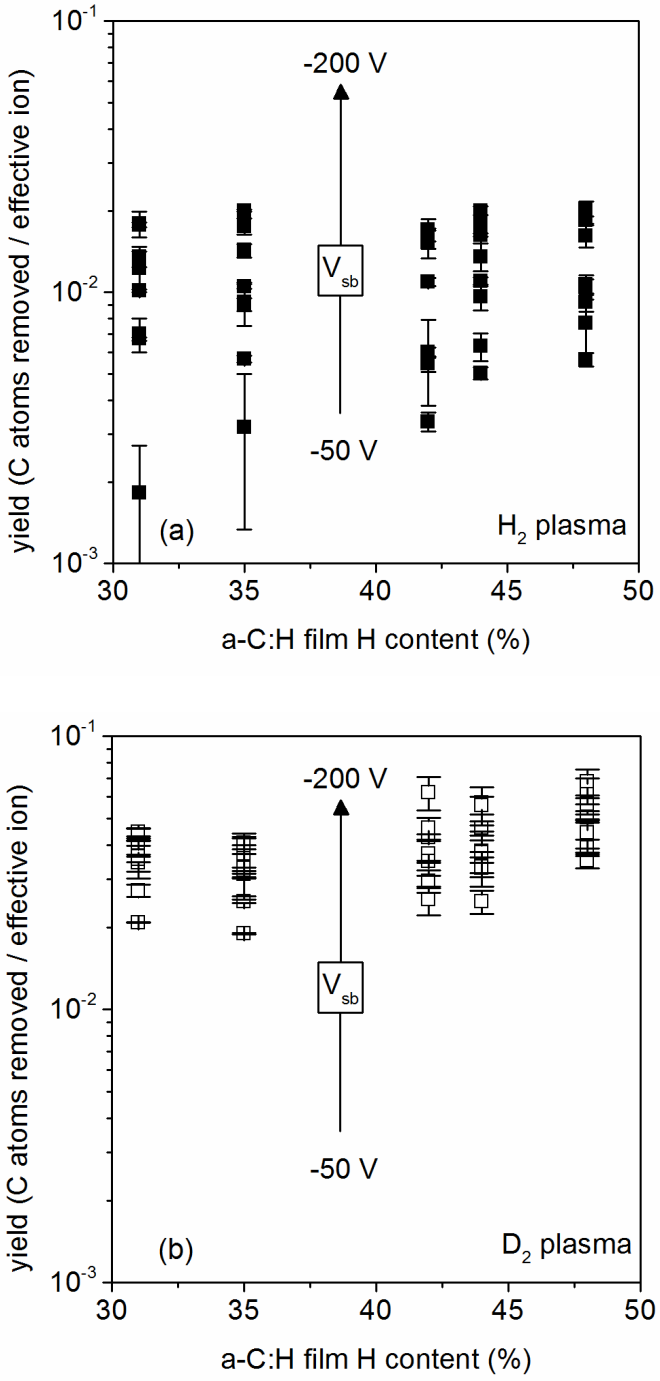

Figure. 7.5: *Yield of hydrocarbons with different %H contents in H_2 (a) and D_2 (b) plasmas at various V_{SB} (-50V to -200V).*

The modification and etch rates of the various films in H_2 and D_2 plasmas should be related to the initial film's physical properties. For photoresists, the Ohnishi parameter describes an etch rate effect for increasing oxygen in polymers. At higher O densities, the etch rate of the film increases proportionally (Eq. 7.1).[7.13] C-O species are easily volatilized by incident ions, whereas less O-saturated C atoms sputter at a much lower rate. It is important to note that all polymers fitting with the Ohnishi parameter are of very similar density and contain significant oxygen densities.[7.14] If we consider a-C:H films in using the Ohnishi model, where N_T consists solely of N_C and N_H, and N_H is substituted for N_O, we can predict the expected etch rate differences. Assuming the N_T in this case is equal to 100, 31% H a-C:H films would have an Ohnishi parameter of $(69\text{-}31)^{-1}$, or about 0.026 while 48% H a-C:H films would have an Ohnishi parameter of $(52\text{-}48)^{-1}$, or about 0.25. These differences (here ~10x in predicted ER difference) are far off from actual etch rate differences (~2-4x difference). Unaccounted for in the Ohnishi model for soft polymers, film density can play a large role in etching films. At higher densities, penetration and ion-atom displacement event depths decrease dramatically. Normalizing for bulk densities of the films (~1.9 g/cm^3 for 31% H films down to ~1 g/cm^3 for 48% H film), C atom yields (C atoms removed per incident ion), and molecular ion energy splitting effects (treating each ion as 3, due to molecular ion splitting effects described above), we plot the etch rate data as C atom yields vs. film %H content in Figure 7.5 (a,b). The etching difference effects seen before with different %H content initial films is much reduced. For our data, the etch yield of an a-C:H film, $Y_{a\text{-}C:H}$, can be expressed for most a-C:H film etching situations as:

$$Y_{a-C:H} \propto \frac{V_{sb}\, m_i}{\rho_{a-C:H}} \tag{7.3}$$

where $\rho_{a\text{-}C:H}$ is the initial film density, and m_i is a factor accounting for the average ion mass. In H_2 plasmas, the yields agree well with this observation, except in the lowest V_{sb} and low %H cases. This is due to an inability to chemically sputter the film effectively due because of limited reactive H atom diffusion and insufficient ion energies. We previously described this slow etching behavior at low potentials for H_2 etching of hard a-C:H.[32] D_2 also shows a significantly lower etch yield regime at smaller a-C:H %H films (31% H and 35% H) that persists for all V_{sb}. For these hard a-C:H films, yields have good agreement with results reported in beam studies.[7.10] This could be due to the limitations of available H/D atoms to saturate bonds at higher etch rates. Without the formation of sufficient volatile CH_4 products, chemical sputtering is at sub critical levels.

Conclusions

In this work we explored the effects of etching different hydrocarbons in H_2/D_2 plasmas. We find that having a higher initial %H content a-C:H leads to higher etch rates that do not follow Ohnishi parameter dependencies. These etch rate differences are due mainly to differences in a-C:H film densities. The yield for hard (31% and 35% H) a-C:H in H_2 plasmas is at low biases is smaller due to insufficient free H atoms to create volatile etch products and limited physical sputtering and chemical sputtering. Ions in D_2 plasmas (predominantly D_3^+) can impart more kinetic energy into the film, lowering the threshold ion energy required for chemical and physical sputtering. This effect is magnified when etching at low substrate biases, as D_3^+ is effectively imparting enough energy for chemical and physical sputtering while

H_3^+ ions cannot. Different kinds of modification can take place as etch rates increase and incorporation of H_2 into films decreases. Modification can be H-depleting or H/D-incorporating at the film surface at some energies and initial film properties. By starting with intermediate density and %H films active switching from densification to hydrogenation was observed.

Chapter 8: Conclusions and Future work

The main goal of this PhD thesis was to increase understanding of fundamental plasma-surface interactions between inert/reactive plasmas and hydrocarbon films during etching conditions to increase the level of control over plasma kinetics and evolving surfaces. This knowledge and control of plasmas and surfaces is valuable for applications in device manufacture, the high temperature/ion flux first-wall in fusion chambers, and other areas. We investigated the evolution of hydrocarbon surfaces by plasma exposure and the change in plasma properties with the addition of reactive species.

In Chapter 2, we investigated the fundamental effects of reactive and inert plasmas on hard amorphous hydrocarbon (a-C:H) films. Through experiments and molecular dynamics (MD) simulation we looked at the mechanisms governing ions and reactive atoms interaction with hydrocarbon surfaces. In inert Ar plasmas, the main surface interacting species, Ar^+ ions, cause densification and loss of hydrogen that scales with ion energy. H_2 plasmas cause rapid population of the near-surface region with H atoms, leading to large decrease in surface density and higher etch rates. With higher ion energies the hydrogenated layer was decreased, as the degree of hydrogenation in the surface required for effective sputtering was suppressed.

Using these insights, we also explored the effects of mixed plasmas on hydrocarbons. With inert/reactive Ar/H_2 plasma mixtures, the surface properties were controllable by changing the plasma chemistry and ion energies. Reversible effects of plasma modification were found, and were revisited in Chapters 6 and 7.

In Chapter 3, the effect of reactive hydrogen addition and changes to pressure have on Ar metastable atoms was investigated. Ar metastable atoms are important surface-interacting ions and are important energy carriers in the plasma. Using multiple concurrent plasma diagnostics and models for excited electron states, we find the changes to Ar metastable atom densities. Increases in pressure cause an initial increase in Ar metastable atom density, as electron density increases strongly with pressure. As pressure continues to rise, electron temperature falls leading to a slower metastable atom formation rate. H_2 addition to Ar plasmas causes a rapid loss in electron density as molecular processes quenched plasma electrons. These results showed an application of a new method for detecting changes to notoriously hard to characterize Ar metastable species. Further effects caused by H_2 addition to plasmas, such as ion mass distributions and surface effects were described in Chapter 7.

In Chapter 4, we studied how the addition of hydrocarbon species into the plasma (from both gaseous and surface derived sources) affects inert Ar plasma properties. As industrial etch processes are in contact with a high surface area of hydrocarbon films, quantification of the feed-back effects on the plasma properties is important. By etching plasma-deposited hydrocarbon materials concurrently with surface characterization, we calculated the effective gaseous hydrocarbon flow into the plasma. We found that both types of hydrocarbon addition cause large decreases in electron density. By etching large areas of hydrocarbons into the plasma, we found that surface-derived CH_x rivals the impact of the equivalent CH_4 from a gaseous source.

In Chapter 5, we provide the first in-depth look at the plasma properties that govern the conformal fluorocarbon deposition into high aspect ratio, asymmetric features for plasma-assisted shrink. Plasma assisted shrink is a plasma deposition process that ideally conformally coats patterned features with polymeric film and shrinks the critical dimensions. Limited academic work exists on this subject and the parametric dependencies and limitations were not well understood. We find that we can create highly conformal fluorocarbon layers on sidewalls of photoresist features using Ar/C_4F_8 plasmas. We find that lower deposition thicknesses, lower plasma densities, higher pressures, and lower amounts of C_4F_8 in the plasma are advantageous to more uniform deposition in asymmetric features. These parameters control the diffusivity and deposition characteristics of depositing neutral and ion species in the photoresist features. Within our parameter space, we find the best amount of shrink to retain feature dimensions to be limited to ~20 nm (in 65nm wide features) or less.

In Chapter 6, we investigated the effect of isotope has on reactive plasma properties and plasma-surface properties of various hydrocarbon films. D_2 plasma, relative to H_2, has higher ion masses, but the same triatomic ion is predominant. D_2 is much more effective at etching hydrocarbons, specifically very H-deficient ($\leq$ 35 % H) hydrocarbon films. D containing ions can effectively cause more sputtering of hydrocarbon species. We saw that modification of film surfaces depended on initial film composition, ion energy, and ion mass. In soft hydrocarbon films, depletion of H atoms was seen with ion bombardment. In hard hydrocarbon films, the films were seen to swell with hydrogenation/deuteration before etching. On this same line of

thought regarding isotope impurities/plasma mixtures, in Chapter 7 we compared the effects that isotope impurities have on inert plasma properties. We found that both impurities in Ar plasmas caused near-identical electron effects, due to very small amounts of electron-molecule interaction at these pressures. Conversely, there are noticeable amounts of ion-molecule interactions at these pressure which cause the formation of molecular ions (H_3^+, ArH^+, D_3^+, ArD^+). In low impurity flows, D_2 molecules cause a faster transition from atomic to molecular ions, due to their larger (vs. H_2) molecular interaction cross section.

Overall, this work showcases the drastic differences a surface can experience with minute changes to plasma conditions. We found that there are dramatic changes to surfaces undergoing plasma. Going the next steps, we need to continue to investigate dilute reactant addition to plasmas, the effects unintended flows have on plasma properties, and unconventional plasma processes for feature and surface control. Applying new knowledge about surface control to real-world situations, such as photoresist processing, could improve current and future generation etch technology.

References

Chapter 1

1.1 S. Samukawa, M. Hori, S. Rauf, K. Tachibana, P. Bruggeman, G. Kroesen, J.C. Whitehead, A.B. Murphy, A.F. Gutsol, S. Starikovskaia, U. Kortshagen, J.-P. Boeuf, T.J. Sommerer, M.J. Kushner, U. Czarnetzki, and N. Mason, J. Phys. D. Appl. Phys. **45**, 253001 (2012).

1.2 G.N. Taylor and T.M. Wolf, Polym. Eng. Sci. **20**, 1087 (1980).

1.3 M. Engelhardt, Contrib. to Plasma Phys. **39**, 473 (1999).

1.4 K. Suzuki, A. Sawabe, H. Yasuda, and T. Inuzuka, Appl. Phys. Lett. **50**, 728 (1987).

1.5 E.M. Liston, L. Martinu, and M.R. Wertheimer, J. Adhes. Sci. Technol. **7**, 1091 (1993).

1.6 G.S. Oehrlein, R.J. Phaneuf, and D.B. Graves, J. Vac. Sci. Technol. B Microelectron. Nanom. Struct. **29**, 010801 (2011).

1.7 H. Winters and J. Coburn, Surf. Sci. Rep. (1992).

1.8 H. Bolt, V. Barabash, W. Krauss, J. Linke, R. Neu, S. Suzuki, and N. Yoshida, J. Nucl. Mater. **329-333**, 66 (2004).

1.9 D. Nest, T.-Y. Chung, D.B. Graves, S. Engelmann, R.L. Bruce, F. Weilnboeck, G.S. Oehrlein, D. Wang, C. Andes, and E. a. Hudson, Plasma Process. Polym. **6**, 649 (2009).

1.10 S. Engelmann, R.L. Bruce, T. Kwon, R. Phaneuf, G.S. Oehrlein, Y.C. Bae, C. Andes, D. Graves, D. Nest, E. a. Hudson, P. Lazzeri, E. Iacob, and M. Anderle, J. Vac. Sci. Technol. B Microelectron. Nanom. Struct. **25**, 1353 (2007).

1.11 A. R. Pal, R.L. Bruce, F. Weilnboeck, S. Engelmann, T. Lin, M.-S. Kuo, R. Phaneuf, and G.S. Oehrlein, J. Appl. Phys. **105**, 013311 (2009).

1.12 S. Engelmann, R.L. Bruce, F. Weilnboeck, G.S. Oehrlein, D. Nest, D.B. Graves, C. Andes, and E. a. Hudson, Plasma Process. Polym. **6**, 484 (2009).

1.13 F. Weilnboeck, R.L. Bruce, S. Engelmann, G.S. Oehrlein, D. Nest, T.-Y. Chung, D. Graves, M. Li, D. Wang, C. Andes, and E. a. Hudson, J. Vac. Sci. Technol. B Microelectron. Nanom. Struct. **28**, 993 (2010).

1.14 C. Hopf, a. Von Keudell, and W. Jacob, Nucl. Fusion **42**, L27 (2002).

1.15 J.T. Gudmundsson, T. Kimura, and M.A. Lieberman, Plasma Sources Sci. Technol. **8**, 22 (1999).

1.16 J.T Gudmundsson, Plasma Sources Sci. Technol. (1999).

1.17 J.T Gudmundsson, Plasma Sources Sci. Technol. **7**, 330 (1998).

1.18 T. Kimura and H. Kasugai, J. Appl. Phys. **107**, 083308 (2010).

1.19 T. Kimura and H. Kasugai, J. Appl. Phys. **108**, 033305 (2010).

1.20 M. Sode, T. Schwarz-Selinger, and W. Jacob, J. Appl. Phys. **113**, 093304 (2013).

1.21 M. Sode, T. Schwarz-Selinger, and W. Jacob, J. Appl. Phys. **114**, 063302 (2013).

1.22 N. Fox-Lyon, A.J. Knoll, J. Franek, V. Demidov, V. Godyak, M. Koepke, and G.S. Oehrlein, J. Phys. D. Appl. Phys. **46**, 485202 (2013).

1.23 S. Wang, A.E. Wendt, J.B. Boffard, C.C. Lin, S. Radovanov, and H. Persing, J. Vac. Sci. Technol. A Vacuum, Surfaces, Film. **31**, 021303 (2013).

1.24 X. Hua, X. Wang, D. Fuentevilla, G.S. Oehrlein, F.G. Celii, and K.H.R. Kirmse, J. Vac. Sci. Technol. A Vacuum, Surfaces, Film. **21**, 1708 (2003).

1.25 T. Schwarz-Selinger, A. von Keudell, and W. Jacob, J. Appl. Phys. **86**, 3988 (1999).

1.26 C.B. Labelle, V.M. Donnelly, G.R. Bogart, R.L. Opila, and A. Kornblit, J. Vac. Sci. Technol. A Vacuum, Surfaces, Film. **22**, 2500 (2004).

1.27 Plasma Sensors, Inc. www.plasmasensors.com

1.28 H. Tompkins and E. Irene, *Handbook of Ellipsometry* (2005).

Chapter 2

2.1 T. Lee, N.-K. Min, H. W. Lee, J. Jang, D. Lee, M. Hong and K.-H. Kwon, Thin Solid Films **517** (14), 3999-4002 (2009).

2.2 H. Dimigen, H. Hübsch and R. Memming, Applied Physics Letters **50** (16), 1056-1058 (1987).

2.3 F. M. Kustas, M. S. Misra, D. F. Shepard and J. F. Froechtenigt, Surface and Coatings Technology **48** (2), 113-119 (1991).

2.4 N. Boutroy, Y. Pernel, J. M. Rius, F. Auger, H. J. v. Bardeleben, J. L. Cantin, F. Abel, A. Zeinert, C. Casiraghi, A. C. Ferrari and J. Robertson, Diamond and Related Materials **15** (4-8), 921-927 (2006).

2.5 W. J. Ma, A. J. Ruys, R. S. Mason, P. J. Martin, A. Bendavid, Z. Liu, M. Ionescu and H. Zreiqat, Biomaterials **28** (9), 1620-1628 (2007).

2.6 W. Jacob and W. Möller, Applied Physics Letters **63** (13), 1771-1773 (1993).

2.7 T. Schwarz-Selinger, A. von Keudell and W. Jacob, Journal of Applied Physics **86** (7), 3988-3996 (1999).

2.8 K. Kanasugi, Y. Ohgoe, K. K. Hirakuri and Y. Fukui, Journal of Applied Physics **105** (9), 094702-094705 (2009).

2.9 J. J. Végh, D. Nest, D. B. Graves, R. Bruce, S. Engelmann, T. Kwon, R. J. Phaneuf, G. S. Oehrlein, B. K. Long and C. G. Willson, Journal of Applied Physics **104**, 034308 (2008).

2.10 R. L. Bruce, F. Weilnboeck, T. Lin, R. J. Phaneuf, G. S. Oehrlein, B. K. Long, C. G. Willson, J. J. Végh, D. Nest and D. B. Graves, Journal of Applied Physics **107** (8), 084310-084315 (2010).

2.11 R. L. Bruce, S. Engelmann, T. Lin, T. Kwon, R. J. Phaneuf, G. S. Oehrlein, B. K. Long, C. G. Willson, J. J. Végh, D. Nest, D. B. Graves and A. Alizadeh, Journal of Vacuum Science & Technology B: Microelectronics and Nanometer Structures **27** (3), 1142-1155 (2009).

2.12 C. Hopf, A. von Keudell and W. Jacob, Journal of Applied Physics **94** (4), 2373-2380 (2003).

2.13 G. S. Oehrlein, T. Schwarz-Selinger, K. Schmid, M. Schlüter and W. Jacob, Journal of Applied Physics **108** (4), 043307-043313 (2010).

2.14 C. Hopf, A. von Keudell and W. Jacob, Nuclear Fusion **42** (12), L27 (2002).

2.15 D. Boutard, B. M. U. Scherzer and W. Möller, Journal of Applied Physics **65** (10), 3833-3837 (1989).

2.16 W. Jacob and J. Roth, in *"Chemical Sputtering" In Sputtering by Particle Bombardment, Experiments and Computer Calculations from Threshold to MeV Energies* (Springer, Berlin, 2007), pp. 329-400.

2.17 W. Jacob, C. Hopf and M. Schlüter, Physica Scripta **2006** (T124), 32 (2006).

2.18 C. Hopf and W. Jacob, Journal of Nuclear Materials **342** (1-3), 141-147 (2005).

2.19 M. Schlüter, C. Hopf and W. Jacob, New Journal of Physics **10** (5), 053037 (2008).

2.20 A. von Keudell and W. Jacob, Journal of Applied Physics **79**, 1092-1098 (1996).

2.21 A. von Keudell, W. Jacob and W. Fukarek, Journal of Applied Physics **66**, 1322-1324 (1995).

2.22 X. Hua, X. Wang, D. Fuentevilla, G. S. Oehrlein, F. G. Celii and K. H. R. Kirmse, Journal of Vacuum Science & Technology A: Vacuum, Surfaces, and Films **21** (5), 1708-1716 (2003).

2.23 T. Y. Leung, W. F. Man, P. K. Lim, W. C. Chan, F. Gaspari and S. Zukotynski, Journal of Non-Crystalline Solids **254** (1-3), 156-160 (1999).

2.24 J. T. Gudmundsson, Plasma Sources Science and Technology **8** (1), 58 (1999).

2.25 T. Kimura, H. Kasugai. Journal of Applied Physics **107**, 083308 (2010)

2.26 H.G. Tompkins, (Wiley, New York, 1999).

2.27 C. A. Davis, Thin Solid Films **226** (1), 30-34 (1993).

2.28 F. Weilnboeck, N. Fox-Lyon, G. S. Oehrlein and R. P. Doerner, Nuclear Fusion **50** (2), 025027 (2010).

2.29 C. Hopf, A. v. Keudell and W. Jacob, Journal of Applied Physics **93**, 3352-3358 (2003).

2.30 D. W. Brenner O. A. Shenderova, J. A. Harrison, S. J. Stuart, B. Ni and S. B. Sinnott, Journal of Physics: Condensed Matter **14** (4), 783 (2002).

2.31 D. B. Graves and P. Brault, Journal of Physics D: Applied Physics **42** (19), 194011 (2009).

2.32 B. Jariwala, C. Ciobanu. S. Agarwal, Journal of Applied Physics **106**, 073305 (2009).

2.33 D. Humbird and D. B. Graves, Plasma Sources Science and Technology **11** (3A), A191 (2002).

2.34 R. L. Bruce, S. Engelmann, T. Lin, T. Kwon, R. J. Phaneuf, G. S. Oehrlein, B. K. Long, C. G. Willson, J. J. Végh, D. Nest, D. B. Graves and A. Alizadeh, Journal of Vacuum Science & Technology B: Microelectronics and Nanometer Structures **27**, 1142-1155 (2009).

2.35 J. F. Ziegler, J. Biersack and U. Littmark, *The Stopping and Range of Ions in Matter* Pergamon Press, New York, (1985)

2.36 A. von Keudell and W. Jacob, Journal of Applied Physics **79**, 1092-1098 (1996).

2.37 W. Jacob, C. Hopf and M. Schlüter, Applied Physics Letters **86** (20), 204103-204102 (2005).

2.38 P. S. Krstic, C. O. Reinhold and S. J. Stuart, Europhysics Letters **77** (3), 33002 (2007).

2.39 L. I. Vergara, F. W. Meyer, H. F. Krause, P. Träskelin, K. Nordlund and E. Salonen, Journal of Nuclear Materials **357** (1-3), 9-18 (2006).

2.40 P.R. Harris, F.W. Meyer, W. Jacob, T. Schwarz-Selinger, U von Toussaint, Nuclear Instruments and Methods in Physics Research B 269 (2011).

2.41 H. Zhang, F.W. Meyer, H.M. Meyer III, M.J. Lance, Vacuum **82** (2008)

2.42 M. Schlüter, C. Hopf and W. Jacob, New Journal of Physics **10** (5), 053037 (2008).

2.43 P. N. Maya, U. von Toussaint and C. Hopf, New Journal of Physics **10** (2), 023002 (2008).

Chapter 3

3.1 V. S. Voitsenya, D. I. Naidenkova, Y. Kubota, S. Masuzaki, A. Sagara, and A. K Yamazaki, National Institute of Fusion Science **799** (2004)

3.2 N. Fox-Lyon, G. S. Oehrlein, N. Ning, and D. B. Graves, Journal of Applied Physics **110** (2011)

3.3 C. F. Yeh, T. J. Chen, C. Liu, J .T. Gudmundsson, and M. A. Lieberman, Ieee Electron Device Letters **20,** 223-225 (1999)

3.4 T. Kimura and H. Kasugai, Journal of Applied Physics **107** (2010)

3.5 A. T. Hjartarson, E. G. Thorsteinsson, and J. T. Gudmundsson, Plasma Sources Science & Technology **19** (2010)

3.6 M. Sode, T. Schwarz-Selinger, and W. Jacob, Journal of Applied Physics **113** (2013)

3.7 D. Leonhardt, J. C. R. Eddy, V. A. Shamamian, R. F. Fernsler, and J. E. Butler, Journal of Applied Physics **83,** 2971-2979 (1998)

3.8 G. R. Scheller, R. A. Gottscho, T. Intrator, and D. B. Graves, Journal of Applied Physics **64,** 4384-4397 (1988)

3.9 G. A. Hebner and P. A. Miller, Journal of Applied Physics **87,** 8304-8315 (2000)

3.10 S. B. Hill, C. A. Haich, F. B. Dunning, G. K. Walters, J. J. McClelland, R. J. Celotta, and H. G. Craighead, Applied Physics Letters **74,** 2239-2241 (1999)

3.11 M. L. Chabinyc, J. C. Love, J. H. Thywissen, F. Cervelli, M. G. Prentiss, and G. M. Whitesides, Langmuir **19,** 2201-2205 (2003)

3.12 G. A. Hebner, Journal of Applied Physics **80**, 2624 (1996)

3.13 M. Schulze, A. Yanguas-Gil, A. von Keudell, P. Awakowicz, *Journal of Physics D: Applied Physics* **41,** 065206 (2008)

3.14 J. B. Boffard, R. O. Jung C. C. Lin, A. E. Wendt, *Plasma Sources Science & Technology* **18,** 035017 (2009)

3.15 Z. Gavare, D. Gött, A. V. Pipa, J. Röpcke, A. Skudra, *Plasma Sources Science and Technology* **15,** 391 (2006)

3.16 J. B. Boffard, R. O. Jung, C. C. Lin, L. E. Aneskavich, A. E. Wendt, *Journal of Physics D: Applied Physics* **45,** 045201 (2012)

3.17 S. Wang, A. E. Wendt, J. B. Boffard, C. C. Lin, S Radovanov, H Persing, Journal of Vacuum Science & Technology A **31**, 021303 (2013)

3.18 C. A. DeJoseph and V. I. Demidov, Journal of Physics B-Atomic Molecular and Optical Physics **38,** 3805-3814 (2005)

3.19 C. A. DeJoseph, V. I. Demidov, and A. A. Kudryavtsev, Physical Review E **72,** 036410 (2005)

3.20 V. I. Demidov, C. A. DeJoseph, and A. A. Kudryavtsev, Physical Review Letters **95**, 215002 (2005)

3.21 R. O. Jung, J. B. Boffard, L. W. Anderson, and C. C. Lin, Physical Review A **75** (2007)

3.22 S. F. Adams, E. A. Bogdanov, V. I. Demidov, M. E. Koepke, A. A. Kudryavtsev, and J. M. Williamson, Physics of Plasmas **19**, 023510 (2012)

3.23 X. F. Hua, X. Wang, D. Fuentevilla, G. S. Oehrlein, F. G. Celii, and K. H. R. Kirmse, Journal of Vacuum Science & Technology A **21,** 1708-1716 (2003)

3.24 VGPS probe system, www.plasmasensors.com

3.25 V. Godyak and V. Demidov, Journal of Physics D: Applied Physics **44,** 233001 (2011)

3.26 V. A. Godyak, R B Piejak, and B M Alexandrovich, Plasma Sources Science & Technology **11,** 525-543 (2002)

3.27 J. T. Gudmundsson, Plasma Sources Science & Technology **7,** 330-336 (1998)

Chapter 4

4.1 S. Wang, A.E. Wendt, J.B. Boffard, C.C. Lin, S. Radovanov, and H. Persing, J. Vac. Sci. Technol. A Vacuum, Surfaces, Film. **31**, 021303 (2013).

4.2 T. Kimura and H. Kasugai, J. Appl. Phys. **108**, 033305 (2010).

4.3 T. Kimura and H. Kasugai, J. Appl. Phys. **107**, 083308 (2010).

4.4 N. Fox-Lyon, A.J. Knoll, J. Franek, V. Demidov, V. Godyak, M. Koepke, and G.S. Oehrlein, J. Phys. D. Appl. Phys. **46**, 485202 (2013).

4.5 S.J. Ullal, A.R. Godfrey, E. Edelberg, L. Braly, V. Vahedi, and E.S. Aydil, J. Vac. Sci. Technol. A Vacuum, Surfaces, Film. **20**, 43 (2002).

4.6 S. Xu, Z. Sun, X. Qian, J. Holland, and D. Podlesnik, J. Vac. Sci. Technol. B Microelectron. Nanom. Struct. **19**, 166 (2001).

4.7 G. Cunge, N. Sadeghi, and R. Ramos, J. Appl. Phys. **102**, 093304 (2007).

4.8 K. Wong, D.S. Boning, H.H. Sawin, S.W. Butler, and E.M. Sachs, J. Vac. Sci. Technol. A Vacuum, Surfaces, Film. **15**, 1403 (1997).

4.9 I.P. Herman, Annu. Rev. Phys. Chem. **54**, 277 (2003).

4.10 M. a. Sobolewski and D.L. Lahr, J. Vac. Sci. Technol. A Vacuum, Surfaces, Film. **30**, 051303 (2012).

4.11 D. Zhou, T.G. Mccauley, L.C. Qin, A.R. Krauss, and D.M. Gruen, **83**, 98 (1998).

4.12 S. Hong, J. Berndt, and J. Winter, Plasma Sources Sci. Technol. **12**, 46 (2003).

4.13 S. Samukawa, M. Hori, S. Rauf, K. Tachibana, P. Bruggeman, G. Kroesen, J.C. Whitehead, A.B. Murphy, A.F. Gutsol, S. Starikovskaia, U. Kortshagen, J.-P.

Boeuf, T.J. Sommerer, M.J. Kushner, U. Czarnetzki, and N. Mason, J. Phys. D. Appl. Phys. **45**, 253001 (2012).

4.14 V.M. Donnelly and A. Kornblit, J. Vac. Sci. Technol. A Vacuum, Surfaces, Film. **31**, 050825 (2013).

4.15 G. Cunge, N. Sadeghi, and R. Ramos, J. Appl. Phys. **102**, 093305 (2007).

4.16 R. Ramos, G. Cunge, and O. Joubert, J. Vac. Sci. Technol. A Vacuum, Surfaces, Film. **25**, 290 (2007).

4.17 X. Hua, X. Wang, D. Fuentevilla, G.S. Oehrlein, F.G. Celii, and K.H.R. Kirmse, J. Vac. Sci. Technol. A Vacuum, Surfaces, Film. **21**, 1708 (2003).

4.18 VGPS Probe System, www.plasmasensors.com.

4.19 N. Fox-Lyon, G.S. Oehrlein, N. Ning, and D.B. Graves, J. Appl. Phys. **110**, 104314 (2011).

4.20 T. Schwarz-Selinger, a. von Keudell, and W. Jacob, J. Appl. Phys. **86**, 3988 (1999).

4.21 V. Godyak, R.B. Piejak, and B.M. Alexandrovich, Plasma Sources Sci. Technol. **1**, 36 (1992).

4.22 M. Sode, T. Schwarz-Selinger, and W. Jacob, J. Appl. Phys. **114**, 063302 (2013).

4.23 A.T. Hjartarson, E.G. Thorsteinsson, and J.T. Gudmundsson, Plasma Sources Sci. Technol. **19**, 065008 (2010).

4.24 C. Hopf, a. Von Keudell, and W. Jacob, Nucl. Fusion **42**, L27 (2002).

Chapter 5

5.1 M. Op de Beeck, J. Versluijs, Z. Tőkei, S. Demuynck, J.-F. De Marneffe, W. Boullart, S. Vanhaelemeersch, H. Zhu, P. Cirigliano, E. Pavel, R. Sadjadi, and J. Kim, Proc. SPIE **6519**, 65190U (2007).

5.2 M. Nagase, T. Maruyama, and M. Sekine, IEEE Trans. Semicond. Manuf. **20**, 245 (2007).

5.3 Y. Yamada, M.M. Crouse, S. Dunn, T. Kawasaki, S. Shimura, E. Nishimura, Y. Tanaka, J. Galloway, B. Pierson, and R. Routh, in *SPIE Proc.* , *Opt. Microlithogr. XXI*, p. 69242D–69242D–11 (2008).

5.4 J. Versluijs, J.-F. De Marneffe, D. Goossens, M. Op de Beeck, T. Vandeweyer, V. Wiaux, H. Struyf, M. Maenhoudt, M. Brouri, J. Vertommen, J.S. Kim, H. Zhu, and R. Sadjadi, Proc. SPIE **6924**, 69242C (2008).

5.5 S. Demuynck, Z. Tokei, C. Zhao, J.F. de Marneffe, H. Struyf, W. Boullart, M.O. de Beeck, L. Carbonell, N. Heylen, J. Vaes, G.P. Beyer, S. Vanhaelemeersch, R. Sadjadi, H. Zhu, P. Cirigliano, J.S. Kim, J. Vertommen,

B. Coenegrachts, E. Pavel, and A. Athayde, in *2007 Int. Symp. Semicond. Manuf.* (IEEE, 2007), pp. 1–4.

5.6 J.-F. De Marneffe, F. Lazzarino, D. Goossens, A. Vandervorst, O. Richard, D. Shamiryan, K. Xu, V. Truffert, and W. Boullart, Jpn. J. Appl. Phys. **50**, 08JE07 (2011).

5.7 M.-C. Liang, H.-Y. Tsai, C.-C. Chung, C.-C. Hsueh, H. Chung, and C.-Y. Lu, IEEE Electron Device Lett. **24**, 562 (2003).

5.8 M.R. Baklanov, J.-F. de Marneffe, D. Shamiryan, A.M. Urbanowicz, H. Shi, T. V. Rakhimova, H. Huang, and P.S. Ho, J. Appl. Phys. **113**, 041101 (2013).

5.9 K. Endo, K. Shinoda, and T. Tatsumi, J. Appl. Phys. **86**, 2739 (1999).

5.10 S. McAuley and H. Ashraf, J. Phys. D Appl. Phys. Phys. **34**, 2769 (2001).

5.11 L. Ling, X. Hua, L. Zheng, G.S. Oehrlein, E. a. Hudson, and P. Jiang, J. Vac. Sci. Technol. B Microelectron. Nanom. Struct. **26**, 11 (2008).

5.12 F. Marty, L. Rousseau, B. Saadany, B. Mercier, O. Français, Y. Mita, and T. Bourouina, Microelectronics J. **36**, 673 (2005).

5.13 J. Yeom, Y. Wu, and M. Shannon, Transducers, Sensors, Actuators and Microsystems 1631 (2003).

5.14 C.J.D. Craigie, T. Sheehan, V.N. Johnson, S.L. Burkett, a. J. Moll, and W.B. Knowlton, J. Vac. Sci. Technol. B Microelectron. Nanom. Struct. **20**, 2229 (2002).

5.15 J. Kiihama□ki and S. Franssila, J. Vac. Sci. Technol. A Vacuum, Surfaces, Film. **17**, 2280 (1999).

5.16 H. Fukumoto, K. Eriguchi, and K. Ono, Jpn. J. Appl. Phys. **48**, 096001 (2009).

5.17 R.A. Gottscho, C.W. Jurgensen, and D.J. Vitkavage, J. Vac. Sci. Technol. B Microelectron. Nanom. Struct. **10**, 2133 (1992).

5.18 M.F. Doemling, N.R. Rueger, and G.S. Oehrlein, Appl. Phys. Lett. **68**, 10 (1996).

5.19 X. Hua, X. Wang, D. Fuentevilla, G.S. Oehrlein, F.G. Celii, and K.H.R. Kirmse, J. Vac. Sci. Technol. A Vacuum, Surfaces, Film. **21**, 1708 (2003).

5.20 C.B. Labelle, V.M. Donnelly, G.R. Bogart, R.L. Opila, and A. Kornblit, J. Vac. Sci. Technol. A Vacuum, Surfaces, Film. **22**, 2500 (2004).

5.21 N. Rueger, J. Beulens, Schaepkins, M.F. Doemling, J. Mirza, T. Standaert, and G. Oehrlein, J. Vac. Sci. Technol. A Vacuum, Surfaces, Film. **15**, 1881 (1997).

5.22 G. Kokkoris, A. Goodyear, M. Cooke, and E. Gogolides, J. Phys. D. Appl. Phys. **41**, 195211 (2008).

5.23 D. Zhang and M.J. Kushner, J. Vac. Sci. Technol. A Vacuum, Surfaces, Film. **19**, 524 (2001).

5.24 H.C.M. Knoops, E. Langereis, M.C.M. van de Sanden, and W.M.M. Kessels, J. Electrochem. Soc. **157**, G241 (2010).

5.25 J.W. Coburn and H.F. Winters, Appl. Phys. Lett. **55**, 2730 (1989).

5.26 G.S. Oehrlein, Y. Zhang, D. Vender, and M. Haverlag, J. Vac. Sci. Technol. A Vacuum, Surfaces, Film. **12**, 323 (1994).

Chapter 6

6.1. J. Kim, M. Ishihara, Y. Koga, K. Tsugawa, M. Hasegawa, and S. Iijima, Appl. Phys. Lett. **98**, 091502 (2011).

6.2. T. Yamada, M. Ishihara, J. Kim, M. Hasegawa, and S. Iijima, Carbon N. Y. **50**, 2615 (2012).

6.3. C.-F. Yeh, T.-J.C.T.-J. Chen, C.L.C. Liu, J.T. Gudmundsson, and M.A. Lieberman, IEEE Electron Device Lett. **20**, (1999).

6.4. N. Fox-Lyon, G.S. Oehrlein, N. Ning, and D.B. Graves, J. Appl. Phys. **110**, 104314 (2011).

6.5. J. Gudmundsson, Plasma Sources Sci. Technol. **8**, 58 (1999).

6.6. J.T. Gudmundsson, T. Kimura, and M.A. Lieberman, Plasma Sources Sci. Technol. **8**, 22 (1999).

6.7. T. Kimura and H. Kasugai, J. Appl. Phys. **107**, 083308 (2010).

6.8. A.T. Hjartarson, E.G. Thorsteinsson, and J.T. Gudmundsson, Plasma Sources Sci. Technol. **19**, 065008 (2010).

6.9. M. Sode, T. Schwarz-Selinger, and W. Jacob, J. Appl. Phys. **114**, 063302 (2013).

6.10. M. Sode, T. Schwarz-Selinger, and W. Jacob, J. Appl. Phys. **113**, 093304 (2013).

6.11. S. Wang, A.E. Wendt, J.B. Boffard, C.C. Lin, S. Radovanov, and H. Persing, J. Vac. Sci. Technol. A Vacuum, Surfaces, Film. **31**, 021303 (2013).

6.12. N. Fox-Lyon, A.J. Knoll, J. Franek, V. Demidov, V. Godyak, M. Koepke, and G.S. Oehrlein, J. Phys. D. Appl. Phys. **46**, 485202 (2013).

6.13. C. Hopf and W. Jacob, J. Nucl. Mater. **342**, 141 (2005).

6.14. X. Hua, X. Wang, D. Fuentevilla, G.S. Oehrlein, F.G. Celii, and K.H.R. Kirmse, J. Vac. Sci. Technol. A Vacuum, Surfaces, Film. **21**, 1708 (2003).

6.15. VGPS Probe System, www.plasmasensors.com (n.d.).

6.16. J.-S. Yoon, Y.-W. Kim, D.-C. Kwon, M.-Y. Song, W.-S. Chang, C.-G. Kim, V. Kumar, and B. Lee, Reports Prog. Phys. **73**, 116401 (2010).

6.17. N. Sadeghi, D.W. Setser, a. Francis, U. Czarnetzki, and H.F. Do□bele, J. Chem. Phys. **115**, 3144 (2001).

6.18. X.-M. Zhu and Y.-K. Pu, J. Phys. D. Appl. Phys. **43**, 403001 (2010).

6.19. T. Schwarz-Selinger, a. von Keudell, and W. Jacob, J. Appl. Phys. **86**, 3988 (1999).

6.20. P.R. Harris, F.W. Meyer, W. Jacob, T. Schwarz-Selinger, and U. von Toussaint, Nucl. Instruments Methods Phys. Res. Sect. B Beam Interact. with Mater. Atoms **269**, 1276 (2011).

Chapter 7

7.1. T. Desmet, R. Morent, N. De Geyter, C. Leys, E. Schacht, and P. Dubruel, Biomacromolecules **10**, 2351 (2009).

7.2. M. Baraket, R. Stine, W.K. Lee, J.T. Robinson, C.R. Tamanaha, P.E. Sheehan, and S.G. Walton, Appl. Phys. Lett. **100**, 233123 (2012).

7.3. A. Felten, C. Bittencourt, J.J. Pireaux, G. Van Lier, and J.C. Charlier, J. Appl. Phys. **98**, 074308 (2005).

7.4. E. Vietzke and V. Philipps, Nucl. Instruments Methods Phys. Res. **B23**, 449 (1987).

7.5. P.E. Hopkins, M. Baraket, E. V Barnat, T.E. Beechem, S.P. Kearney, J.C. Duda, J.T. Robinson, and S.G. Walton, Nano Lett. **12**, 590 (2012).

7.6. M. Baraket, S.G. Walton, E.H. Lock, J.T. Robinson, and F.K. Perkins, Appl. Phys. Lett. **96**, 231501 (2010).

7.7. J. Gudmundsson, Plasma Sources Sci. Technol. **8**, 58 (1999).

7.8. J. Gudmundsson, Plasma Sources Sci. Technol. **7**, 330 (1998).

7.9. C. Hopf, a. von Keudell, and W. Jacob, J. Appl. Phys. **94**, 2373 (2003).

7.10. C. Hopf and W. Jacob, J. Nucl. Mater. **342**, 141 (2005).

7.11. W. Eckstein, *Computer Simulation of Ion–solid Interactions*, 1st Ed. (Springer series in materials science, Berlin, 1991).

7.12. G.S. Oehrlein, T. Schwarz-Selinger, K. Schmid, M. Schlu□ter, and W. Jacob, J. Appl. Phys. **108**, 043307 (2010).

7.13. H. Gokan, S. Esho, and Y. Ohnishi, J. Electrochem. Soc. **130**, 143 (1983).

7.14. G.K. Choudhary, J.J. Végh, and D.B. Graves, J. Phys. D. Appl. Phys. **42**, 242001 (2009).

7.15. T. Schwarz-Selinger, a. von Keudell, and W. Jacob, J. Appl. Phys. **86**, 3988 (1999).

7.16. X. Hua, X. Wang, D. Fuentevilla, G.S. Oehrlein, F.G. Celii, and K.H.R. Kirmse, J. Vac. Sci. Technol. A Vacuum, Surfaces, Film. **21**, 1708 (2003).

7.17. N. Fox-Lyon, G.S. Oehrlein, N. Ning, and D.B. Graves, J. Appl. Phys. **110**, 104314 (2011).

7.18. H. Singh, J.W. Coburn, and D.B. Graves, J. Vac. Sci. Technol. A Vacuum, Surfaces, Film. **18**, 299 (2000).

7.19. W.M.M. Kessels, C.M. Leewis, M.C.M. van de Sanden, and D.C. Schram, J. Appl. Phys. **86**, 4029 (1999).

7.20. D. Skinner, A. Bruneteau, and P. Berlemont, Phys. Rev. E **48**, 2122 (1993).

7.21. M. Sode, T. Schwarz-Selinger, and W. Jacob, J. Appl. Phys. **113**, 093304 (2013).

7.22. M. Sode, T. Schwarz-Selinger, and W. Jacob, J. Appl. Phys. **114**, 063302 (2013).

7.23. T. Kimura and H. Kasugai, J. Appl. Phys. **107**, 083308 (2010).

7.24. M. Jiménez-Redondo, E. Carrasco, V.J. Herrero, and I. Tanarro, Phys. Chem. Chem. Phys. **13**, 9655 (2011).

7.25. P.G. Jambrina, J.M. Alvariño, D. Gerlich, M. Hankel, V.J. Herrero, V. Sáez-Rábanos, and F.J. Aoiz, Phys. Chem. Chem. Phys. **14**, 3346 (2012).

7.26. P.S. Krstic, C.O. Reinhold, and S.J. Stuart, Europhys. Lett. **77**, 33002 (2007).

7.27. P.R. Harris, F.W. Meyer, W. Jacob, T. Schwarz-Selinger, and U. von Toussaint, Nucl. Instruments Methods Phys. Res. Sect. B Beam Interact. with Mater. Atoms **269**, 1276 (2011).

7.28. H. Zhang, F.W. Meyer, H.M. Meyer, and M.J. Lance, Vacuum **82**, 1285 (2008).

7.29. N. Fox-Lyon, A.J. Knoll, J. Franek, V. Demidov, V. Godyak, M. Koepke, and G.S. Oehrlein, J. Phys. D. Appl. Phys. **46**, 485202 (2013).

7.30. W. Mo□ller and B.M.U. Scherzer, Appl. Phys. Lett. **50**, 1870 (1987).

7.31. A. Von Keudell and W. Jacob, J. Appl. Phys. **79**, 1092 (1996).